UNIVERSITÉ DU LUXEMBOURG

PhD-FSTC-2019-41
The Faculty of Sciences, Technology and Communication

DISSERTATION

Defence held on 11/06/2019 in Esch-sur-Alzette
to obtain the degree of

DOCTEUR DE L'UNIVERSITÉ DU LUXEMBOURG

EN BIOLOGIE

by

Guadalupe C. Garcia
born on 27 September 1980 in Buenos Aires (Argentina)

MULTISCALE MODELING OF MITOCHONDRIA

Dissertation defence committee

Dr Alexander Skupin, dissertation supervisor
Université du Luxembourg

Dr Genevieve Dupont
Professor, Université Libre de Bruxelles

Dr Rudi Balling, Chairman
Professor, Université du Luxembourg

Dr Jordi Garcia Ojalvo
Professor, Universitat Pompeu Fabra Barcelona

Dr Massimiliano Esposito, Vice Chairman
Professor, Université du Luxembourg

To Mikka and Lennard, for your joy.

Contents

Abstract of the dissertation

Life is based on energy conversion by which cells and organisms can adapt to the environment. The involved biological processes are intrinsically multiscale phenomena since they are based on molecular interactions on a small scale leading to the emerging behavior of cells, organs and organisms. To understand the underlying regulation and to dissect the mechanisms that control system behavior, appropriate mathematical multiscale models are needed. Such models do not only offer the opportunity to test different hypothesized mechanisms but can also address current experimental technology gaps by zooming in and out of the dynamics, changing scales, coarse-graining the dynamics and giving us distinct views of the phenomena. In this dissertation substantial efforts were done to combine different computational modeling strategies based on different assumptions and implications to model an essential system of eukaryotic life – the energy providing mitochondria – where the spatiotemporal domain is suspected to have a substantial influence on its function.

Mitochondria are highly dynamic organelles that fuse, divide, and are transported along the cytoskeleton to ensure cellular energy homeostasis. These processes cover different scales, in space and time, where on the more global scale mitochondria exhibit changes in their molecular content in response to their physiological context including circadian modulation. On the smaller scales, mitochondria show also faster adaptation by changing their morphology within minutes. For both processes, the relation between the underlying structure of either their regulating network or the spatial morphology and the functional consequences are essential to understand principles of energy homeostasis and their link to health and disease conditions.

This thesis focuses on different scales of mitochondrial adaptation. On the small scales, fission and fusion of mitochondria are rather well established but substantial evidence indicates that the internal structure is also highly variable in dependence on metabolic condition. However, a quantitative mechanistic understanding how mitochondrial morphology affects energetic states is still elusive. In the first part of this dissertation I address this question by developing an agent-based dynamic model based on three-dimensional morphologies from electron microscopy tomography, which considers the molecular dynamics of the main ATP production components. This multiscale approach allows for investigating the emergent behavior of the energy generating

mechanism in dependence on spatial properties and molecular orchestration. Interestingly, comparing spatiotemporal simulations with a corresponding space-independent approach, I found only minor space dependence in equilibrium conditions but qualitative difference in fluctuating environments and in particular indicate that the morphology provides a mechanism to buffer energy at synapses.

On the more global scale of the regulation of mitochondrial protein composition, I applied a data driven approach to explore how mitochondrial activity is changing during the day and how food intake restrictions can effect the structure of the underlying adaptation process. To address the question if at different times of the day, the mitochondrial composition might adapt and have potential implications for function, I analyzed temporal patterns of hepatic transcripts of mice that had either unlimited access to food or were hold under temporal food restrictions. My analysis showed that mitochondrial activity exhibits a temporal activity modulation where different subgroups of elements are active at different time points and that food restriction increases temporal regulation.

Overall, this thesis provides new insights into mitochondrial biology at different scales by providing an innovative computational modeling framework to investigate the relation between morphology and energy production as well as by characterizing temporal modulation of the regulatory network structure under different conditions.

List of Figures

List of Tables

Acronyms

ADP adenine diphosphate. 19, 20, 23, 24, 46–48, 51–53

ANT adenine nucleotide translocator. 3, 9, 12, 19, 23, 24, 28, 29, 46–48, 50–53, 82

ATP adenosine triphosphate. 2, 9, 19, 20, 23, 24, 31, 43, 46, 48, 50–52

CJ cristae junction. 7, 16, 48

CM cristae membrane. 13, 16, 20, 44, 46, 48, 50, 51, 53

ET electron tomography. 15

ETC electron-transport chain. 9, 72, 76

IBM inner boundary membrane. 7, 12, 13, 46–48, 50–53

ICS intracristal space. 7, 19, 20, 23, 24, 39, 46, 48

IM inner membrane. 7, 9, 16, 24, 44

IMS intermembrane space. 7, 9, 12, 20, 23, 24, 39, 41, 46, 48

MCU mitochondrial calcium uniporter. 19, 32, 42

MDL model description language. 38

ODE ordinary differential equation. 19, 24, 37, 39–41, 46–48, 51–53

OM outer membrane. 7, 9, 12, 31, 44, 46, 48, 53

SCN suprachiasmatic nucleus. 67

TCA tricarboxylic acid. 2, 9, 13

VDAC voltage dependent anion channel. 9, 12, 19, 31, 46, 48, 53

Acknowledgements

This project is the result of a long collaboration among three groups: The National Center for Microscopy and Imaging Research (NCMIR) at the UCSD, the Computational Neurobiology Laboratory at the SALK Institute for biological studies and the Integrative Cell Signalling group at the LCSB. Through the years of my PhD, I had the invaluable opportunity to spend time at each institution and learn the required tools to make this project possible.

I am truly grateful to my advisor Alexander Skupin. My path from physics to biology was quite non-linear, with ups and downs, I would not call it easy. I am grateful for your support in this transition, trust, encouragement and help to find my personal scientific approach, giving me freedom to search for my questions of interest. I thank all present and past members of the Integrative Cell Signalling group and the LCSB, we make together substantial efforts to succeed with our interdisciplinary approach.

I would like to thank Mark Ellisman for his guidance as one of the mentors of this project and for opening the doors of his lab to me. Other people from NCMIR I want to thank are Alex Perez, Eric Bushong, Sebastien Phan, Christine Kim and Daniela Boassa, they taught me all what I know about electron microscopy and available tools to analyze this data and Guy Perkins for insightful discussions about mitochondria.

From SALK, I would first like to thank Terry Sejnowski for the opportunity to work in his lab. Terry nurtures spaces where scientific discussion can flourish, gathering colleagues on a daily base –generating a very inspirational atmosphere. I would specially like to thank Tom Bartol, Tom has been also a mentor of this project; with his optimism, energy and constant support he helped me to overcome several difficulties of this project. In particular, I want to express my gratitude to Emily Liu and Tom for their help with the mitochondrial reconstruction. I would like to thank Satchin Panda for his trust and encouragement in part of this project.

And above all, I would like to thank my family, specially Niko, for your love, support, and advice.

I acknowledge the Luxembourg National Research Fund for funding my research through an AFR individual PhD grant.

Guadalupe C. Garcia.
Luxembourg, May 2019

Chapter 1

Introduction

1.1 Motivations

Life is intrinsically dynamic across all scales ranging from molecular interactions to organisms and population behavior. At any scale, the incessant change can be observed in dependence of the environment and is essential for adaptation and development. In particular the essential units of life – the cells – are in constant transformations: dividing, growing, moving, communicating with each other, sensing and reacting with the environment. These processes are empowered by the constant movement and interactions of ions, metabolites and proteins within and across cells.

Life spans across a wide range of temporal and spatial scales. The spatial domain range from nanometers of molecules, to micrometers of cells, to millimeters of organs, to meters of organisms and further beyond. In a similar way, the temporal scales of biological processes extend broadly from the nanoseconds of enzyme activity, to the milliseconds of ion channels gating, to the hours that take human cells to divide (Milo and Phillips, 2015; Phillips et al., 2012). One of the current challenges in biology is to understand how system behavior emerges as an integrated phenomenon from smaller and faster scales.

Cells come in a variety of sizes and shapes (Alberts et al., 2015), but they certainly extend in space and within their membranes hold the subunits of life: ions, metabolites, enzymes, proteins, organelles. In this crowded environment filled with water, particles move and interact to generate cellular behavior. Hence, cells are reaction-diffusion systems in complex geometries. The thermodynamic forces that spatial gradients generate make particles move and when they encounter in space they can interact chemically. Diverse chemical gradients drive cellular behavior. For example, morphogen gradients determine tissue patterning and morphogenesis (Heller and Fuchs, 2015), ionic gradients across plasma membranes control cellular excitable behavior, and through chemotaxis they drive cellular movement.

The overwhelming complexity of this plethora of interactions of diverse constitutes renders the identification of underlying principles in life problematic. How can we get a mechanistic understanding at a system-level? Can we integrate experimental data to explain system behavior by sketches and cartoons? To address these challenges, we undoubtedly need the integration of these components by mathematical models and tools (Gunawardena, 2014). Due to the dynamic nature of biological processes on different scales in space and time, appropriate mathematical models are required for the development of mechanistic insights in the evolution and regulation of these processes. In a similar manner as Kepler's laws help us to mechanistically understand and predict the movement of planets, in biology mathematics can help us to dissect the mechanisms that control cellular behavior, and in a similar way to make concrete predictions (Phillips, 2015).

The field of molecular biology has recurrently witnessed how functional properties can be encoded in the structure such as the three-dimensional structure of proteins has been systematically connected to their physiological properties (Alberts et al., 2015). Each unique amino acid sequence determines its conformation and therefore its biological activity. This link between structure and function has inspired the field of system biology (Kitano, 2002) to search for such causal relation also at the system level where network structures are explored and linked to sytem-level function of the cell.
Also spatial interactions can have a huge impact on the dynamics of a system. A number of phenomena are exclusively observed in spatially extended systems like Turing patterns, spiral and rotating waves or gradients. The advancements in spatial and temporal resolution of experimental techniques as well as the progress in simulation methods allow now the extension of system biology to spatial system biology approaches.

Life is inevitable based on non-equilibrium processes and therefore energy is ubiquitously required to maintain life with all its dynamic aspects. Hence, the essential task of cells is to extract energy from their environment and use it for growth and adaptation. For this purpose, the energy e.g. stored in nutrient molecules is converted to energy stored in chemical bonds of adenosine triphosphate (ATP), the main energy substrate of life (Alberts et al., 2015). There exist two main ATP producing pathways: (i) glycolysis, which generates ATP due to the breakdown of glucose, and (ii) oxidative phosphorylation in which electron transport generates an electrical potential that is eventually used to generate ATP.

In most eukaryotic cells, oxidative phosphorylation takes place in mitochondria which are membrane bound organelles. The place where the enzymes of the tricarboxylic acid (TCA) cycle reside and where the major synthesis of ATP occurs due to the higher efficiency of oxidative phosphorylation compared to glycolysis. Besides this essential energy supply, many additional functions have been associated with mitochondria including cell signaling by reactive oxygen species or Ca^{2+} and apoptosis (Duchen,

1999) expanding its relevance in cell life and death. A well accepted theory sets the origin of mitochondria to the symbiosis of a prokaryotic cell engulfed by a nucleated cell (Scheffler, 2009). Mitochondria still preserve a prokaryotic-like circular genome that encodes a number of proteins, and the machinery necessary to decode this information. However, the vast majority of mitochondrial proteins are encoded by nuclear genes. In recent years, $\sim$ 1500 nuclear genes have been associated with mitochondrial-localized proteins (Calvo et al., 2015).
As detailed later in Chapter 2, mitochondria exhibit a diverse spectrum of phenotypes in respect to their size, structure and function and their dysfunction is related to different diseases. Mitochondria are, such as life in general, very dynamic. On the slower time scale of hours, mitochondria adapt their molecular content in relation to the cellular context including circadian modulation. On the faster time scale of seconds and minutes, they can fuse and divide also in response to environmental changes. Furthermore, their rather peculiar structure with a number of subcompartments generated by the folding of its own membranes has been shown to adapt to metabolic conditions. Perturbations of these adaptive processes can have substantial impact on energy production and therefore on cells and life. A compelling open question from the spatial systems biology perspective is therefore how mitochondrial structures affect its function on the different scales. On the slower time scale, the adaptation of protein content may effect the energetic machinery by changing the overall molecular interactions. On the faster time scale, the formed subcompartments are speculated to provide an advantage for ATP production but a mechanistic and quantitative framework is still lacking.

1.2 Aims

The presented work investigates these two separate time scales of mitochondrial dynamics. The first part focuses on the faster time scale by studying the functional implications of the intrigued mitochondrial structure on its ATP generating function. For this purpose, high-resolution imaging data and high-performance computation were combined to investigate the relation between the spatial structure and physiological function. To cover the relevant scales, three-dimensional morphologies from electron microscopy tomography were integrated by agent-based modelling which considers the molecular dynamics of the main ATP production components. For this part the main goals were:

I. to generate an *in silico* representation of mitochondria from electron tomograms,

II. to develop and implement kinetic models of the main components of ATP production in mitochondria, including ATP synthase and adenine nucleotide translo-

cator (ANT),

III. to explore the impact of mitochondrial morphology on diffusion,

IV. to investigate the formation of suborganelle concentration gradients,

V. to investigate how the interplay between diffusion and spatial localization of ANTs and ATP synthases affect mitochondrial ATP production,

VI. to analyze potential energetic consequences for synaptic signal transmission.

The second part focuses on the slower time scale by investigating temporal patterns of mitochondrial gene expression under different feeding conditions. For this part the main goals were:

I. to identify distinct temporal patterns of mitochondrial genes expression under different feeding conditions,

II. to associate the temporal patterns to functional relation.

1.3 Overview of the thesis

This dissertation is organized as follows: the first part entitled 'Mitochondrial morphology: a buffering mechanism' focuses on the spatial mitochondrial model, its simulations and results. The more explorative second part entitled 'Mitochondrial genes and its temporal organization' focuses on the analysis of the temporal expression pattern of mitochondrial genes under different feeding conditions

The first part starts in Chapter 2 by providing the biological background to anticipate the hypothesis of the project in more detail and relate it to the available literature. Chapters 3, 4 and 5 describe the material and methods employed where Chapter 3 provides a description of the mitochondria reconstruction from serial electron tomogram, Chapter 4 introduces the kinetic models, and Chapter 5 details the simulation methods used and the *in silico* experiments performed. In Chapter 6 the results are presented, and Chapter 7 gives the conclusions of this part.

The second part is described in Chapter 8, and it is divided into four sections. Section 8.1 provides the biological background needed to understand the content of the chapter. Section 8.2 presents the material and methods employed and the explorative results are introduced in Section 8.3. Finally, in Section 8.4 conclusions are drawn and critically discussed.

Part I

Mitochondrial morphology: a buffering mechanism

Chapter 2

Background

Mitochondria are essential for eukaryotic life by generating the majority of ATP and their involvement in diverse signaling mechanisms. Dependent on their physiological context, mitochondria exhibit diverse phenotypes and their dysfunction is linked to various diseases, including cancer (Wallace, 2012), diabetes (Lowell and Shulman, 2005) and neurodegeneration (Knott et al., 2008). The specific energetic needs of the brain and in particular of synaptic transmission is accompanied with a distinct mitochondrial phenotype on the molecular as well as on the morphological level (Devine and Kittler, 2018). Hence, understanding the interplay between molecular and morphological features of mitochondria may provide new insights into brain energy homeostasis and its mechanisms.

This chapter gives a brief introduction to the ATP producing mechanism in mitochondria. For this purpose, Section 2.1 details the complex mitochondrial morphology and Section 2.2 focuses on the molecular key components. In Section 2.3, the relation between morphology and metabolic states is described. Finally, Section 2.4 gives a rough overview and a brief description of computational mitochondria models in the literature.

2.1 Structure and Morphology

The mitochondrial structure is characterized by two membranes with the external one, called outer membrane (OM), surrounding the internal membrane (Figure 2.1). The inner membrane (IM) presents a number of invaginations and infoldings called cristae. This complex structure forms specific compartments: the intracristal space (ICS), the narrower intermembrane space (IMS), and the matrix describing the internal compartment (Figure 2.1), each of them with specific protein content. Cristae are attached to the inner boundary membrane (IBM) through narrow tubular openings called cristae junctions (CJs) (Perkins et al., 1997), having relative uniform size and shape of $\sim$

15 nm in diameter in brain tissue (Perkins et al., 2001). In particular, the fact that these spaces communicate through narrow openings raises the possibility that they operate as functionally separate compartments.
Within the brain, mitochondria typically exhibit a composition of lamellar and tubular cristae (Perkins et al., 2001), with lamellar cristae more at the center and tubular cristae in the periphery. In particular, synaptic mitochondria are further specialized to their physiological context by their smaller volume (Perkins et al., 2001), increased motility, higher ratio of cristae to OM surface (Perkins et al., 2010) and distinct metabolic profiles (Devine and Kittler, 2018).

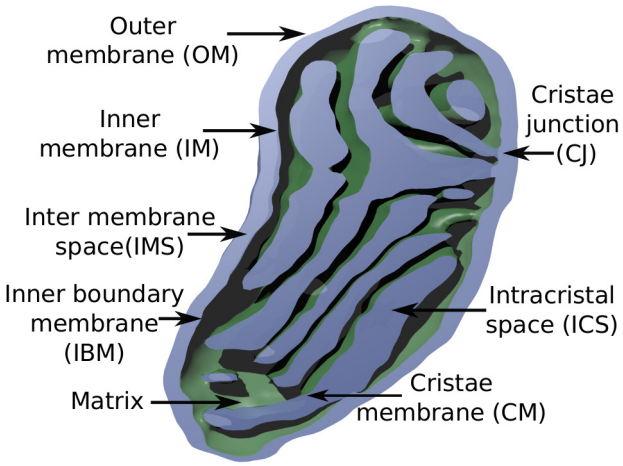

Figure 2.1: Functional annotations of mitochondrial morphology. The outer membrane (OM) and the inner membrane (IM) are separated by the intermembrane space (IMS). IM separates the interior matrix of the mitochondrion from the IMS and can be topologically divided into the inner boundary membrane (IBM) and the cristal membrane (CM) connected by tubular cristal junctions (CJs).

2.2 Molecular key components of ATP production

Energy is essential for life. Cells need it to grow, move and divide. Cells convert the energy stored in chemical bonds in organic molecules into energy stored in chemical bonds in ATP, through a number of chemical reactions happening in mitochondria. Pyruvate and fatty acids can be used as fuel molecules, converted to acetyl CoA in the mitochondrial matrix where afterwards acetyl CoA is further oxidized via the TCA cycle. The oxidation of acetyl CoA generates high-energy electrons carried by NADH or FADH_2. Subsequent oxidation of these substrates transfer electrons to the electron-transport chain (ETC), a series of protein complexes in the inner mitochondria membrane. The movement of electrons through the ETC liberates energy that can be used to pump protons (hydrogen ions) across the membrane. The resulting proton gradient generated across the IM is used to drive the synthesis of ATP from ADP and inorganic phosphate in the matrix. The molecular machine in charge of this energy conversion step is the ATP synthase (see next section for more details). To be further employed in cellular processes, the generated ATP in the matrix needs to be exported to the cytosol by ANTs. ANTs translocate ATP into the IMS from where it is subsequently transported into the cytosol by voltage dependent anion channels (VDACs) across the OM. Figure 2.2 is a schematic representation of the processes described above.

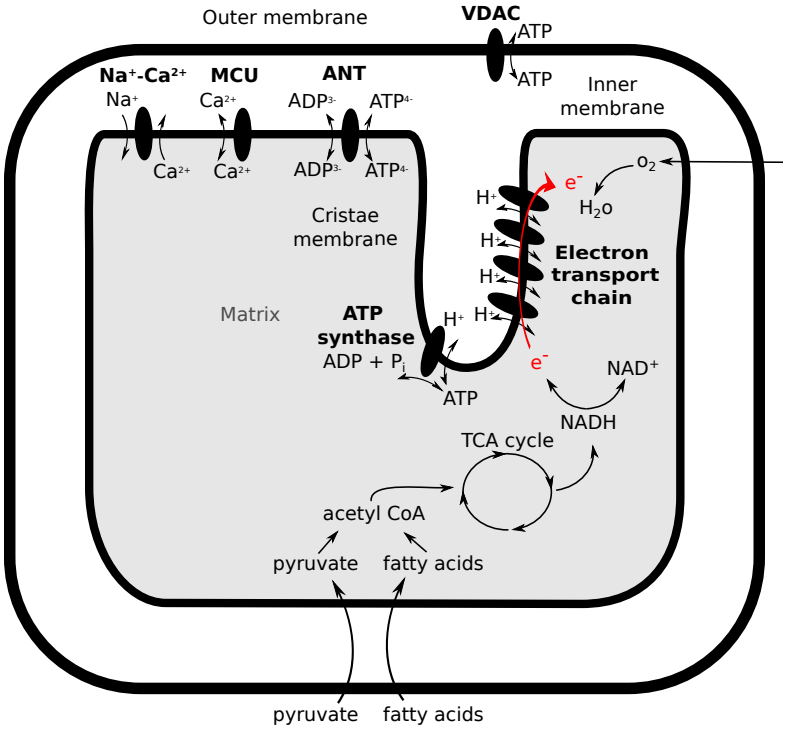

Figure 2.2: Schematic representation of the processes happening in mitochondria for ATP production. Pyruvate and fatty acids are imported into the mitochondrial matrix for conversion in acetyl CoA. Enzymes of the TCA cycle metabolized acetyl CoA, through a number of chemical reactions, generate high-energy electrons carried by NADH or $\mathrm{FADH_2}$ (not shown). Subsequently, NADH is oxidized, passing electrons to the electron-transport chain, where they are transported along the complexes to finally produce water molecules. The transport of electrons is coupled to the transfer of protons across the membrane, generating a chemical and voltage gradient. This electrochemical gradient is further used to drive the synthesis of ATP, phosphorylating ADP in the mitochondrial matrix through ATP synthase. To be further employed in cellular processes ATP has to be actively exported from the matrix by ANT.

2.2.1 ATP synthase

The ATP synthase or $\mathrm{F_oF_1}$ ATPase is a multiprotein complex ($\sim 500\mathrm{kDa}$) embedded in the IM that synthesizes cellular ATP from ADP and inorganic phosphate ($\mathrm{P_i}$). By a marvellous mechanism (Yoshida et al., 2001), it uses the energy stored in the electrochemical gradient to rotate its own subunits to catalyze this reaction. This is one of the most conserved enzymes during evolution and is present in bacteria, mitochondria and chloroplast (Yoshida et al., 2001). The multisubunit complex has two functional domains known as $\mathrm{F_o}$ and $\mathrm{F_1}$. The membrane intrinsic $\mathrm{F_0}$ is linked by stalks to the membrane extrinsic $\mathrm{F_1}$ domain (Alberts et al., 2015) (Figure 2.3). The approximately spheric $\mathrm{F_1}$ domain contains the catalytic sites for the substrates, whereas the $\mathrm{F_o}$ domain contains a motor that rotates when protons flow through the carrier. As the stalk rotates and alters the protein conformation to produce ATP. The reverse reaction can also occur using the energy of ATP hydrolysis to induce the rotation of $\mathrm{F_o}$ in reverse direction and drive a transfer of protons 'uphill'.

Experimental findings on mammalian mitochondria report that ATP synthases are typically arranged in rows of dimeric supercomplexes at the apex of lammellar cristae and along the length of tubular cristae, at the most tightly curved membrane regions (Strauss et al., 2008).

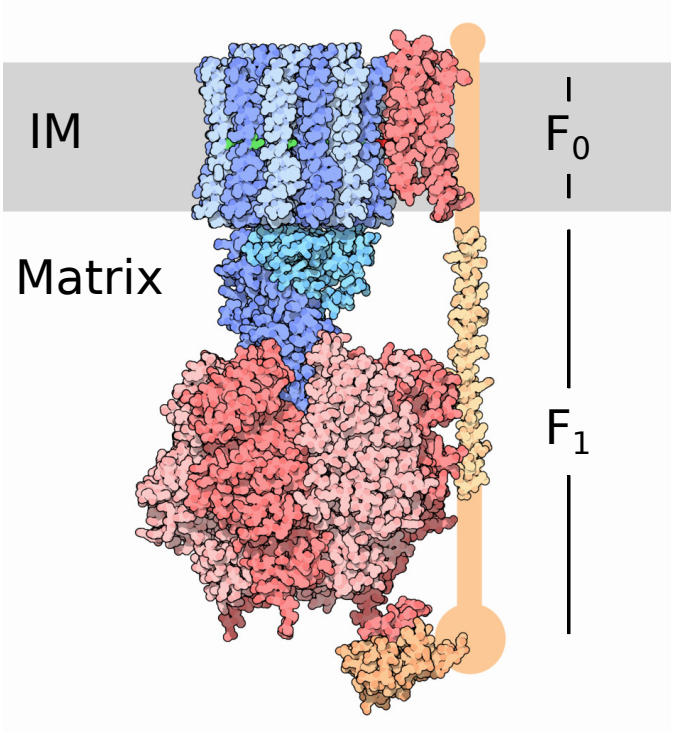

Figure 2.3: Schematic representation of mitochondrial ATP synthase showing two of the functional domains of the complex F_0 and F_1, figure reproduced from RCSB PDB (Goodsell et al., 2015).

2.2.2 ATP/ADP translocator

The vital process of import and export of ADP and ATP from the IMS to the matrix and vice versa is carried out by the ATP/ADP translocator or ANT (Klingenberg, 2008). The antiporter operates with a 1:1 stoichiometry exchanging either one ADP or ATP with one endogenous ADP or ATP from the matrix. The exchange of nucleotides is highly specific and electrogenic; the ionized form of the nucleotides is translocated (ADP^{3-} and ATP^{4-}), being the membrane potential the driving force of the asymmetric exchange. The location of ANTs in mitochondria has not yet been definitively determined. Experimental evidence shows on the one hand that they may form complexes with ATP synthases and phosphate carrier (Ko et al., 2003) located in the CM (Wittig and Schägger, 2009; Vogel et al., 2006) and on the other hand studies report an association with VDAC located in the IBM (Vyssokikh et al., 2001). Two isoforms have been identified with apparent different location in the mitochondrial membrane (Vyssokikh et al., 2001).

2.2.3 VDAC

The OM is a lipid bilayer membrane of $\sim$ 7 nm thick (Perkins et al., 1997) that separates the IMS from the cytosol, it has the critical role to control the flow of molecules from and to the mitochondrial interior. The most abundant protein in the OM is VDAC (Szabo and Zoratti, 2014), at a mean density of $1 \cdot 10^4$ per μm^2 (De Pinto et al., 1987). These proteins form large pores that are the main mechanism for metabolites and ions (including Ca^{2+}) to cross the OM. The pores have greater permeability to anions and are voltage-dependent. They close partially at voltages higher than $\sim$ 20 mV of either polarities and open at low potential (Colombini, 1989). Three isoforms exist, VDAC1, VDAC1 and VDAC3, which exhibit a distinct distribution between cell types and distinct electro-physiological properties.

2.3 Metabolic States

The internal morphology of isolated mitochondria exhibit a large heterogeneity dependent on metabolic conditions, different metabolic states have been characterized and tied to their respiratory rates (Hackenbrock, 1966, 1968). Reversible ultrastructure transitions between two metabolic states known as orthodox or state IV and condensed or state III were analyzed (Hackenbrock, 1966), showing distinct features in electron tomograms such as an enlarged matrix, close opposition of the outer and IBM, and small intracristal volume observed in state IV. These states are assumed to be a charged resting state (state IV) and a fully active state (state III) (Perkins and Ellisman, 2011), and the predominant ones observed in situ, dependent on the

energetic demand (Perkins and Ellisman, 2011).

While extended literature (Scalettar et al., 1991; Mannella, 2006; Perkins and Ellisman, 2011) suggests a link between the inner membrane morphology and mitochondrial function, a mechanistic understanding is still lacking. This gap is mainly caused by the static data generated by electron tomography needed to reveal the internal structure. Dynamic effects caused by changing morphologies rely therefore on computational modeling.

2.4 Mathematical models

Several mitochondria models have already been proposed (Magnus and Keizer, 1997; Cortassa et al., 2003; Beard, 2005). Many of them were developed from the pioneer work of Magnus and Keizer (Magnus and Keizer, 1997). These models are rather complex and include a number of processes occurring in mitochondria like the electron transport system, calcium dynamics, the TCA cycle, etc. However, none of them include the spatial architecture of the organelle. Attempts to develop a spatial mitochondria model were made but lack consistent foundation (Mannella et al., 2013).

Effects on diffusion due to the internal structure were studied based on simplified geometries (Partikian et al., 1998; Dieteren et al., 2011) and indicated anomalous diffusion in some cases (Ölveczky and Verkman, 1998), but disagreed on the impact of the internal structure (Dieteren et al., 2011; Partikian et al., 1998).

Electro-diffusion simulations were performed to analyze the interplay between morphology and the electrochemical potential, and predicted an increased in proton concentration in the cristae membrane (CM) compared to the IBM (Song et al., 2013).

Chapter 3

Generating model geometries for numerical simulations

This chapter describes the steps required to generate realistic three-dimensional (3D) reconstructions of mitochondria from electron tomograms. In Section 3.1 a brief description of the data acquisition process is given. This is followed by Section 3.2 devoted to explain how the membranes were segmented and surfaces generated. Finally in Section 3.3, I describe the process and tools needed to obtain watertight triangulated meshes for computer simulations.

3.1 Data Acquisition

Electron microscopy has been an invaluable tool to resolve the substructures of cells, and in particular of mitochondria (Scheffler, 2009). In the last decades, more advanced experimental techniques, such as electron tomography (ET), have enabled the generation of 3D reconstructions of cells and organelles (Frey et al., 2006) with image resolution in the range of $\sim$ 3 to 20 nm. In ET thick sections of a sample are used ($\sim$ 200-3000 nm), and through a process of tilting the sample, a tilt series is obtained by rotating the sample holder in the transmission electron microscope and collecting the corresponding images. The volume is subsequently reconstructed by computational algorithms which generate digital slices of only a few nanometers of thickness. With this method, a significant fraction of an organelle can be imaged but due to sample preparation it is rather unlikely to cover a full organelle. One challenge of this project was the need of a complete mitochondrion reconstruction since the physiological computer simulations do not only require high quality meshes but also closed structures.
As for electron microscopy, ET samples have to be plastic embedded and frozen-hydrated (Perkins et al., 2015). Frozen-hydrated samples are frozen very quickly and result in a vitreous (glass-like) ice specimen. By this method, samples are conserved

in close-to-physiological conditions but are not suitable for sectioning due to the substantial material lost between cuts. A method combining chemical fixation with high pressure freezing and freeze substitution was developed (Sosinsky et al., 2008) to obtain large volumes of well-preserved tissue.

The mitochondrial reconstruction was performed from 3 sections of a multi-tilt serial electron tomogram (Phan et al., 2016) of a cryo-fixated high pressure frozen (Sosinsky et al., 2008) mouse cerebellum sample which contained the complete organelle. Images were realigned using the software package TxBR (Lawrence et al., 2006) and down-sampled by a factor of 4 for processing, yielding a final voxel resolution of 1.64 nm. The mitochondrion was embedded into a stack of 360 images. The tomogram is visualized in Figure 3.1 and a movie of the full tomogram used for the reconstruction can be found online Multi-tilt serial electron-tomogram of a presynaptic mitochondrion[1] .

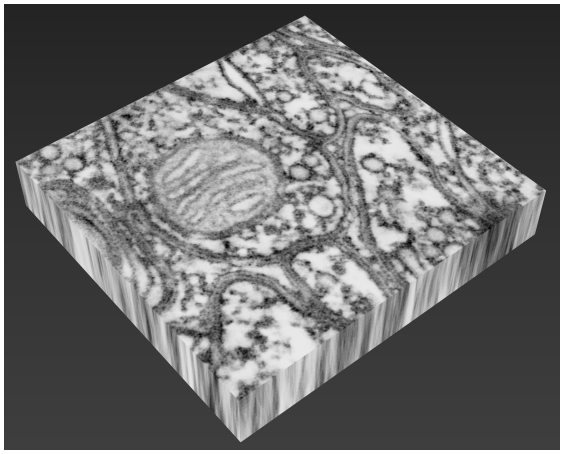

Figure 3.1: Multi-tilt serial electron tomogram of a presynaptic mitochondrion in a cerebellum mouse neuron. For the representation of the tomogram, ten digital slices with simulated thickness are shown.

3.2 Segmentation and Surface Generation

The first step to generate a 3D reconstruction of a mitochondrion is to manually trace the membranes of the mitochondrion. The outer, closed IM and CM were separately traced using RECONSTRUCT. Subsequently, contours were imported into Blender[2] for

[1] `http://r3lab.uni.lu/frozen/mitochondrial-morphology-provides-a-mechanism-for-energy-buffering-at-synapses/`

[2] Blender is a free and open source software that supports 3D modeling, animation, rendering, video editing and more.

realignment and manually correction (due to the loss of tissue during the sectioning of the sample). Afterwards, contours were converted into three-dimensional surfaces using VolRover. In this way, the outer membrane, closed inner membrane[3] and the cristae membrane triangulated meshes have been generated. Subsequently, the meshes were re-imported into Blender, to generate the CJs by intersecting the mesh of the cristae membrane with the closed inner membrane. This step was performed by applying a boolean difference operation in Blender. The synaptic membrane surrounding the mitochondrion was also traced using the software IMOD to generate contours and finally the 3D structure.

3.3 Surface Improvements

The resulting meshes had to be further improved for computer simulations since they have to be watertight, triangulated, manifold, and with outward facing normals. Figure 3.2A exhibits the cristae membrane before improvement processing. The quality of the generated 3D reconstruction also depends on the software employed to generate the meshes from contours. First, meshes were treated in Blender by the CellBlender's[4] Mesh Analysis tool (a tutorial can be found here[5]). Mesh improvement in general is far from being a standardized process and requires a lot of manual curation including mesh editing, validation and solving specific problems that might arise.

Further optimization was performed with the mesh improvement library and CellBlender add-on GAMer. With GAMer, the surfaces can be smoothed while features like the total volume or surface are preserved. Additional steps described in the tutorial[6] were used for final surface improvements. Figure 3.2 exemplifies this optimization where the initially segmented cristae membrane surface (Figure 3.2A) is improved by GAMer as shown in Figure 3.2B where the inner boundary membrane is also included as almost transparent surface. An analogous process was applied to generate and improve the synaptic membrane surface. To consider possible compression effects, 10 vesicles were traced, and its shape was set to spheres with a diameter of 40 nm. We observed shrinkage in Z direction of around 20% and for compensation we rescaled the reconstructed meshes by a factor of 1.239 in the Z direction. To summarize, we show in Figure 3.3 our final result – the 3D reconstruction of the mitochondrion and the surrounding presynaptic terminal embedded in a digital slice of the electron tomogram used for segmentation.

[3]We refer to the closed inner membrane to the inner boundary membrane without the cristae membrane, as a closed surface.

[4]Cellblender, is a plug-in of MCell in Blender

[5] `http://mcell.org/tutorials/mesh_repair.html`

[6]`https://mcell.org/tutorials/gamer.html#gamer`

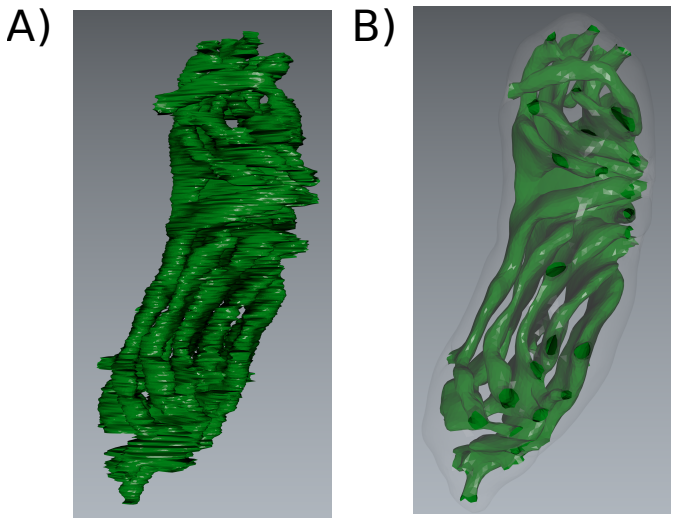

Figure 3.2: Mitochondrial morphology reconstruction first leads to mesh generation (A) and after optimization to waterproofed *in silico* representation (B) where green corresponds to the cristae membrane and semi-transparent blue surfaces to inner and outer membranes, respectively.

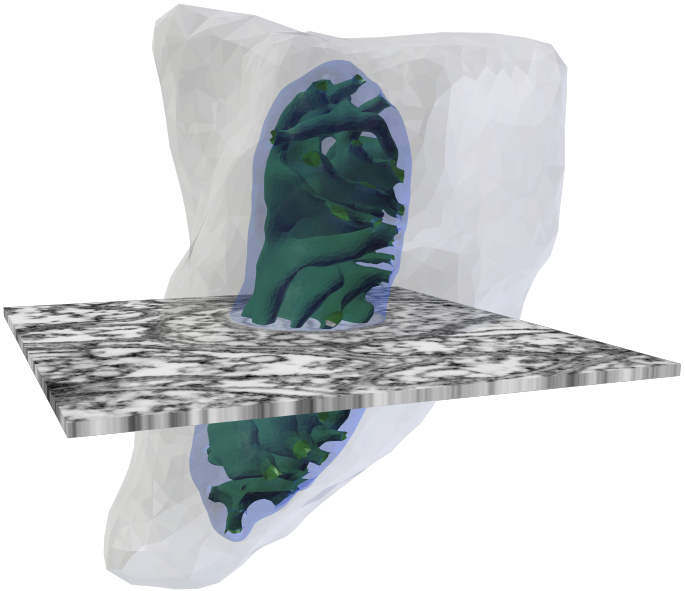

Figure 3.3: A presynaptic mitochondrion embedded in a digital slice of the electron tomogram use for segmentation.

Chapter 4

Kinetic Models

The investigation of the spatiotemporal dynamics within mitochondria relies on computational modeling because the internal structure can be only resolved by electron microscopy which generates static images. For making these data dynamic, I developed a mitochondria model from first principles by adapting molecular models from literature for the key molecules involved in ATP production and incorporate them into a spatial framework. For this purpose, I first decided on a mathematical model available in the literature. Afterwards, I derived a system of ordinary differential equations (ODEs) for each them and finally the validated MCell implementations were incorporated into the reconstructed mitochondrial mesh. Overall, the concrete dynamic ODEs and MCell implementations needed more parameters than in the original publications due to the considered non-equilibrium scenarios.

This chapter focuses on the kinetic models used, it begins with a description of the ATP synthase implementation. Followed by Section 4.2 devoted to describe the ANT model by pointing to the modifications carried out and summarizing all experimental results used for paramterization. In Section 4.3, I continue with the VDAC model before the implementation of ATP-consuming reactions is outlined. Finally, Section 4.5 characterizes a model for the mitochondrial calcium uniporter (MCU) which has not been incorporated in the final version of the mitochondria model.

4.1 ATP synthase

ATP synthase (also named as F_OF_1 or Complex V) is the ADP phosphorylating nanomachinery which generates the majority of ATP in eukaryotic cells. Given its central importance for life it has been intensively studied under a large variety of conditions and from different perspectives. The implemented model for the ATP synthase is based on a six states model of a proton pump by Pietrobon and Caplan (1985) shown in Figure 4.1A where each state has been mapped to a number in Figure 4.1B following

the original notation. States toward the matrix are on the left and those oriented toward the ICS are on the right. A clockwise cycle starting in E^{-3} (state 6) represents the binding of n protons from the ICS (state 5), transport of the protons (state 4), binding of adenine diphosphate (ADP) and phosphate (P_i) (state 3) and the subsequent synthesis of ATP (state 2) which is followed by unbinding of the protons in the matrix (state 1). Note that proton translocation without ATP synthesis might also occur (transition from state 5 to 2). The original model used the Hill diagram to write down the relation between the fluxes and the thermodynamic forces for any given cycle (Hill, 1989) and explored the region of linearity close to the inflexion points (in the framework of non-equilibrium thermodynamics).

The unoccupied proton binding site (state 1 and 6) is considered to be negatively charged and hence the rate constants of the transitions depend on the membrane potential. The original work used thermodynamic considerations to calculate this dependence by assuming a symmetric barrier Pietrobon and Caplan (1985). Three protons are translocated per ATP molecule synthesized accordingly to experimental findings [BNID 101774, 101775] (Milo et al., 2009). Transitions from state 1 to 2 or 6 to 5 imply the binding of three protons to the empty binding sites of the protein. Therefore, these are reduced transitions that involve a number of transient states. These imposed constrains to the reaction constants were taken into account to set the parameter values Pietrobon and Caplan (1985). For the implemented ATP synthase model, I started with the originally determined parameter values (Pietrobon and Caplan, 1985) which were modified in analogy to other work (Magnus and Keizer, 1997) as explained below.

Transitions from state 4 to 3 imply binding of ADP and phosphate simultaneously and are reduced transitions as well with a pseudo second order rate constant $k_{43} = k^{*}_{43}$ $[P]_i$ $[ADP]_i$. If we consider the phosphate concentration constant, this expression can be written as k^{**}_{43} $[ADP]_i$ where k^{**}_{43} is a pseudo first order rate constant. In the original paper, the value of k_{43} is 10^2 s^{-1} and if we assume an $[ADP]_i$ concentration of 125 μM and a constant $[P]_i$ of 20 mM, the value of k^{**}_{43} can be determined as $8{\cdot}10^5 M^{-1}s^{-1}$. I used ADP and ATP concentrations in the matrix and the IMS as input variables and therefore this parameter sets the rate constant (k^{**}_{43}) of the transition from state 4 to 3. I further considered the proton concentration inside the ICS as well as in the matrix to be constant with a $\Delta pH = -0.4$ to reflect the higher concentration in the ICS than in the matrix. The original work Pietrobon and Caplan (1985) considered the concentration of pH being equal in the matrix and the ICS. Therefore I modified the rate constant k_{12} in analogy as before leading to the rate constant $k_{12} = k^{*}_{12}$ $[H]^3$ with which we determined k^{*}_{12} by assuming a pH in the matrix of 7.8 resulting the rate constants given in Table 4.1.

In my model, ATP synthases are localized at the apex of the CM in lamellar cristae and along the length of tubular cristae at the most tightly curved membrane regions. This positioning is in accordance with experimental findings on mammalian

mitochondria reporting that ATP synthases are typically arranged there in rows of dimeric supercomplexes (Strauss et al., 2008). The density of proteins, pH and all kinetic rate constants are given in Table 4.1. The number of proteins was determined using the density estimated previously Song et al. (2013) to be 2500 molecules/μm^2 which is in good agreement with independent estimations Schwerzmann et al. (1986). Using the volume enclosed by the inner membrane of my reconstructed mitochondrion, I eventually determined the number of ATP synthases in the model as 3800.

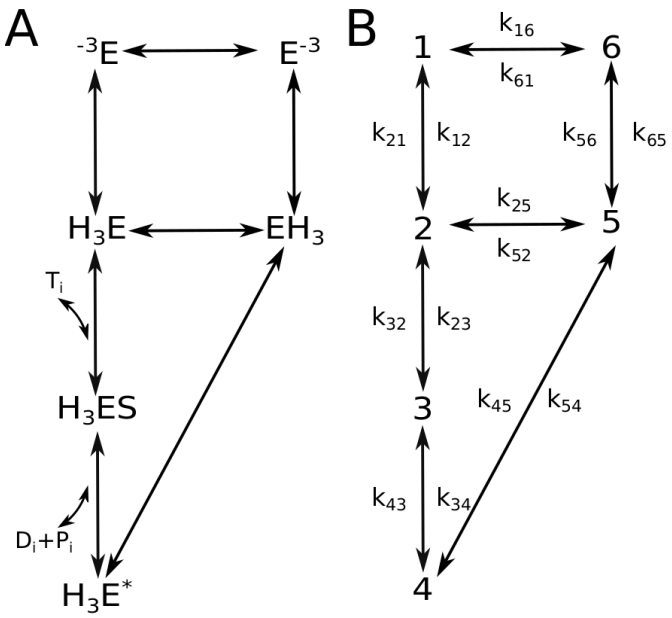

Figure 4.1: Markov chain model of ATP synthase describing the molecular kinetics. A) Markov chain model of ATP synthase describing the molecular kinetics. It is composed of six states. States toward the matrix are on the left and states oriented toward the outside are on the right. A clockwise cycle starting from E^{-n} corresponds to the binding of n protons from the outside and transport to the matrix follow by the binding of ADP and P_i to further synthesis of ATP, and unbound the n protons in the matrix. B) The states are assigned to numbers and the first order or pseudo first order rate constants k_{ij} are labeled accordingly to the transition they drive from state i to state j.

Parameter	Value	Units	Reference
pH_{matrix}	7.8		(Magnus and Keizer, 1997)
$pH_{cristae}$	7.4		(Magnus and Keizer, 1997)
$[P_i]$	20	mM	(Magnus and Keizer, 1997)
$\Delta\phi$	-180	mV	
Density	2500	μm^{-2}	(Song et al., 2013; Schwerzmann et al., 1986)
# ATP synthase	3800		
Temperature	310	K	
k_{16}	452457	s^{-1}	(Pietrobon and Caplan, 1985)
k_{65}	$1{\cdot}10^3$	s^{-1}	(Pietrobon and Caplan, 1985)
k_{54}	100	s^{-1}	(Pietrobon and Caplan, 1985)
k_{43}	$8{\cdot}10^5$	$M^{-1}s^{-1}$	(Magnus and Keizer, 1997)
k_{32}	$5{\cdot}10^3$	s^{-1}	(Pietrobon and Caplan, 1985)
k_{21}	40	s^{-1}	(Pietrobon and Caplan, 1985)
k_{61}	11006	s^{-1}	(Pietrobon and Caplan, 1985)
k_{12}	24	s^{-1}	(Pietrobon and Caplan, 1985)
k_{23}	4	$\mu M^{-1}s^{-1}$	(Magnus and Keizer, 1997)
k_{34}	100	s^{-1}	(Pietrobon and Caplan, 1985)
k_{45}	100	s^{-1}	(Pietrobon and Caplan, 1985)
k_{56}	1000	s^{-1}	(Pietrobon and Caplan, 1985)
k_{25}	$1.17{\cdot}10^{-12}$	s^{-1}	(Magnus and Keizer, 1997)
k_{52}	2	s^{-1}	(Magnus and Keizer, 1997)
n	3		(Pietrobon and Caplan, 1985)

Table 4.1: Chemical kinetic rate constants and parameters for the ATP synthase model.

4.2 ATP/ADP translocator

As described in Section 2.2.2, the ANT is the adenosine transporter in mitochondria, which mediates transport of ADP and ATP between the matrix and the intermembrane space. Due to its importance, it has been intensively investigated and two different kinetics mechanisms were proposed with one binding site, known as *ping-pong mechanism* (Kraemer and Klingenberg, 1982), and with dual sites binding known as the *sequential mechanism* (Duyckaerts et al., 1980) accordingly with Cleland's definition (Cleland, 1963). One can discriminate between the two mechanisms by their contrasting properties in Lineweaver-Burk plots (v^{-1} vs [nucleotide]$^{-1}$) (Voet and Voet, 2011). From such experiments the sequential mechanism could be confirmed (Duyckaerts et al., 1980; Barbour and P, 1981). Moreover, the dimeric organization of the carrier supports the hypothesis of two transport pathways (Nury et al., 2006). In this case, two molecules bind to the protein from different sides of the membrane forming a ternary complex.

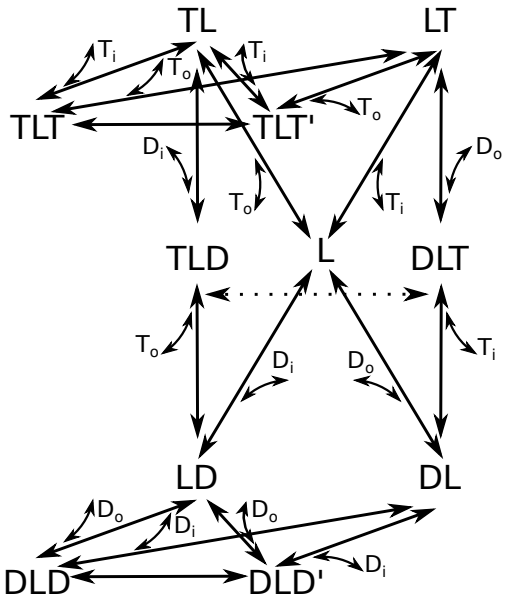

Figure 4.2: Markov chain model of the ANT describing the molecular kinetics. ATP and ADP are represented by the letter T and D, with the subindex i referring to the matrix side and o to IMS and ICS (called outside). L represents the free protein and YLX represent a three molecular state with one X molecule bound from the matrix side and one Y molecule from the outside.

The ANT model developed by Metelkin et al. (2006) takes into account the above mentioned considerations and furhter important properties of the carrier such as the dependence of the exchange rate on the membrane potential. They applied quasi-steady state and quasi equilibrium approximations to the kinetic scheme and derived

equations for the total turnover rate of ATP and ADP. The kinetic parameters were fitted using experimental data by Kraemer and Klingenberg (1982).
The here developed model is based on this previous work but due to the considered non-steady state and non-equilibrium conditions more parameters had to be estimated leading to a slightly modified parameter set 4.2. The first step in model adaptation was to reproduce the results presented in Metelkin et al. (2006) to ensure model validity (Appendix, Section 8.6). Careful analysis has revealed typos in the original publications but eventually the results were reproduced successfully.
As a first modification to the model, two additional states were introduced to monitor futile translocations in MCell (e.g. TLT $\longrightarrow$ TLT'. This did not have any implications in terms of the dynamics and the given rate constants led to equivalent model outcomes. The resulting kinetic ANT model shown in Figure 4.2 is composed of 11 states and 19 bidirectional transitions between them resembling the binding and unbinding of ATP and ADP from different sides of the IM. ATP and ADP are represented by the letter T and D, with the subindex i referring to the matrix side and o to IMS and ICS (called outside). L represents the free protein, and YLX represent a three molecular state with one X molecule bound from the matrix side and one Y molecule from the outside. The essential ADP to ATP exchanging step is indicated by a dash arrow in Figure 4.2 indicating the reaction DLT $\longrightarrow$ TLD.

Starting from fitted flux parameters from Metelkin et al. (2006) for ANTs extracted from heart mitochondria (Kraemer and Klingenberg, 1982), we first estimated parameters for the implementation in MCell and the corresponding ODE model (see Chapter 5). To adapt the model to the non-steady state condition, the backward and forward rate constants were estimated from the dissociation constants. The forward rate constants were set as smaller than the diffusion limited rate (see Section Rates and Duration in Milo and Phillips (2015)) and the backward rate constants were set to satisfy the dissociation constant ratio. For instance, the dissociation constants for a membrane potential of 180 mV is $K_{T_o} \sim 400$ µM in the original paper, and in our simulations 500 µM was chosen. Analogously, K_{D_o} was modified from ~ 51 µM in the original paper to 25 µM in our simulations. In (Metelkin et al., 2006) only the ratio of the internal dissociation constants is given (~ 10 for $\Delta\psi = 180$ mV). I estimated the dissociation constants from the matrix side K_{T_i} and K_{D_i} as 6.25 mM and 10 mM, respectively (the ratio is ~ 1.5) from fitting procedures to the experimental data. Interestingly, these values are in the mM range, in contrast to the external rates that are in the μM rang. This indicates a lower affinity of substrates from the matrix side. Values in the same range have been observed for the Michaelis-Menten constant K_m for other mitochondrial carriers (Klingenberg, 2008). The rate constants for the kinetic model are given in Table 4.2 and Table 4.3 for 180 and 0 mV, respectively.

These set of parameters were chosen to qualitatively reproduce the independent

data of Kraemer and Klingenberg (1982) from isolated translocators in liposomes[1] as well as data of Duyckaerts et al. (1980) for heart mitochondria. The experimental data of Kraemer and Klingenberg (1982) is presented and discussed in section 8.6 in the Appendix. The experimental results of Duyckaerts et al. (1980) are duplicated in Figure 4.3. With the developed model, I numerically reproduced these experimental results figures 4.4,4.5,4.6 and 4.7 respectively.

From the data Duyckaerts et al. (1980) proposed a mechanism for the ANT translocator which implies the formation of a ternary complex and proposed the explicit form for the flux as

$$v_o^{-1} = \frac{K_{AB}}{V}\frac{1}{[A][B]} + \frac{1}{V}. \tag{4.1}$$

From this relation it follows that the reciprocal of the initial rate of exchange as a function of the concentrations of ADP in the matrix and outside should be linear as shown by the straight line in Figure 4.3C. From this relation, they also estimated the parameters from their data 4.3C and obtained a value for K_{AB} of $(26.5 \pm 4.6)\cdot 10^{-3}$ mM^2. This value is in good agreement with our simulations leading to $27.84\cdot 10^{-3}$ mM^2 (Figure 4.7C).

Although the data was reproduced satisfactorily, the turnover rate of 0.1 sec^{-1} is two order of magnitude smaller than the rate measured in heart mitochondria (Duyckaerts et al., 1980; Chinopoulos et al., 2009). The experimental data of Kraemer and Klingenberg (1982) has two limitations: first, the experiments were done in liposomes and it is known that the lipid composition can affect the velocity of the translocator, and secondly only steady state transport can be measured. For improved model calibration, we therefore included a third experiment (Chinopoulos et al., 2009) in which the transient appearance of ATP within the medium was measured for isolated synaptic mitochondria. This allowed us to adjusted the rate of ATP translocation (k_p) in a way that the turnover rate is ~ 23 sec^{-1} as measured for synaptic mitochondria (Chinopoulos et al., 2009). For this purpose, I sought to reproduce the experimental conditions of Chinopoulos et al. (2009) where the concentration of ADP in the medium was 2 mM and of ATP 0.01 mM. The internal concentrations were set to 2.98 mM and 7.11 mM for ADP and ATP, respectively, based on estimations by Metelkin et al. (2009) while the effective concentrations used for the simulations were reduced as explained at the end of this section. For the simulations the number of ANTs present in the mitochondrion was set to 1000 and is smaller than the total number of ANTs estimated in a synaptic mitochondrion (also explained at the end of this section), but since the turnover rate per molecule was the relevant outcome, the smaller value was sufficient. To obtain a turnover rate of 23 sec^{-1}, the rate constant of the reaction DLT $\xrightarrow{k_p}$ TLD representing the productive cycle that exports ATP had to be in-

[1] I assumed liposomes are spheres of radius 100 nm with a volume of 0.004 μm^3, and estimated the number of ANTs on them as 100.

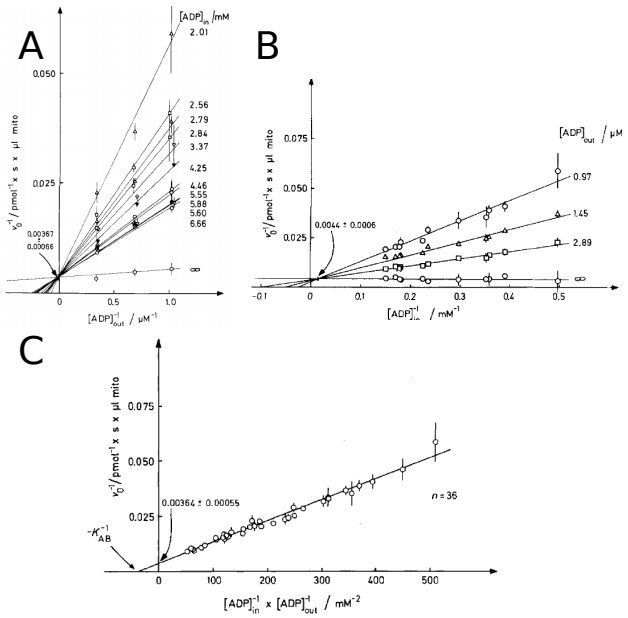

Figure 4.3: Experimental data reproduced from Duyckaerts et al. (1980), Fig. 3, 4 and 5. A) Reciprocal of the initial rate of ADP exchange as a function of the reciprocal of the external-ADP concentration. The initial rate were measured for three external ADP concentrations and eleven internal ADP concentrations. The lines were calculated by the method of least squares. B) Reciprocal of the initial rate of ADP exchange as a function of the reciprocal of the internal-ADP concentration. The initial rate were measured for three external ADP concentrations and eleven internal-ADP concentrations. C) Reciprocal of the initial rate of ADP exchange as a function of the reciprocal of $[ADP]_{in}[ADP]_{out}$. The values of v_o are from A. The parameter K_{AB} (equation 4.1) was fitted to $(26.5 \pm 4.6)\cdot 10^{-3}$ mM^2.

creased to 800 s^{-1}. Values in this order of magnitude have been also measured in transient experiments in liposomes (Gropp et al., 1999).

Final simulations

ADP and ATP can react with different cations, be bound or ionized. Therefore, the total concentration of ATP can be distributed in different compounds or states like ATP^{4-} or $ATPMg^{2-}$. These distributions can be estimated by coefficients representing the fraction of unbound ATP in the matrix of mitochondria or the external compartments. For our model, mitochondrial ADP^{3-} and ATP^{4-} concentrations were estimated analogously to the mitochondrial model of beta cells Magnus and Keizer (1997) as $[ADP]_{m,free} = 0.8\ [ADP]_m$, $[ATP]_{m,free}=[ATP]_m$, $[ATP^{4-}] = 0.05\ [ATP]$ and $[ADP^{-3}] = 0.45\ [ADP]_{free}$. For the final simulations presented in Chapter 6, the

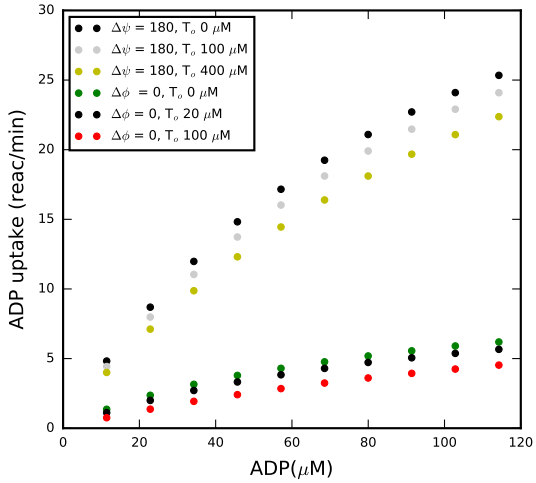

Figure 4.4: Reproduced experiments for the ANT I. ADP uptake rate vs external ADP concentration for a membrane potential ($\Delta\psi$) of 180 mV and ATP concentrations outside the liposomes of 0, 100, 400 μM shown by black, light grey and yellow points, respectively. Green, grey and red points describe the dependency for for membrane potential $\Delta\psi$) of 0 mV and concentrations of T_o of 0, 20, 100 μM, respectively. The concentrations of ADP and ATP inside the liposomes were 5 mM.

concentrations of ATP and ADP in the matrix were set to 2 mM and 10 mM, respectively, for an active mitochondrion, and to 0.01 mM and 2 mM in the cytosol based on previous estimations (Metelkin et al., 2009). The total number of ANTs in a mitochondrion can be estimated assuming a density of ANTs of 1.37 nmol/mg protein per dry mass (Chinopoulos et al., 2009) and 1 nmol/mg $\approx$ 1.25 mM (Magnus and Keizer, 1997). This translates into $\sim 2.10^4$ ANTs per mitochondrion given the volume of the here reconstructed mitochondrion.

The location of ANTs in mitochondria has not yet been definitively determined. Experimental evidence shows that they might form complexes with ATP synthases and phosphate carriers (Ko et al., 2003) on the CM (Wittig and Schägger, 2009; Vogel et al., 2006) but could also be associated with VDACs located in the IBM (Vyssokikh et al., 2001). In my simulations I explored the functional implications of these different locations by placing them (i) homogeneously distributed in the IBM (Figure 4.8A), (ii) colocalized with ATP synthase in the CM (Figure 4.8B), and (iii) in both locations.

Parameter	Value	Unit
$k^{b}_{T_i}$	$4{\cdot}10^{4}$	s^{-1}
$k^{f}_{T_i}$	$6.4{\cdot}10^{6}$	$M^{-1}s^{-1}$
$k^{b}_{T_o}$	200	s^{-1}
$k^{f}_{T_o}$	$4{\cdot}10^{5}$	$M^{-1}s^{-1}$
$k^{b}_{D_i}$	$4{\cdot}10^{4}$	s^{-1}
$k^{f}_{D_i}$	$4{\cdot}10^{6}$	$M^{-1}s^{-1}$
$k^{b}_{D_o}$	100	s^{-1}
$k^{f}_{D_o}$	$4{\cdot}10^{6}$	$M^{-1}s^{-1}$
k_p	4	s^{-1}
k_{cp}	0.75	s^{-1}
k_d	0.48	s^{-1}
k_t	0.58	s^{-1}
# ANTs	100	
$\Delta\phi$	-180	mV

Table 4.2: Chemical kinetic rate constants for the ATP/ADP translocator model for a membrane potential of 180 mV used to reproduce published data (Kraemer and Klingenberg, 1982; Duyckaerts et al., 1980).

Parameter	Value	Unit
$k^{b}_{T_i}$	$4{\cdot}10^{4}$	s^{-1}
$k^{f}_{T_i}$	$6.4{\cdot}10^{6}$	$M^{-1}s^{-1}$
$k^{b}_{T_o}$	200	s^{-1}
$k^{f}_{T_o}$	$4{\cdot}10^{5}$	$M^{-1}s^{-1}$
$k^{b}_{D_i}$	$4{\cdot}10^{4}$	s^{-1}
$k^{f}_{D_i}$	$4{\cdot}10^{6}$	$M^{-1}s^{-1}$
$k^{b}_{D_o}$	100	s^{-1}
$k^{f}_{D_o}$	$4{\cdot}10^{6}$	$M^{-1}s^{-1}$
k_p	0.7	s^{-1}
k_{cp}	0.75	s^{-1}
k_d	0.48	s^{-1}
k_t	0.58	s^{-1}
# ANTs	100	
$\Delta\phi$	-180	mV

Table 4.3: Chemical kinetic rate constants for the ATP/ADP translocator model for a membrane potential of 0 mV used to reproduce published data (Kraemer and Klingenberg, 1982).

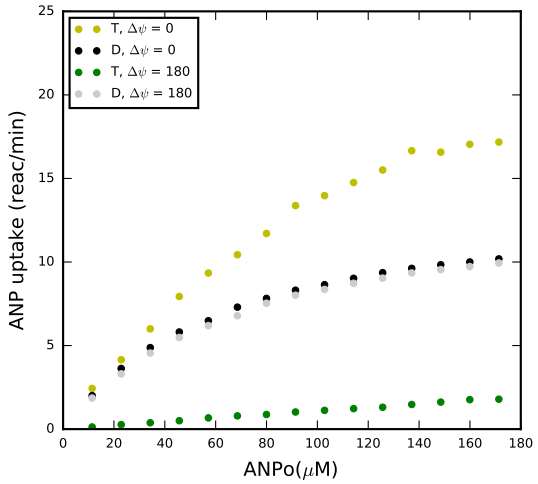

Figure 4.5: Reproduced experiments for the ANT II. ATP uptake rate vs external ATP concentration for a membrane potential ($\Delta\psi$) of 0 and 180 mV and no ADP are shown by yellow and green points, respectively. Black and grey points describe ADP uptake rate vs external ADP concentration for a membrane potential of 0 and 180 mV with a vanishing ATP concentration.

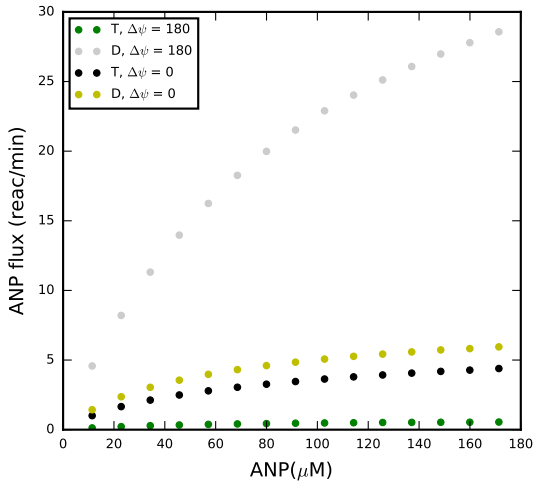

Figure 4.6: Reproduced experiments for the ANT III. ATP uptake rate vs ATP concentration, yellow and green points for a membrane potential ($\Delta\psi$) of 0 and 180 mV respectively, and ADP concentration equal to the ATP concentration. ADP uptake rate vs ADP concentration, black and grey points for a membrane potential of 0 and 180 mV respectively, and ATP concentration equal to the ADP concentration.

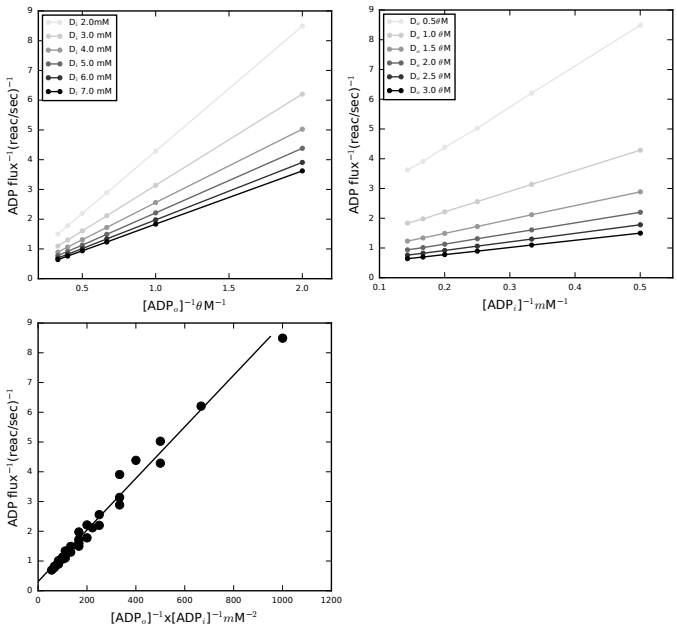

Figure 4.7: Reproduced experiments for the ANT IV. Qualitative reproduction of the experimental results of Duyckaerts et al. (1980). A) Reciprocal of the initial rate of ADP exchange as a function of the reciprocal of the external-ADP concentration. The initial rate were measured for three external ADP concentrations and eleven internal-ADP concentrations. The lines were calculated by the method of least squares. B) Reciprocal of the initial rate of ADP exchange as a function of the reciprocal of the internal-ADP concentration. The initial rate were measured for three external ADP concentrations and eleven internal-ADP concentrations. C) Reciprocal of the initial rate of ADP exchange as a function of the reciprocal of $[\mathrm{ADP}]_{\mathrm{in}}[\mathrm{ADP}]_{\mathrm{out}}$. The values of v_o are from A. The value for the parameter K_{AB} from our simulations is $27.84{\cdot}10^{-3}$ mM^2.

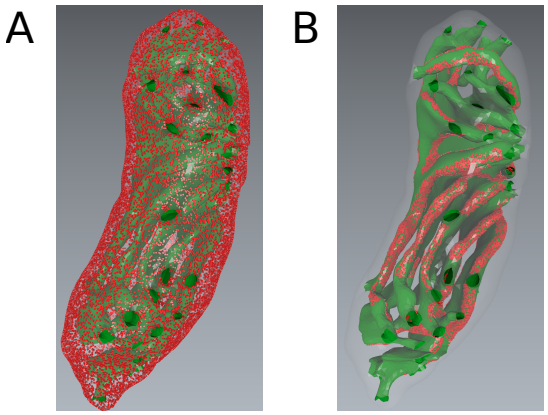

Figure 4.8: The location of ANTs in mitochondria has not yet been definitively determined. Therefore we explored the functional implications of different locations: (A) ANTs were either homogeneously distributed on the IBM, (B) co-localized with ATP synthases at the curvatures of tubular cristae and at the apex of lamellar cristae, or in both locations (not shown).

Parameter	Value	Unit
$k^{b}_{T_i}$	$4{\cdot}10^{4}$	s^{-1}
$k^{f}_{T_i}$	$6.4{\cdot}10^{6}$	$M^{-1}s^{-1}$
$k^{b}_{T_o}$	200	s^{-1}
$k^{f}_{T_o}$	$4{\cdot}10^{5}$	$M^{-1}s^{-1}$
$k^{b}_{D_i}$	$4{\cdot}10^{4}$	s^{-1}
$k^{f}_{D_i}$	$4{\cdot}10^{6}$	$M^{-1}s^{-1}$
$k^{b}_{D_o}$	100	s^{-1}
$k^{f}_{D_o}$	$4{\cdot}10^{6}$	$M^{-1}s^{-1}$
k_p	800	s^{-1}
k_{cp}	0.75	s^{-1}
k_d	0.48	s^{-1}
k_t	0.58	s^{-1}
# ANTs	2.10^{4}	
$\Delta\phi$	-180	mV

Table 4.4: Final chemical kinetic rate constants for the ATP/ADP translocator model for a membrane potential of 180 mV.

4.3 VDAC

In order to incorporate a process that exports ATP from the mitochondrion into the cytosol in my model, I include voltage dependent anion channels (VDACs), the main mechanism for metabolites to cross the OM (Mannella, 1998). As briefly explained in the introduction, the dynamics of this channel is rather complex including several close states and a peculiar dependence on the membrane potential. Unfortunately, I could not find models for the VDAC at the required level for the intended simulations since they were representing different scales such as all-atom molecular dynamics or free energy simulations (Noskov et al., 2016). Efforts to bridge from molecular dynamics to Markov state models seem to be underway (Noskov et al., 2014) but are not yet applicable. A realistic model would include another layer of complexity to the dynamics potentially delaying the exit of ATP, blocking the exit altogether in specific configurations or effect also the entrance of ADP. For this first version of my model, the aim was not to reproduce the complex dynamics of the channel but rather allow ATP molecules to exit the mitochondria. Therefore, I implemented a rather simple model of the VDAC assuming that the proteins interact with ATP and translocate it to the cytosol by the following reaction equation: $\mathrm{VDAC} + \mathrm{ATP}_{\mathrm{mito}} \rightleftharpoons \mathrm{VDAC} + \mathrm{ATP}_{\mathrm{cyto}}$.

In my simulations VDAC proteins were homogeneously distributed within the OM with a density of $10^4 \mu\mathrm{m}^{-2}$ based on experimental estimations (De Pinto et al., 1987). I set the rate constant of the reaction such that ATP molecules are not substantially delayed by the interaction with porin. I did simulations with ATP molecules diffusing from a spherical region in the interior of the IM to the cytosol with and without VDACs on the OM. Within 10 ms, almost all molecules reached the cytosol without the consideration of VDACs, but with VDACs and my given parameters only $\sim$ 75 % were entering the cytosol within the same period.

Parameter	Value	Unit
k	$1{\cdot}10^6$	$\mathrm{M}^{-1}\mathrm{s}^{-1}$
Density	$1{\cdot}10^4$	$\mu\mathrm{m}^{-2}$
$\mathrm{n}_{\mathrm{VDAC}}$	7100	

Table 4.5: Chemical kinetic rate constants for the VDAC model.

4.4 ATP-consuming reactions

To reflect physiological conditions, I emulated the arrival of an action potential at the terminal by varying the rate constant k of ATP-consuming reactions located at the synaptic membrane. I simulated the energetic response during a 5 ms lasting recovery phase between 2 spikes by modulating k_{cha} as step functions between the basal and active ATP consumption rates (Figure 4.9).

To set the parameter values of the ATP consuming reactions, I used the calculations by Attwell and Laughlin (2001) for the energy demand of glutamatergic signaling. From these considerations, they estimated a demand of 11,000 ATP molecules per released vesicle, 12,000 ATP molecules for related Ca^{2+} removal and $\sim$ 821 ATP molecules for endocytosis and exocytosis of vesicles. From the 11,000 ATP molecules needed for glutamate recycling, I only considered 1,333 (for the packing of glutamate in vesicles) since this is actually happening at the presynaptic terminal whereas the other processes are located within astrocytes. Thus, $\sim$ 14,000 ATP molecules are needed per vesicle released. For a firing frequency of 200 Hz and a release probability of 0.25, the total number of ATP molecules needed at the synapse equals $7 \cdot 10^5$ ATPs/s $(0.25 \times 200\mathrm{Hz} \times 1.4 \cdot 10^4)$.

To consider ATP consumption within the synapse, I placed channel molecules at the synaptic membrane which consume ATP by the reaction ATP $+$ channels $\xrightarrow{\mathrm{k_{cha}}}$ channels. For mimicking the action potential dependent ATP consumption, the reaction rate exhibits the form of two square pulses with a minimal and maximal value $\mathrm{k_{basal}}$ and $\mathrm{k_{max}}$, respectively. The values of $\mathrm{k_{max}}$ and the number of channels $\mathrm{n_{cha}}$ were set to match an ATP consumption rate of $7 \cdot 10^5$ ATPs/s. The basal level of ATP consumption reflects additional housekeeping processes and is given in Table 4.6. For the synaptic simulations, I assumed a spontaneous firing rate of 5Hz and vesicle release probability of 0.25 leading to a number of $\sim 1.8 \cdot 10^4$ ATP molecules per second needed at the synapse. The values of the rate constants were selected to not limit the reaction by diffusion.

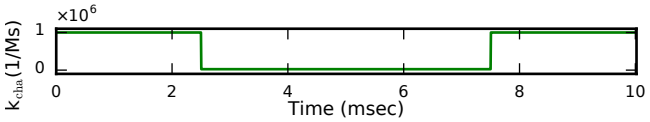

Figure 4.9: Rate constant of the ATP-consuming reactions. The initial value is $\mathrm{k_{basal}}$, and at 1 ms the action potential arrives at the synapse when the rate constant is increased to $\mathrm{k_{max}} = 1{\cdot}10^6$ $\mathrm{M^{-1}s^{-1}}$.

Parameter	Value	Unit
n_{cha}	$7{\cdot}10^5$	
k_{basal}	$2.5{\cdot}10^4$	$M^{-1}s^{-1}$
k_{max}	$1{\cdot}10^6$	$M^{-1}s^{-1}$
t^1_{on}	1	ms
t^1_{off}	5	ms
t^2_{on}	6	ms
t^2_{off}	10	ms

Table 4.6: Chemical kinetic rate constants for the ATP-consuming reactions.

4.5 Mitochondrial Calcium Uniporter

Dash and colleagues (Dash et al., 2009; Pradhan et al., 2010) proposed a six-state kinetic mechanism for Ca^{2+} transport into the mitochondria via the MCU. The proposed model is schematized in Figure 4.10. Free Ca^{2+} from the cytoplasmic (Ca^{2+}_o) or matrix (Ca^{2+}_i) side can bind to the protein complex L, to form either the $Ca^{2+}L$ or LCa^{2+} intermediate state. Another Ca^{2+} can bind to any of the aforementioned intermediate states forming a ternary complex with two Ca^{2+} bound. If they are both bound from the cytoplasmic side, the ternary complex is represented by $Ca^{2+}Ca^{2+}L$ whereas if they are both bound from the matrix side, the ternary complex formed is $LCa^{2+}Ca^{2+}$. The remaining case is $Ca^{2+}LCa^{2+}$ with one Ca^{2+} from each side. Transport occurs when a molecule in state $LCa^{2+}Ca^{2+}$ translates to $Ca^{2+}Ca^{2+}L$ that afterwards dissociates in two steps and liberates two Ca^{2+} ions and the protein complex L.

With a similar approach as in (Metelkin et al., 2006), Dash et al. (2009) assumed quasi-steady state, rapid equilibrium binding of Ca^{2+} to the membrane protein and derived a flux expression for Ca^{2+} in mitochondria with six unknown parameters. I used the revised version of the model presented in (Pradhan et al., 2010) and the corresponding fitted parameters. In particular, I useed this set of parameters from the paper: $k^0 = 1.42$ nmol/mgprot sec, $K^0 = 37.9$ μM , $\alpha = 0$, nH $= 2.65$, and from which I estimated some of the parameters needed for the simulations (Table 4.7). (Pradhan et al., 2010) set the parameter value of the rate constant of the reaction that brings calcium inside of the mitochondria $Ca^{2+}Ca^{2+}L \xrightarrow{k_{in}} LCa^{2+}Ca^{2+}$ as $k'_{in} = k_{in}$ [L] where [L] is the concentration of the uniporter. This value has been measured as ~ 0.001 nmol/mgprot, ~ 0.08 nmol/mgprot depending on the inhibitor used Reed and Bygrave (1974). Therefore the values of k_{in} (k'_{in}/[L]) are between 9537 s^{-1} to 763000 s^{-1}. A similar criteria was used to determined the value of k_{out}. The values chosen in our simulations were between these limits. The number of MCUs in the membrane was estimated using the density of channels per μm^2 estimated by (Kirichok et al.,

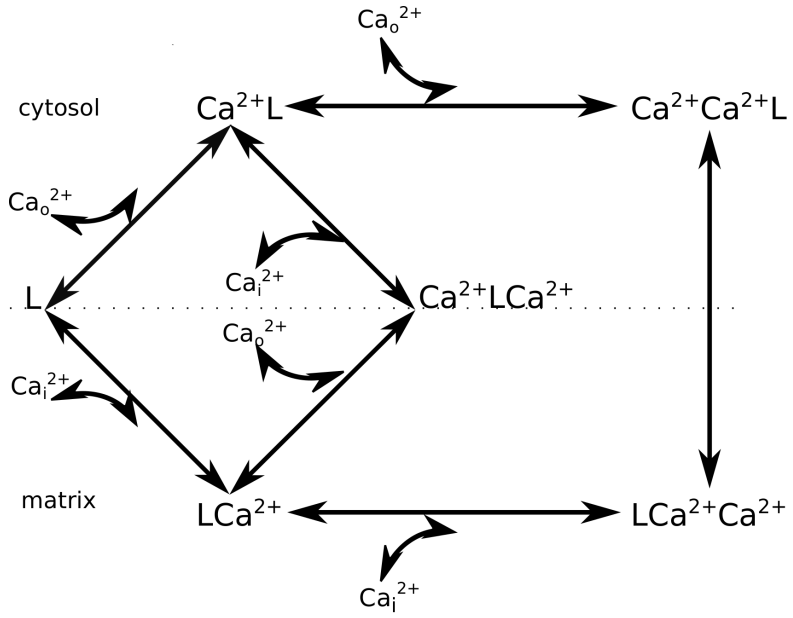

Figure 4.10: Markov chain model of the mitochondrial calcium uniporter. Kinetic model of calcium transport in mitochondria by a six-state mechanism. Free $\mathrm{Ca^{2+}}$ from the cytoplasmatic ($\mathrm{Ca_o^{2+}}$) or matrix ($\mathrm{Ca_i^{2+}}$) side can bind to the free protein complex L, forming the intermediate state $\mathrm{Ca^{2+}L}$ or $\mathrm{LCa^{2+}}$, respectively. Another $\mathrm{Ca^{2+}}$ ion can bind cooperatively forming a ternary complex of the form $\mathrm{Ca^{2+}Ca^{2+}L}$, $\mathrm{LCa^{2+}Ca^{2+}}$ or $\mathrm{Ca^{2+}LCa^{2+}}$. Transport of calcium to the matrix side occurs when the ternary complex $\mathrm{Ca^{2+}Ca^{2+}L}$ transitions to $\mathrm{LCa^{2+}Ca^{2+}}$.

2004). I reproduced the experimental results of (Vinogradov and Scarpa, 1973) for liver mitochondria. To subsequently transform the units of the fluxes, we adopted the conversion employed by (Williams et al., 2013) and estimated the flux on whole cell recordings. From the numerical simulations in MCell, this flux was calculated as $\mathrm{J_{uni}} = \mathrm{i_{uni}N_{mcu}N_{mitos}} \ / \ \mathrm{N_aV_{cyto}}$ where $\mathrm{i_{uni}}$ is the average number of net translocations per uniporter, $\mathrm{N_{mcu}}$ is the number of MCUs in the mitochondrion, $\mathrm{N_{mitos}}$ the number of mitochondria in a liver cell, $\mathrm{V_{cyto}}$ is the volume of the cytosol, and $\mathrm{N_a}$ the Avogadro's number.

As before we had to estimate the value of the forward ($\mathrm{k_f}$) and backward ($\mathrm{k_b}$) rate constant for $\mathrm{Ca^{2+}}$ binding from the equilibrium constant ($\mathrm{K = k_b/k_f}$). I did a parameter search changing the value of $\mathrm{k_f}$ from $1{\cdot}10^6$ $\mathrm{M^{-1}s^{-1}}$ to $1{\cdot}10^9$ $\mathrm{M^{-1}s^{-1}}$, increasing by one order of magnitude, and $\mathrm{k_b}$ from 37.6 $\mathrm{s^{-1}}$ to 37600 $\mathrm{s^{-1}}$ increasing also by one order of magnitude to keep the ratio constant. The simulations with a forward rate of $1{\cdot}10^8$ $\mathrm{M^{-1}s^{-1}}$, and a backward rate of 3760 $\mathrm{s^{-1}}$ reproduced the results at best. Interestingly, Williams et al. (2013) showed that several datasets from different groups give a similar flux as from (Vinogradov and Scarpa, 1973) with the proper conversion of units.

Parameter	Value	Unit
k^f	$1{\cdot}10^8$	$M^{-1}s^{-1}$
k^b	3790	s^{-1}
k_{in}	38162	s^{-1}
k_{out}	$1.74\,10^{-8}$	s^{-1}
$\Delta\phi$	-190	mV
# MCUs	188	
# Mitos per cell	$2{\cdot}10^4$	
V_{cyto}	18	pL

Table 4.7: Chemical kinetic rate constants and parameters for the MCU model.

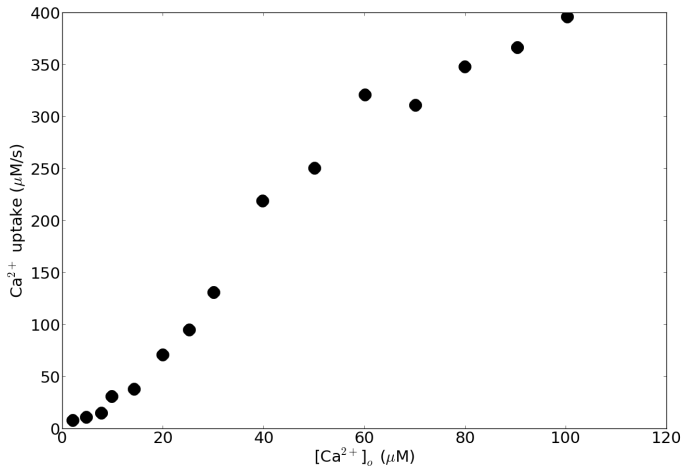

Figure 4.11: Experimental data reproduced from Vinogradov and Scarpa (1973), Fig.2. The units were transformed to represent whole cell recordings in liver cells, using the same conversion proposed by Williams et al. (2013).

Despite the successful reproduction of the experimental results, recent findings indicate that the MCU is not a transporter but obeys channel properties (Kirichok et al., 2004). To not introduce artifacts in our model, I decided to not incorporate the MCU implementation in the mitochondrion model but first to clarify the molecular mechanism and add the MCU at a future version of the model.

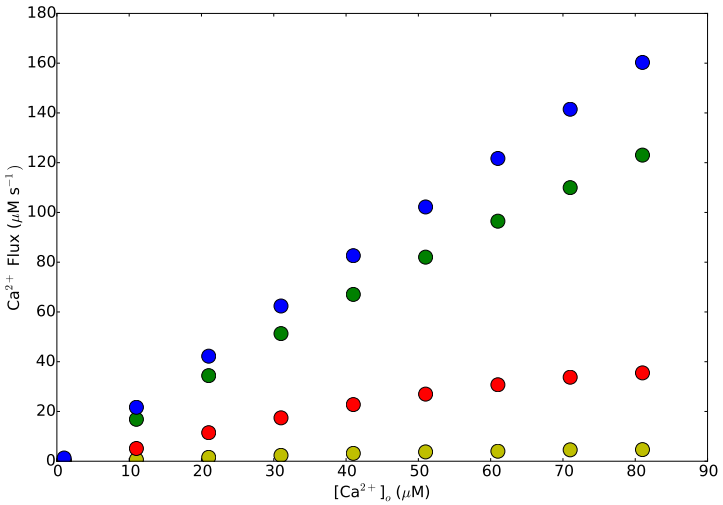

Figure 4.12: Reproduced experiments for the MCU. Qualitative reproduction of the experimental results of Vinogradov and Scarpa (1973) with a parameter search for the forward and backward rate constant for Ca^{2+} binding. The values are incremented one order of magnitude starting from $1{\cdot}10^{6}$ $\mathrm{M}^{-1}\mathrm{s}^{-1}$ and 37.6 s^{-1} respectively in yellow.

Chapter 5

Simulation Methods

As introduced in Chapter 1, life emerges across all different scales as a multiscale phenomenon. The embedding in space and time renders cells as complex reaction diffusion systems also at the subcellular level. The complex morphology of mitochondria reconstructed in Chapter 3 is pointing to potential spatiotemporal effect where the interplay of diffusion with active molecules like transporters, proton pumps and syntheses may have strong implications for the emergent dynamics in dependence on their spatial arrangement and the interaction with the environment. To address this open scientific question, I developed a realistic spatiotemporal mitochondrial model and a corresponding space independent approach to dissect the contribution of the different elements to the emergent dynamics. For this purpose, two different model formalisms were used to simulate the dynamics of the mitochondrion. One approach is based on stochastic spatial modeling using the particle-based simulator MCell, and the other model implementation is based on ODEs, i.e. essentially a deterministic and non-spatial approach. The deterministic formalism was mainly used to test the molecular implementation in MCell and to dissect the spatial effects. In Section 5.1 a brief summary of the MCell implementation is given, followed by a description of the space independent implementation in Section 5.2. Lastly, an overview of the three main *in silico* experiments performed is outlined.

5.1 Monte Carlo simulations

A number of formalisms can be use for biochemical simulations with different spatial and molecular resolution (see (Gupta et al., 2018) for an overview). Since we are dealing with a complex 3D geometry with small volume, we decided to implement the model using a particle-based simulator which, on the one hand, can consider the complex boundary conditions and on the other hand reflect the discrete nature of molecules for typical concentrations in such small volumes. Following these arguments, the com-

plex geometry can induce compartmentalization of molecules, confining molecules to smaller subvolumes, bringing the dynamics away of a well-stirred condition[1], and indicate that even stochastic effects might be relevant due to low molecule number in the confined spaces.
The software employed is MCell (Stiles et al., 1996; Stiles and Bartol, 2001; Kerr et al., 2008), a particle-based reaction-diffusion simulator that allows the specification of detailed cellular and subcellular structures. In MCell simulations, particles can diffuse in two and three dimensions, collide, and interact through bimolecular or unimolecular reactions. There are four basic elements of a simulation: movement, collision detection, bimolecular and unimolecular reactions each of which are briefly described below.

The individual trajectory of each molecule is generated by a Monte Carlo random walk. This movement is induced by translating the particles in discrete spatial steps by sampling the solution of the diffusion equation in radial coordinates for a point source of molecules defined by

$$\rho(r,t) = \frac{1}{(4\pi Dt)^{\frac{d}{2}}} \exp^{\frac{-r^2}{4Dt}}, \tag{5.1}$$

where D is the diffusion coefficient, t denotes time and d the dimension in which diffusion is embedded. The corresponding azimuthal angle ψ is determined by sampling from a uniform distribution between 0 an 2π while the polar angle θ is sampled from a sinusoidal probability distribution (see (Kerr et al., 2008) for more details).

Particles can also collide and if the distance between the molecules is smaller than a predefined collision radius they react. Collisions are detected by ray-tracing algorithms (Kerr et al., 2008). Bimolecular reactions occur stochastically accordingly to probabilities that depend on the reaction rate, the diffusion coefficient and the time step. For reaction between a surface and a volume molecule the probability takes the form

$$\rho = \frac{k}{A}(\frac{\pi \Delta t}{D})^{1/2}, \tag{5.2}$$

where k denotes the reaction rate and A the interface. The probability of reactions per collision should be chosen to be smaller than 1 to get accurate results (not greater than 0.5 to obtain errors less than 1-2% (Stiles and Bartol, 2001)). Unimolecular reactions can also occur where transitions are scheduled accordingly to the distribution of expected lifetimes (Equation 5.3), using Gillespie's stochastic simulation algorithm

$$\rho(t) = \frac{1}{k} \exp^{-kt}. \tag{5.3}$$

MCell uses Model description language (MDL) to define simulation inputs and outputs. MDL are text files with keywords, commands and parameters defined by the user. They have a modular structure with a section for model parameters such as geometry,

[1]This assumption implies that molecules are homogeneously distributed through space.

molecules and reactions that can be split in different MDL files. MCell also has a graphical user interface through its plug-in for Blender, called CellBlender. When a project is created using CellBlender the MDL files are generated automatically. This option was used for this project but after setting up the project all simulations and further modifications where done directly to the MDL files (in the Appendix B a brief description of these files is given). Moreover, a Python script was implemented to perform parameter sweeps by first modifying the MDL files with the parameter values and subsequently running the simulations from the command line.

The global time step for the simulations was set to 1 ns to have all reaction probabilities lower than 0.2 and to have the average diffusion length step at least half the minimal distance to resolve in the structure. I used the diameter of the cristae of $\sim$ 20 nm as the smallest distance to be resolved and the average diffusion length was with $\sim$ 0.3 nm way smaller than the minimal distance to resolve. The spatial granularity decreases while decreasing the temporal granularity because the average diffusion step depends on the time step (Stiles and Bartol, 2001).

The space is partitioned by a grid of 0.01 μm step to speed up the simulation time and the output data is saved every 100 ns. In order to obtain 10 ms of a simulation approximately 5 days of computing power were needed using an Intel Xeon processor CPU X5680 3.33GHz with 59G of memory. This could be reduced to 2.5 days with a Intel Xeon Gold 6146 processor 3.20GHz with 377G of memory.
MCell simulations can be stopped and restarted at any time through the use of *checkpointing*. Simulations can also be interrupted after a specific time, and then restarted from the same configuration. This has been widely used during these simulations to share resources and avoid premature terminations of the simulations with the consequent loss of results.

5.2 Ordinary differential equations

The simplest approach to model biochemical reaction dynamics is by ODEs. This level of description would treat the mitochondrion as a non-spatial object, where molecules are described as continuous populations under well-mixed assumption with no compartmentalization or spatial gradients. Cellular compartments can be included artificially by introducing distinct chemical species.

For each of the modules of the model, I derived a system of ODEs assuming mass action kinetics (Keener and Sneyd, 1998). I considered three compartments: the matrix, IMS and ICS (called outside), and the cytosol. The rate equations were integrated with the software package PyDSTool (Clewley, 2012; Clewley et al., 2007), an integrated simulation and analysis package for dynamical systems implemented in Python using a Radau integrator.

ATP synthase

The ODEs system for the ATP synthase model is given by

$$
\begin{aligned}
\frac{dE^{-3}}{dt} &= -k_{65}\,E^{-3} + k_{56}\,EH_3 + k_{16}\,{}^{-3}E - k_{61}\,E^{-3} \\
\frac{d\,{}^{-3}E}{dt} &= -k_{16}\,{}^{-3}E + k_{61}\,E^{-3} - k_{12}\,{}^{-3}E + k_{21}\,H_3E \\
\frac{dH_3E^*}{dt} &= -k_{45}\,H_3E^* + k_{54}\,EH_3 + k_{34}\,H_3ES - k_{43}\,H_3E^*\,D_i \\
\frac{dH_3ES}{dt} &= k_{43}\,D_i\,H_3E^* - k_{34}\,H_3ES + k_{23}\,H_3E\,T_i - k_{32}\,H_3ES \\
\frac{dH_3E}{dt} &= -k_{23}\,H_3E\,T_i + k_{32}\,H_3ES - k_{25}\,H_3E + k_{52}\,EH_3 + k_{12}\,{}^{-3}E - k_{21}\,H_3E.
\end{aligned}
\tag{5.4}
$$

where the variables E^{-3},${}^{-3}E$,H_3E^*,etc. describe the number of molecules in each state. The model has six states represented in the diagram of Figure 4.1. The total number of proteins $\mathrm{E_{tot}}$ is a conserved quantity, i.e. $\mathrm{E^{-3} + EH_3 + H_3E + H_3ES + H_3E^* + {}^{-3}E = E_{tot}}$. Thus, I derived 5 ODEs, one for each variable and the remaining one can be deduced from them. All parameters values are in Table 4.1.

ADP/ATP translocator

The ODEs system for the ADP/ATP translocator is given by

$$
\begin{aligned}
\frac{dL}{dt} &= -(k^f_{T_o}\,T_o + k^f_{T_i}\,T_i + k^f_{D_o}\,D_o + k^f_{D_i}\,D_i)\,L + k^b_{T_o}\,TL + k^b_{T_i}\,LT + k^b_{D_o}\,DL + k^b_{D_i}\,LD \\
\frac{dTL}{dt} &= k^f_{T_o}\,T_o\,L - (k^b_{T_o} + k^f_{D_i}\,D_i + 2k^f_{T_i}\,T_i)\,TL + k^b_{T_i}\,TLT + k^b_{T_i}\,TLT' + k^b_{D_i}\,TLD \\
\frac{dLT}{dt} &= k^f_{T_i}\,T_i\,L - (k^b_{T_i} + k^f_{D_o}\,D_o + 2k^f_{T_o}\,T_o)\,LT + k^b_{T_o}\,TLT + k^b_{T_o}\,TLT' + k^b_{D_o}\,DLT \\
\frac{dDL}{dt} &= k^f_{D_o}\,D_o\,L - (k^b_{D_o} + k^f_{T_i}\,T_i + k^f_{D_i}\,D_i)\,DL + k^b_{D_i}\,DLD + k^b_{D_i}\,DLD' + k^b_{T_i}\,DLT \\
\frac{dLD}{dt} &= k^f_{D_i}\,D_i\,L - (k^b_{D_i} + k^f_{T_o}\,T_o + k^f_{D_o}\,D_o)\,LD + k^b_{D_o}\,DLD + k^b_{D_o}\,DLD' + k^b_{T_o}\,TLD \\
\frac{dTLD}{dt} &= k^f_{D_i}\,D_i\,TL + k^f_{T_o}\,T_o\,LD - (k^b_{D_i} + k_{cp})\,TLD + k_p\,DLT - k^b_{T_o}\,TLD \\
\frac{dDLD}{dt} &= k^f_{D_o}\,0.5\,D_o\,LD + k^f_{D_i}\,0.5\,D_i\,DL - (k^b_{D_o} + k^b_{D_i} + k_d)\,DLD + k_d\,DLD' \\
\frac{dDLD'}{dt} &= k^f_{D_o}\,0.5\,D_o\,LD + k^f_{D_i}\,0.5\,D_i\,DL - (k^b_{D_o} + k^b_{D_i} + k_d)\,DLD' + k_d\,DLD \\
\frac{dTLT}{dt} &= k^f_{T_o}\,0.5\,T_o\,LT + k^f_{T_i}\,0.5\,T_i\,TL - (k^b_{T_o} + k^b_{T_i} + k_t)\,TLT + k_t\,TLT' \\
\frac{dTLT'}{dt} &= k^f_{T_o}\,0.5\,T_o\,LT + k^f_{T_i}\,0.5\,T_i\,TL - (k^b_{T_o} + k^b_{T_i} + k_t)\,TLT' + k_t\,TLT.
\end{aligned}
\tag{5.5}
$$

where the variables L, TL, LT describe the number of molecules in each state. One ANT can be found in one of the 11 states described in the diagram in Figure 4.2. I wrote 10 differential equations for the system, and used one conservation law for the total number of proteins ($\mathrm{L_{tot}}$), $\mathrm{L} + \mathrm{DL} + \mathrm{DLD} + \mathrm{DLD} + \mathrm{TL} + \mathrm{LT} + \mathrm{TLT} + \mathrm{TLT'} + \mathrm{DLT} + \mathrm{TLD} = \mathrm{L_{tot}}$ from which I deduced the number of molecules in the state DLT. $\mathrm{D_i}$ and $\mathrm{T_i}$ stand for the number of molecules of ADP and ATP in the matrix, $\mathrm{D_o}$ and $\mathrm{T_o}$ for the number of molecules outside, and $\mathrm{T_{cyto}}$ denotes the number of ATP molecules in the cytosol. The rate constants are labeled accordingly by the reactions they drive, e.g. for $\mathrm{T_o} + \mathrm{L} \rightarrow \mathrm{TL}$ the rate constant is $\mathrm{k^f_{T_o}}$ and for the reverse reaction $\mathrm{k^b_{T_o}}$. The reactions that translocate metabolites are: DLT $\xrightarrow{\mathrm{k_p}}$ TLD that brings ATP outside, TLD $\xrightarrow{\mathrm{k_{cp}}}$ DLT that brings ATP inside (and ADP outside), TLT $\xrightarrow{\mathrm{k_t}}$ TLT' that exports ATP from the inside to the outside, and vice versa. The latter reaction matters for example when ATP from the media is labeled and I used this flux to determine the parameter $\mathrm{k_t}$ using data from (Kraemer and Klingenberg, 1982). Something similar

occurs with the reaction DLD $\xrightarrow{\mathrm{k_d}}$ DLD' which is only useful when ADP is labeled outside or inside. Since I wanted the system to be equivalent with one state DLD, or two DLD and DLD', the rate constants of the forward reaction is half the values of the rate when one specie was considered. All the parameters of the ANT model are summarized in Table 4.2.

The rate constant of the bimolecular reactions have been normalized to have proper units to compute the number of particles, i.e. $\mathrm{k} = \frac{\mathrm{k'}}{\mathrm{N_a Vol}}$, where $\mathrm{N_a}$ is the Avogadro's number, and Vol represents the volume. Therefore, Vol is either the matrix volume or the volume of the outside space (ICS together with IMS).

ADP and ATP concentrations

I also derived equations for the number of ATP and ADP in the different compartments based on the ANT and ATP synthase dynamics resulting in

$$\begin{aligned}
\frac{dD_i}{dt} &= -(k^f_{D_i} L + k^f_{D_i} TL + k^f_{D_i} DL + k_{43} H_3E_o) D_i + k^b_{D_i} LD + k^b_{D_i} TLD + k^b_{D_i} DLD \\
&\quad + k^b_{D_i} DLD' + k_{34} H_3ES \\
\frac{dT_i}{dt} &= -(k^f_{T_i} L + k^f_{T_i} TL + k^f_{T_i} DL + k_{23} H_3E) T_i + k^b_{T_i} LT + k^b_{T_i} DLT + k^b_{T_i} TLT \\
&\quad + k^b_{T_i} TLT' + k_{32} H_3ES \\
\frac{dT_o}{dt} &= -(k^f_{T_o} L + k^f_{T_o} LT + k^f_{T_o} LD + k_p n_{vdac}) T_o + k^b_{T_o} TL + k^b_{T_o} TLD + k^b_{T_o} TLT \\
&\quad + k^b_{T_o} TLT' + k_p T_{cyto} n_{vdac} \\
\frac{dT_{cyto}}{dt} &= n_{vdac} k T_o - n_{vdac} k T_{cyto}.
\end{aligned} \tag{5.6}$$

Since I kept the concentration of ADP in the IMS constant, I did not considered an equation for the concentration of ADP there, neither for the concentration of ADP in the cytosol.

Calcium Uniporter

The MCU model has six states shown in the diagram of Figure 4.10. Here L denotes the free protein and again the total number of proteins $\mathrm{L_{tot}}$ is a conserved quantity, i.e. $\mathrm{L + LCa + LCaCa + CaL + CaCaL + CaLCa = L_{tot}}$. Therefore, I integrated five equations and LCaCa was derived from the conservation law. The ODEs system for

the kinetic diagram of the MCU reads

$$\begin{aligned}
\frac{dL}{dt} &= -(k_f\, Ca_o + k_f\, Ca_i)\, L + k_b\, CaT + k_b\, LCa \\
\frac{dCaL}{dt} &= k_f\, Ca_o\, L - (k_b + k_f\, Ca_o + k_f\, Ca_i)\, CaL + k_b\, CaLCa + k_b\, CaCaL \\
\frac{dLCa}{dt} &= k_f\, Ca_i\, L - (k_b + k_b + k_f\, Ca_o)\, LCa + k_b\, LCaCa \\
\frac{dCaLCa}{dt} &= k_f\, Ca_i\, CaL + k_f\, Ca_o\, LCa - 2k_b\, CaTCa \\
\frac{dCaCaL}{dt} &= k_f\, Ca_o\, CaL + k_{out}\, LCaCa - (k_b + k_{in})\, CaCaL
\end{aligned} \tag{5.7}$$

with parameters values given in Table 4.7.

5.3 In silico experiments

For the model establishment, I performed 3 distinct *in silico* experiments to disentangle the contribution of the different molecular components to the dynamics, presented in the next Chapter 6. In a first set of simulations, I started with a fixed number of ADP molecules and let them phosphorylate to ATP without any export or consumption of ATP. Hence, in this *isolated scenario*, ATP molecules accumulate in the mitochondrion. In a second configuration, I considered the mitochondrion to be embedded in a cube of dimension 0.45 μm^3 representing the cytosol with unlimited resources of ADP by clamping the concentration of ADP at the OM and included VDAC channels in the OM for mitochondrial export. The more *physiological scenario* of a fluctuating energy demand at a synapse is similar to the scenario of unlimited resources but with the mitochondrion located in the reconstructed synapse. ATP consuming reactions are included at the synaptic membrane representing ion channels activity, exocytosis and endocytosis of vesicles and glutamate recycling. To reflect the activation of the reactions due to action potential arrivals, I increased the reaction rate constant. The time trace of the rate constant is set by two square pulses with a basal value of $2{\cdot}510^4 M^{-1}s^{-1}$ and a maximum of $1{\cdot}10^6 M^{-1}s^{-1}$ (see Section 4.4 for details of the parameters estimation). For each configuration, I ran 10 individual simulations with different random seeds. Averaged trajectories were compared between configurations and compared with the spatially independent scenario described by the corresponding rate equations (ODEs).

Chapter 6

Results and discussion

To investigate the effect of mitochondrial morphology on the ATP production capacity, I systematically simulated different scenarios particularly for a synaptic mitochondrion. For this purpose, I reconstructed the morphology of an entire mitochondrion with unmatched precision and used this static geometry for dynamic simulations of the molecular interplay with spatially distinct molecular arrangements. I will start this chapter with a summary of results obtained from the reconstructed mitochondrion. This is followed by three sections where I describe three *in silico* experiments of increasing complexity designed to disentangle the contribution of the different molecular components to the dynamics. The first one, in Section 6.2, is an isolated scenario of equilibration, where an initial number of ADP molecules are imported to the matrix to be further subsequently phosphorylated to ATP, without any export or consumption of ATP. Next, in Section 6.3, the results of a more physiological conditions are presented, here I included VDAC channels and maintained the concentration of ADP in the OM. In the last experiment presented in Section 6.4, the mitochondrion is placed in the reconstructed synapse, and ATP consuming channels are added. In Section 6.5 I repeated the aforementioned experiments with a reduced diffusion coefficient. Finally, in Section 6.6, I analyzed how diffusive properties of molecules are affected by the morphology.

6.1 Mitochondrial morphology reconstruction

Due to technical reasons, detailed three-dimensional reconstructions of whole mitochondria are rare and accurate volume and surface measurements of mitochondria are lacking. I therefore initially focused on the comprehensive reconstruction of a synaptic mitochondrion from a serial electron tomogram volume. The resulting reconstruction was subsequently optimized to enable dynamic simulations and detailed morphological characterization (Table 6.1) including the volume of 0.04 μm^3 with a maximal length

of 0.8 μm and width of 0.29 μm and 45 cristae junctions. Based on the physiological classification of mitochondria (Figure 2.1), I determined the size of the different compartments where the IMS occupies approximately a relative volume to the outer membrane of 0.27, the matrix 0.52 and the ICS 0.21.
As it has been mentioned in the past (Perkins et al., 2001), I found a mixture of lamellar and tubular cristae in synaptic mitochondria, with tubular cristae located in the periphery and lamellar cristae in the central region of the mitochondria. This can also be appreciated in the distribution of CJs in three-dimensions, Figure 6.1.

The resulted reconstruction is shown in a Movie to appreciate the complex internal structure of synaptic mitochondria. In this movie, the OM is shown in white and after few seconds disappear, the IM is transparent blue and the CM is colored in green.

OM volume	0.039 μm^3
OM surface	0.651 μm^2
IM volume (matrix)	0.021 μm^3
IM surface	1.493 μm^2
IMS volume	0.011 μm^3
ICS volume	0.008 μm^3
IBM surface	0.54 μm^2
CM surface	0.953 μm^2
Number of CJs	45
Synapse volume	0.13 μm^3
Synapse surface	1.5 μm^2

Table 6.1: Properties measured on the reconstructed mitochondrion.

To get a better understanding of the small spaces generated by the cristae membrane, two figures were produced using CellBlender. In the first one the matrix of the mitochondria is filled with grey color, and the cristae are left emptied, to appreciate the interior a cross section of the mitochondrion is shown Figure 6.1B. In the second figure, the opposite is done, the cristae membrane is filled in grey and the matrix of the mitochondrion is left emptied, Figure 6.1C.

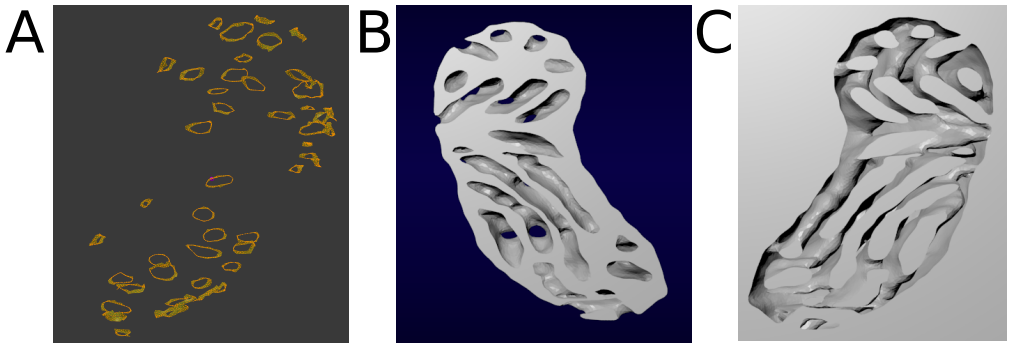

Figure 6.1: A) Distribution of cristae junctions on the mitochondrial IM. All the membranes were removed and only the cristae junctions are visible. An heterogeneous distribution is observed, with the cristae junctions located more in the periphery of the mitochondrion (also where the tubules are observed). B) Cross section of the mitochondrion with the matrix filled. The matrix of the mitochondrion is filled in grey color, and the cristae membrane is left empty. In order to make the interior visible a cross section of the mitochondrion is shown. C) Cross section of the mitochondrion with the cristae filled. The cristae are filled in grey color, and the matrix is left empty. A cross section of the mitochondrion is shown to make the interior visible.

6.2 Isolated Scenario of Equilibration

To investigate the effect of the morphology on the mitochondrial dynamics, I first considered a minimal configuration and simulated only the interplay between ANT and ATP synthase in dependence on their spatial arrangements (Figure 4.8). In this scenario, an initial number of 28,715 ADP molecules corresponding to a free ADP concentration of 900 μM in the IMS and ICS (referred together as outside) are imported into the matrix (Figure 6.2B,C) by 20,000 ANT molecules and subsequently phosphorylated to ATP by 3,800 ATP synthase according to the molecular reaction schemes (Figure 4.1). The generated ATP can be eventually exported into cristae and the IMS by ANTs (Figure 6.2D,E).

While the entire dynamical system obeys 21 variables (6 for ATP synthase, 11 for ANT and 4 for ADP and ATP concentrations within the 2 compartments), I focus here on the main readout of ATP and ADP molecules in the matrix and the outside space and give the remaining variables in Figure 8.7. During the equilibration process, I only observe minor differences between the different spatial arrangements within the first millisecond caused by diffusion induced delays (Figure 6.2B-E). Interestingly, differences to the spatially independent ODE system (black lines) are more pronounced when ANTs are co-localized with ATP synthase at the apex of the cristae (blue) because ADP molecules in the outside have first to diffuse within the cristae to be imported into the matrix by ANTs located in the CM (Figure 6.2B). Nevertheless, these differences are rather small and specifically the exported ATP does neither exhibit a significant dependence on morphology nor on the molecular spatial arrangement.

6.3 Non-equilibrium Induced Gradients

To investigate the mitochondrial dynamics under a more physiological non-equilibrium condition, I clamped the concentration of ADP at the surface of the OM to 900 μM , mimicking unlimited ADP resources in the cytosol. I next included VDAC channels in the OM (Figure 6.3A) to export ATP into the cytosol. For this extended model, I monitored again the main variables of the system including the amount of exported ATP in dependence on the different spatial arrangements and compared averaged trajectories with the corresponding ODE system (Figures 6.3B-F).

In this driven system, different ANT configurations obey distinct dynamics. When ANTs are distributed in the IBM (red), the ADP concentration outside is almost constant but for ANTs located in the CM (blue) an initial drop in the ADP concentration is caused due to a local depletion of ADP in the ICS (Figure 6.3B). Initially, all molecules of ADP are homogeneously distributed in the outside space consisting of IMS (the space between the OM and the IBM) and ICS. If ANTs are located in the IBM (red), ADP molecules are quickly bound to free ANT proteins but ADP molecules are immediately

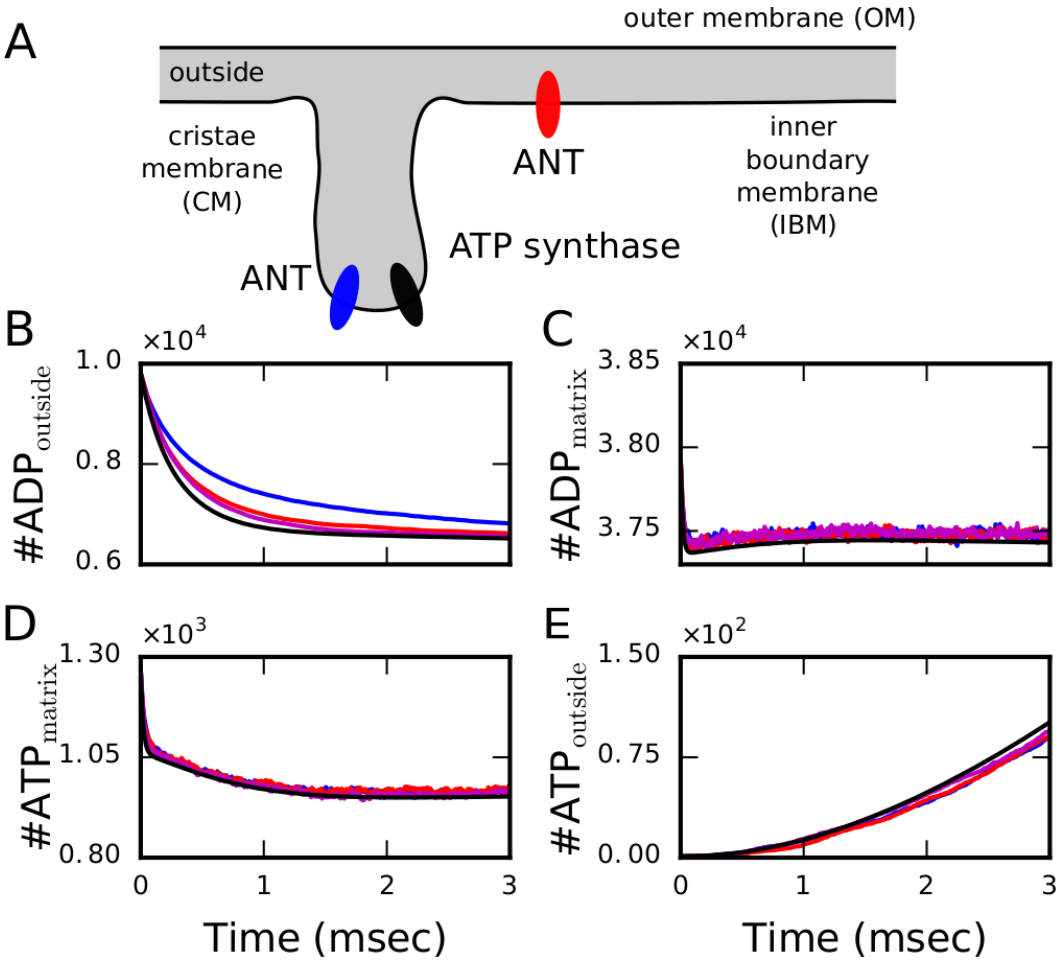

Figure 6.2: Isolated scenario of dynamic equilibration does not exhibit a strong dependence on the spatial arrangement. (A) Schematic representation of the considered components and their arrangement with ANTs either co-localized with ATP synthases in the cristae (blue), placed exclusively at the IBM (red) or in both locations (magenta). All trajectories are averaged over 10 different initial conditions and compared with the ODE system (black). (B) Simulations start with saturated ADP outside (900 µM) which is subsequently imported into the matrix (C) and phosphorylated to ATP (D). (E) After export of ATP from the matrix, it accumulates outside of the matrix. The different arrangements of ANTs do not exhibit significant differences with the corresponding ODE system.

replenished from the clamped membrane concentration. Hence no local gradients are formed. If ANTs are located in the CM exclusively (blue), ADP molecules in the ICS are quickly bound to free ANTs proteins and decrease the ADP concentration in the cristae volume. Thereby transitorily attracting more molecules from the IMS due to a concentration gradient. Since this replenishment relies on slow diffusion through tubular junctions (CJ) with small diameters ($\sim$ 25.5 nm in our reconstruction) connecting the cristae with the peripheral volume, the drop in the outside ADP is enhanced in amplitude as well as duration. To further characterize this scenario, I estimate the concentration traces in the IMS and the ICS (Figures 6.4B,C) indicating that the initially induced ADP gradient is reducing over time and represents the driving force for the persistent differences in the outside ADP between the different configurations (Figure 6.3B).

These differences in the outside ADP concentrations are accompanied with differences in the outside ATP concentration (Figure 6.3E) where more ATP is present in the outside if ANTs are distributed in the CM (blue). In this configuration, ATP molecules are exported into the cristae volume from where they first have to diffuse into the IMS to react with VDAC proteins in the OM to exit the mitochondrion. This diffusive transport takes longer compared to the scenario when ATP is directly exported to the peripheral volume (e.g. when ANTs are located in the IBM, red). Therefore, when ANTs are in the CM, there are more ATP in the outside space because they are held in the ICS for a longer period. To understand this interplay in more detail, I estimated the trajectories of ATP concentrations in the IMS and ICS (Figure 6.4F,G) and quantified the resulting gradients Figure 6.3G,H. The larger and negative ATP gradients between the OM and IBM when ANTs are located in the IBM (red) facilitate ATP transport towards the cytosol (Figure 6.3F) and deliver approximately double the energy amount compared to ANTs located in the CM. Remarkably, in this non-equilibrium scenario, the setup with ANTs in the IBM does not exhibit any major differences to the space independent ODE model whereas localization of ANTs in the cristae induce a diffusion limitation for cytosolic ATP export.

I estimated local ADP and ATP concentrations in the ICS, the inner boundary (IBM) and outer membrane space for the 3 different spatial arrangements (Figure 6.4). For this purpose, I counted with MCell the numbers of hits in an open region from which the concentrations can be estimated by assigning a small volume to this surface. In all configurations, the concentration of ADP is kept constant at the OM, Figure 6.4A.

An initial drop in the ADP concentration is observed within the ICS when ANTs are located in the CM as shown by the blue line in Figure 6.4C. The opposite holds for the ATP concentration which is persistently higher in the ICS due to the constant transport of ATP from the matrix to the cristae space (blue line in Figure 6.4G). I computed local concentration gradients between the inner boundary and outer membrane as well as between the cristae and the outer membrane (Figure 6.5). To calculate

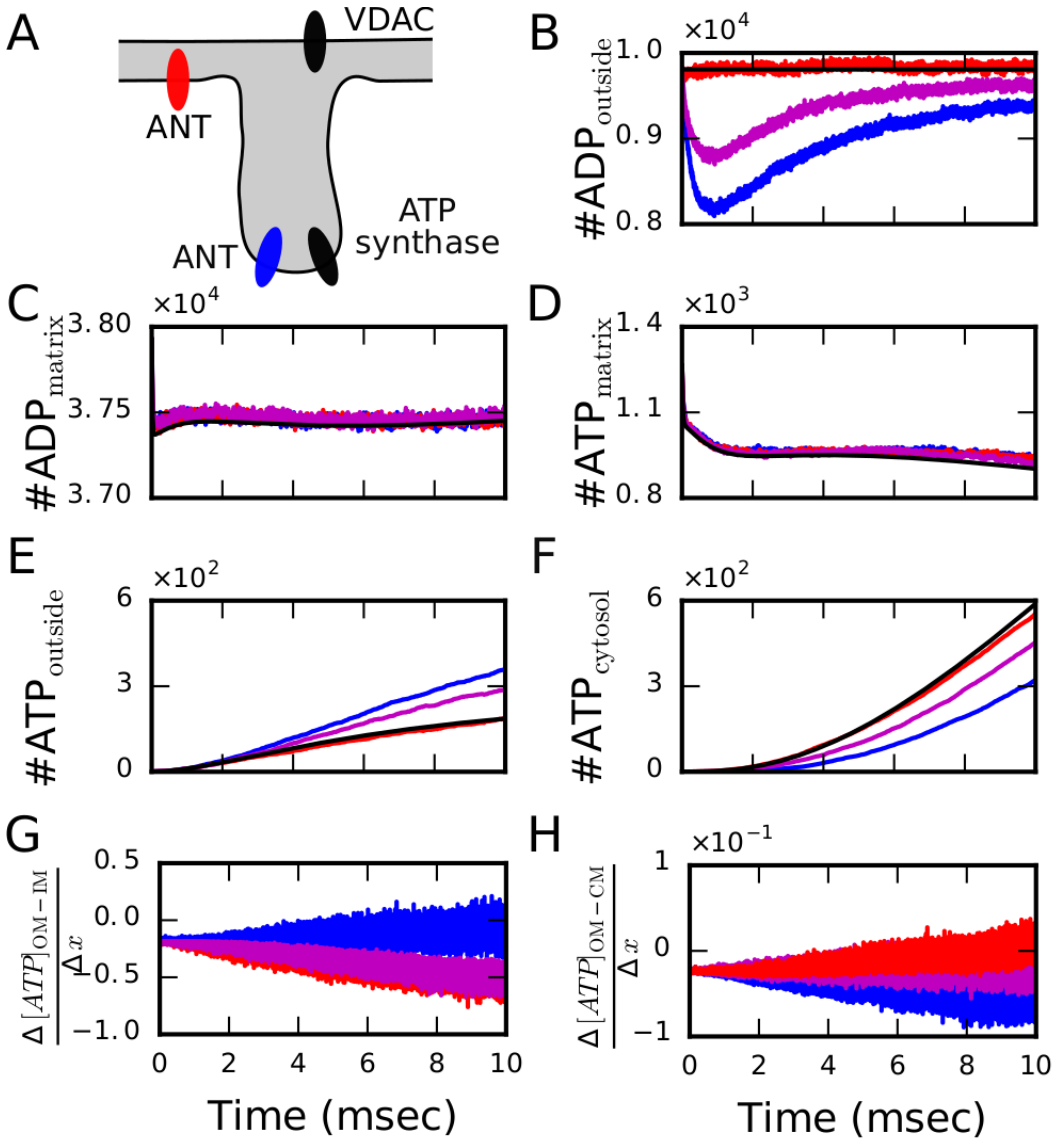

Figure 6.3: Non-equilibrium dynamics of the synaptic mitochondrion driven by clamped ADP concentration and ATP export. (*A*) Schematic representation of the components included in these simulations. (*B-H*) Comparison of averaged molecule trajectories for the distinct ANT localizations (ANTs homogeneously distributed in the IBM in red; ANTs colocalized with ATP synthase at the most curved region of the CM in blue; ANTs in both locations in magenta) with results of the ODE system (in black) exhibits most significant spatial effects for colocalization (blue) which are induced by sub-organelle ATP gradients (G,H).

these gradients, I measured the distance between the outer and inner membrane ($\leq$ 0.02 µm[1]) and between the middle of the mitochondrion to the outer membrane ($\sim$ 0.15 µm), respectively, by the Blender add-onMeasureit.

From the resulting data, I identified a strong gradient formed between the IBM and OM if ANTs are located in the IBM (grey line in Figure 6.5C) driving ATP export from the mitochondrion. In contrast, ATP import is observed in case ANTs are localized in the CM by an on average positive gradient (blue line in Figure 6.5C). In this case with ANTs localized in the CM, the gradient between the CM and the OM points to the exterior but is one order of magnitude smaller than the gradient between the IBM and OM. These observations underlay the results obtained in all different configurations.

6.4 Energy Production at a Presynaptic Terminal

After model establishment and finding significant differences in the cytosolic ATP production in dependence on the spatial arrangement, I was interested in potential physiological consequences of morphology on the synaptic dynamics. For this purpose, I investigated the ATP production rate of the mitochondrion in its physiological context, the presynaptic terminal (Figure 6.6A), and included ATP consuming reactions in the cytosol. To reflect physiological conditions, I considered ADP saturation within the cytosol and mimicked the arrival of an action potential at the terminal by varying the rate constant k of the ATP consuming reactions located at the synaptic membrane. Based on estimations of the energetic costs of a glutamatergic synapse, I set the basal ATP consumption rate to $k_{\mathrm{cha}} = 2.5 \cdot 10^4$ (Ms)$^{-1}$ and the energy demand during an action potential to $k_{\mathrm{cha}} = 1 \cdot 10^6$ (Ms)$^{-1}$ (see Section 4.4 for parameter estimation). To study how synaptic activation induces a transient transition between the approximated steady states for the different scenarios (Figure 6.6B-F), I simulated the energetic response during a 5 ms lasting recovery phase between 2 spikes by modulating k_{cha} as step functions between the basal and active ATP consumption rates (Figure 6.6G).

In contrast to the previous non-equilibrium scenario, the physiological simulation of the energetically dynamic presynapse started close to steady state condition determined by the ODE system. Therefore, I did not observe an initial dip in the outside ADP concentration (Figure 6.6B) but the formation of a stable gradient that drives the differences among the distinct configurations. Due to ADP clamping, the outside ADP concentration stays constant for the ODE approach and similarly for the scenario where ANTs are localized in the IBM (black and red in Figure 6.6B, respectively), whereas for ANTs exclusively or partly localized in the cristae, a slight drop is observed (blue and magenta in Figure 6.6C, respectively). Interestingly, ADP as well as ATP

[1]The maximal distance between the IBM and the OM is 0.02 µm but membranes also get closer to each other. Hence, estimated values of gradients represent lower bounds.

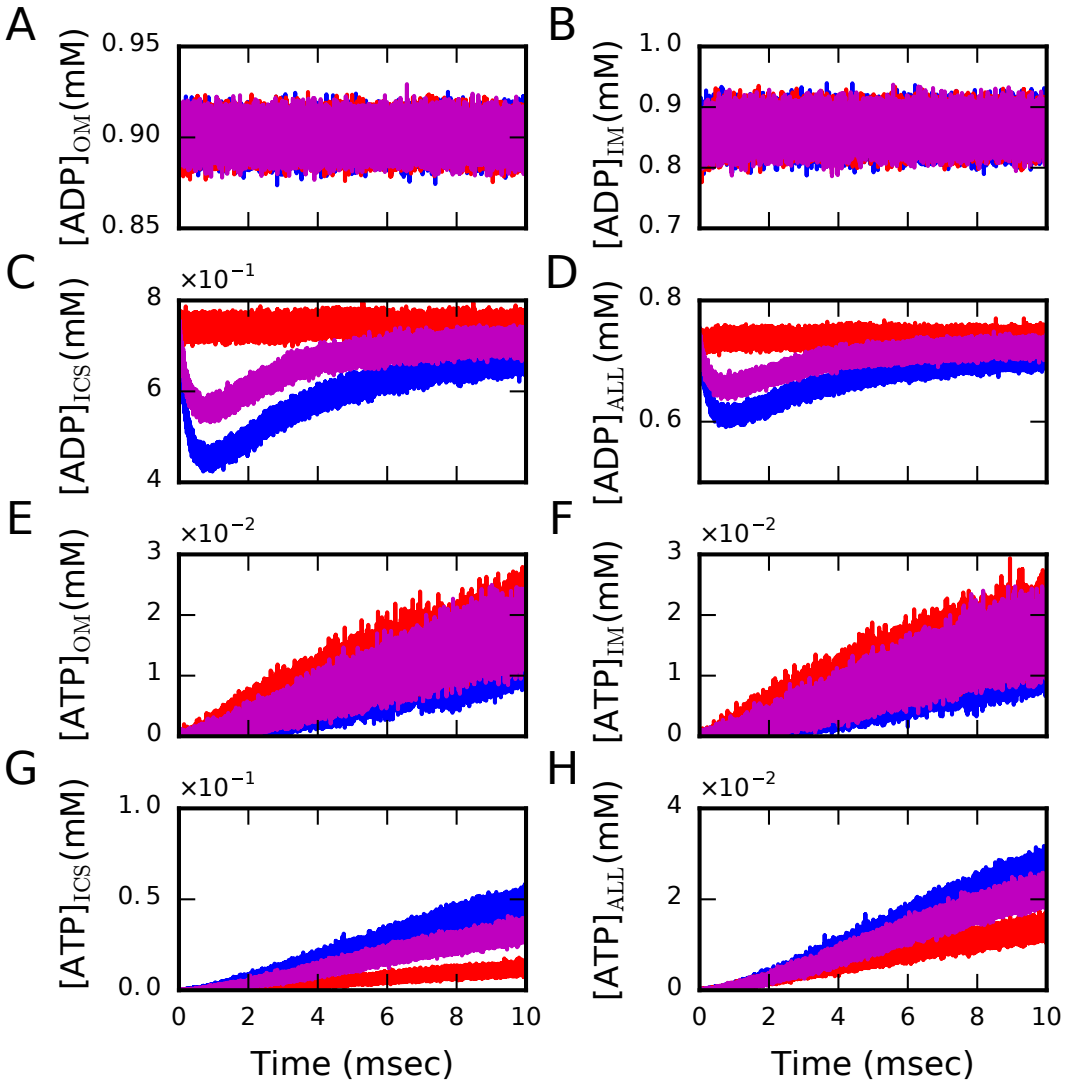

Figure 6.4: Non-equilibrium dynamics of the synaptic mitochondrion driven by clamped ADP concentration and ATP export - Local concentrations. I estimate the concentration of ADP (A-D) and ATP (E-H) in the cristae, inner boundary and outer membrane. Counting the number of hits the surface suffers and approximating a small volume close the it. As before, ANT molecules were placed in three different locations: in red, ANTs homogeneously distributed in the IBM; in blue, ANTs colocalized with ATP synthase at the most curved region of the CM; and in magenta, ANTs in both locations.

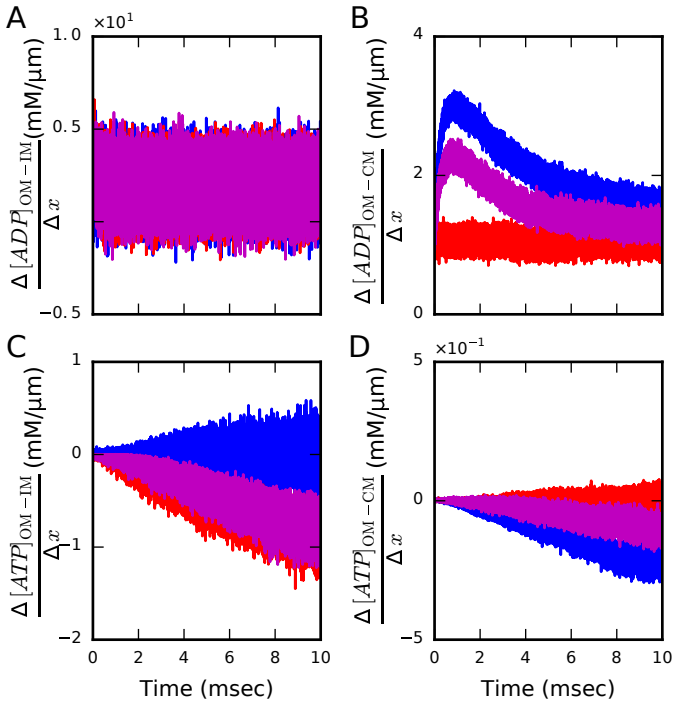

Figure 6.5: Non-equilibrium dynamics of the synaptic mitochondrion driven by clamped ADP concentration and ATP export - Local gradients. I estimate the concentration gradients of ADP (A-B) and ATP (C-D) form between the inner boundary and outer membrane (A and C), and between the cristae and outer membrane (B and D). To calculate the gradients the distance used and measured between the inner boundary and outer membrane is ∼0.02 μm, and the distance from the middle of the mitochondrion to the outer membrane ∼0.15 μm is used to compute the other gradient. ANT molecules were placed in three different locations: in red, ANTs homogeneously distributed in the IBM; in blue, ANTs colocalized with ATP synthase at the most curved region of the CM; and in magenta, ANTs in both locations.

concentration in the matrix are slightly increased consistently for all spatial simulation compared to the ODE approach (Figure 6.6C-E).

The most predominant difference is subsequently observed in the outside ATP concentration where localization of ANTs in the IBM again exhibit similar concentrations as the ODE system whereas localization of ANTs in the cristae lead to substantially increased ATP levels (red and blue in Figure 6.6E, respectively). As in the non-equilibrium scenario, this increase is caused by ATP within the ICS from where it first has to diffuse to the IMS for subsequent export into the cytosol. Hence, the cytosolic ATP is slightly lower for ANTs located in the cristae compared to ANTs in the IBM (blue and red in Figure 6.6F). Despite this difference, all spatiotemporal scenarios exhibited consistently smaller ATP amounts within the synapse during the recovery period with low energy demand compared to the ODE simulations (24% less for co-localization vs 10% less for IBM localization). After synaptic activation, the spatiotemporal simulations displayed a slower decrease in synaptic ATP and reduced differences in the ATP concentration between base level and activation conditions (relative change of 0.87 for co-localization vs 0.88 for IBM localization vs 0.97 for ODE). These results together indicate that ATP molecules can be buffered by the complex morphology and support adaptation to variable conditions.

The presynaptic model was used to calculate net ATP production rates from the second peak in Figure 6.6F. For ANTs located in the IBM I calculate a rate of $\sim$31 molecules/ms slightly reduced compared to the ODE system ($\sim$38 molecules/ms). The model with ANTs exclusively in the CM exhibits a rate of $\sim$ 26 molecules/ms. Comparison with theoretical estimations (see Appendix A, Table 7.1) and approximations in the literature exhibit good agreement.

Finally in this movie, we also show the reconstructed synapse, and an artificial digital slice of the tomogram (the thickness is artificial), we also included ATP molecules and ANTs in the cristae membrane. This movie corresponds to a real simulation, with the same conditions as in this experiment, it corresponds to the first millisecond of the simulations (the time step of the visual representation is 5 µs).

6.5 Reduced diffusion

ATP and ADP molecules are present in an ionized form in neutral solutions what may induce an additional reduction of diffusion. Here, I explore the effect of a smaller diffusion coefficient on the dynamics. I performed analogous simulations for the 3 different scenarios described before but with a diffusion coefficient one order of magnitude smaller $\mathrm{D} = 1.5 \cdot 10^{-8}\ \mathrm{cm^2 s^{-1}}$. For this diffusion coefficient, substantial differences are observed in almost all cases (Figures 6.7, 6.8 and 6.9). Remarkably, significant less ATP molecules (only $\sim$ 47) reached the cytosol after 10 ms when ANTs were located in the CM (blue line in Figures 6.8E). When ANTs were located in the IBM,

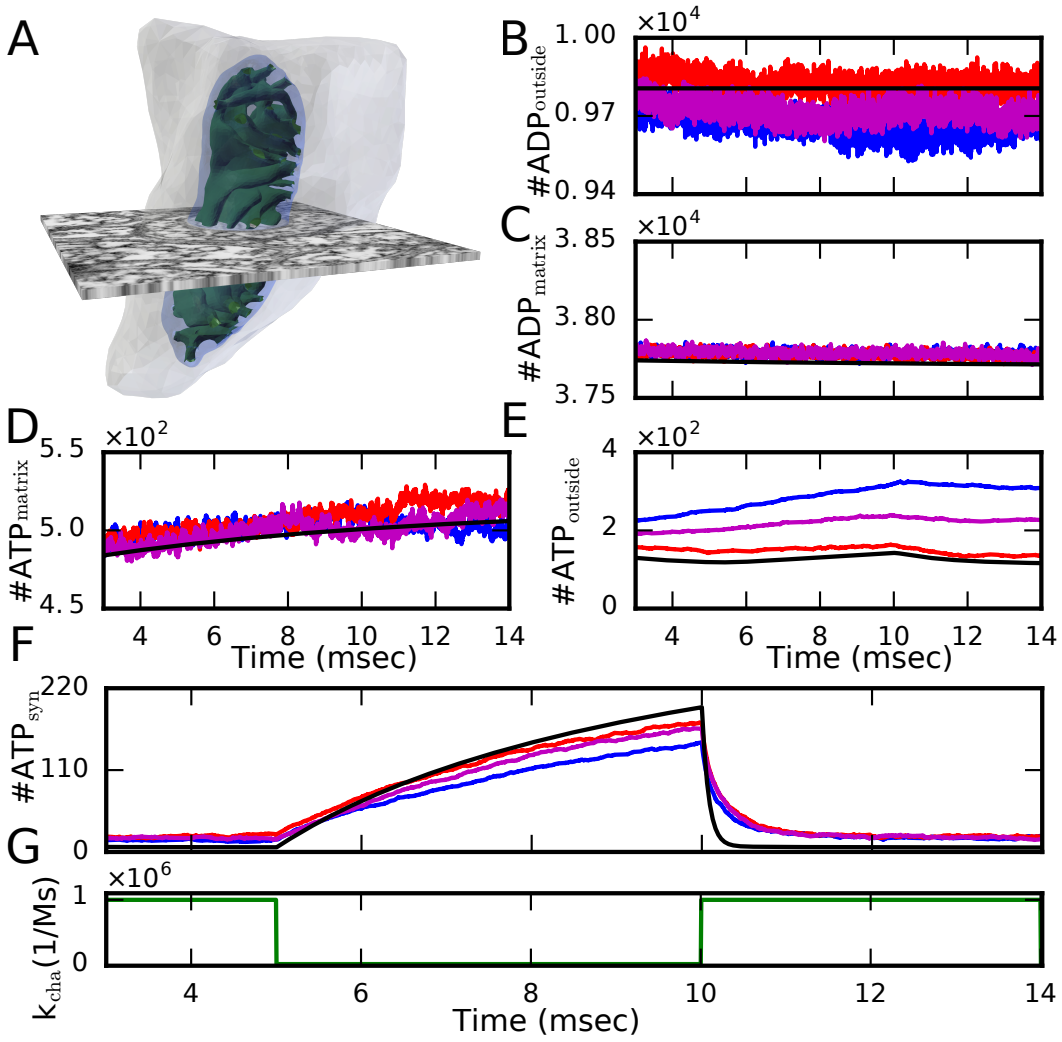

Figure 6.6: The energy source of a presynaptic terminal. Comparison of averaged trajectories of the number of molecules in different compartments with the results obtained with the ODE system. In this configuration, the mitochondrion is placed in the synapse where it was found (A) and I consider ATP consuming reactions. They are activated recreating the arrival of an action potential to the presynaptic terminal, emulated by the increase of the rate constant of the ATP consuming reactions (G). As before, the concentration of ADP in the OM is clamped and I include VDAC channels in the OM. ANT molecules were placed in three different locations: in red, ANTs homogeneously distributed in the IBM, in blue, ANTs colocalized with ATP synthase at the most curved region of the CM, and in magenta, ANTs in both locations. In black are the results of the ODE system.

$\sim$ 354 ATP molecules reached the exterior during the same period of time (grey line in Figures 6.8E). This diffusion limitation based effect was also found for faster diffusion but reduced diffusion is amplifying the differences between configurations.

Based on these simulations, I could estimate the rate at which ATP becomes available within the cytosol what is severely delayed under diffusion limitation conditions (Figure 6.9). For ANTs placed in the IBM, the ATP rate is 38 molecules per millisecond, and for ANTs in the CM the rate reduces to 11 molecules per millisecond whereas the rate for the spatially independent ODE yields 62 molecules per millisecond. If diffusion is reduced, the location of ANTs have a tremendous impact on the rate at which ATP can reach the cytosol and thus on the rate of energy supply at the synapse.

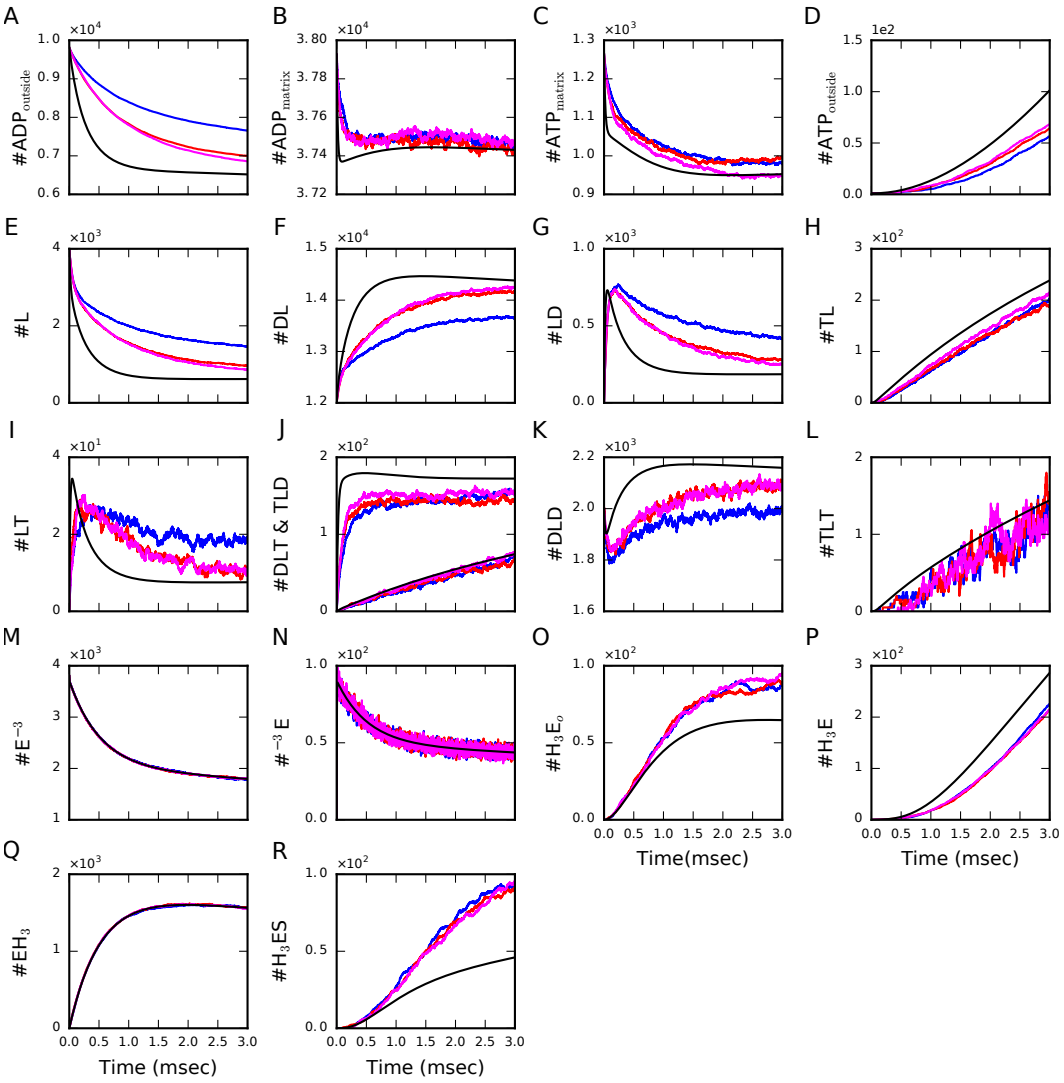

Figure 6.7: Concentration dynamics and variables for the isolated scenario of dynamic equilibration with reduced diffusion. ANTs molecules were again placed in three different locations: ANTs homogeneously distributed in the IBM (red), ANTs colocalized with ATP synthase at the most curved region of the CM (blue) and ANTs in both locations (magenta). Panels A-L show variables of the ANT model and panels M-R the variables of the ATP synthase model.

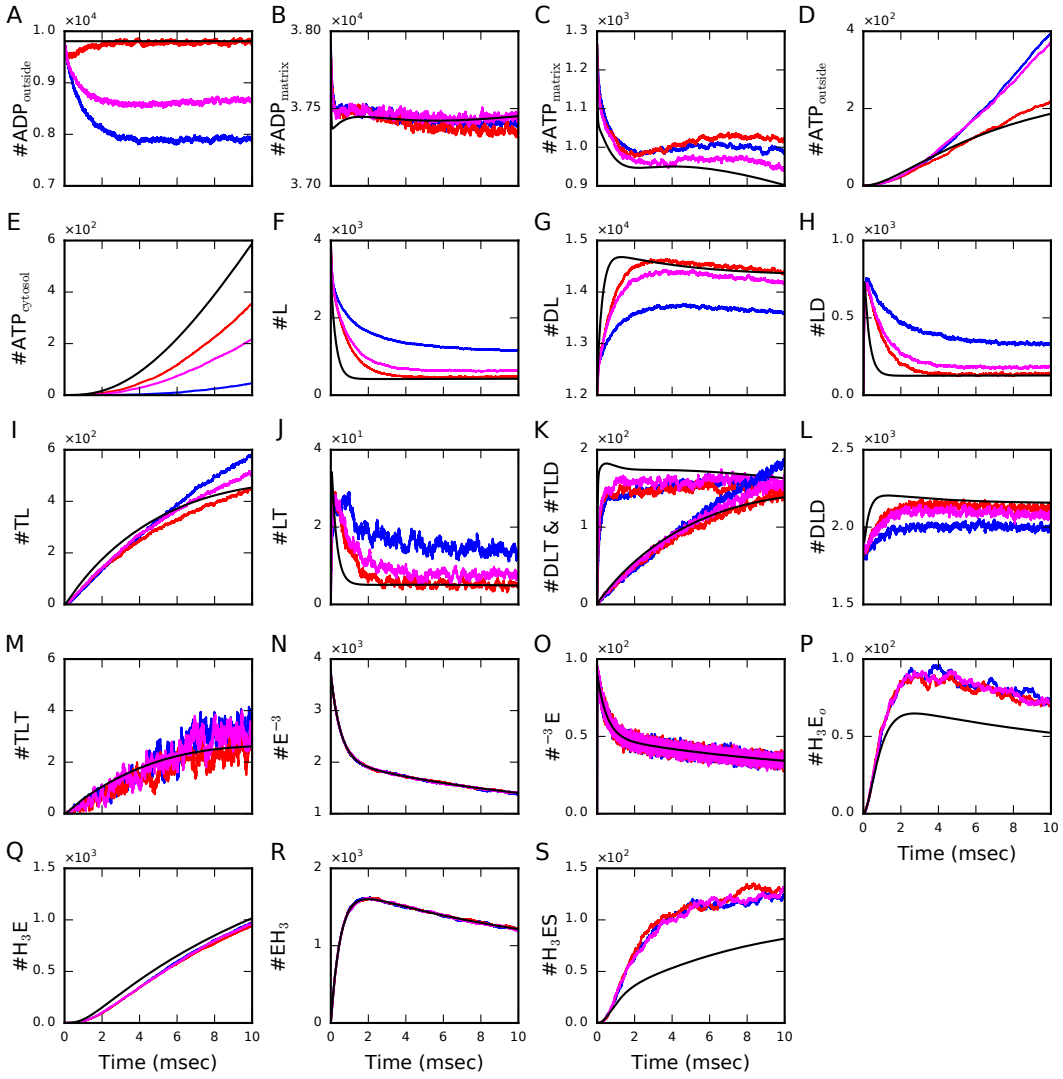

Figure 6.8: Concentration dynamics and variables for the non-equilibrium dynamics of the synaptic mitochondrion driven by clamped ADP concentration and ATP export with reduced diffusion. Comparison of averaged molecule number trajectories for the distinct ANT localizations (ANTs homogeneously distributed in the IBM (red), ANTs colocalized with ATP synthase at the most curved region of the CM (blue) and ANTs in both locations (magenta)) with results of the ODE system (black) exhibits a most significant spatial effects for colocalization (blue). Panels (A-L) show variables of the ANT model and panels M-R variables of the ATP synthase model.

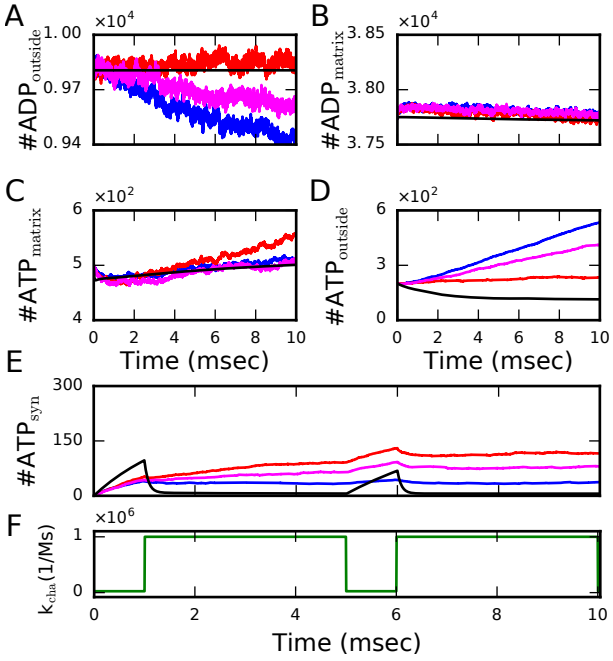

Figure 6.9: The energy dynamics of a presynaptic terminal with reduced diffusion. Comparison of averaged trajectories of the number of molecules in different compartments with the results obtained by the ODE system. In this configuration, the mitochondrion is placed in its physiological context, the presynaptic terminal, and ATP consuming reactions were considered to mimic the arrival of an action potential at the terminal. For this purpose, I emulated the increase of the rate constant of the ATP consuming reactions (F). As before, the concentration of ADP in the OM was clamped and VDACs were included in the OM. ANT molecules were placed in three different locations: ANTs homogeneously distributed in the IBM (in red), ANTs colocalized with ATP synthase at the most curved region of the CM (blue) and ANTs in both locations (magenta). The results of the ODE system are shown in black.

6.6 Anomalous diffusion

The extreme mitochondrial morphology has evoked a scientific discussion on diffusion properties within the organelle. Combining mathematical models and experimental data, the diffusive properties of proteins in the mitochondrial matrix have been measured (Partikian et al., 1998; Dieteren et al., 2011) and simulations of diffusion in obstructed objects suggested anomalous diffusion within organelles (Ölveczky and Verkman, 1998). To test this hypothesis, I used here our physiologically realistic reconstruction and simulated particle diffusion within the interior of the mitochondrion with and without the consideration of the internal structure (cristae membrane). From the resulting particle trajectories, I computed the mean-square displacement (MSD) of the molecules in both configurations. For normal diffusion, the MSD obeys Fick's law and equals $6\,\mathrm{D}\,\mathrm{t}$ where D is the diffusion coefficient (set to $\mathrm{D} = 1.5 \cdot 10^{-7}\ \mathrm{cm^2 s^{-1}}$) and t represents time. In particular, this relation predicts a linear dependence of the MSD on time t.

I compared this theoretical prediction with the MSD measured in simulations with and without internal structure (Figure 6.10). For the comparison, I calculated the linear regressions of the measured MSD in both configurations and determined the slopes. The slope of the theoretical prediction for Fick's law in an open space is $9 \cdot 10^{-7}\ \mathrm{cm^2 s^{-1}}$ whereas I measured $4.65 \cdot 10^{-7}\ \mathrm{cm^2 s^{-1}}$ and $4.07 \cdot 10^{-7}\ \mathrm{cm^2 s^{-1}}$ for simulations without and with considering the internal structure, respectively. While the deviation on the large time scale is caused by the closed space of the mitochondrion, the deviation on the shorter time scale is influenced by the internal structure. To quantify the anomalous diffusion, we considered the non-linear growth of the MSD in time ($6\,\mathrm{D}_\gamma\,\mathrm{t}^\gamma$) and fitted the γ exponents and amplitudes in both configurations (Figure 6.10). We obtained a value 0.85 in case of considering the internal structure and 0.84 without this consideration. The values were obtained for simulations run for 0.5 milliseconds (the coefficients and amplitudes depend on the length of the simulations).

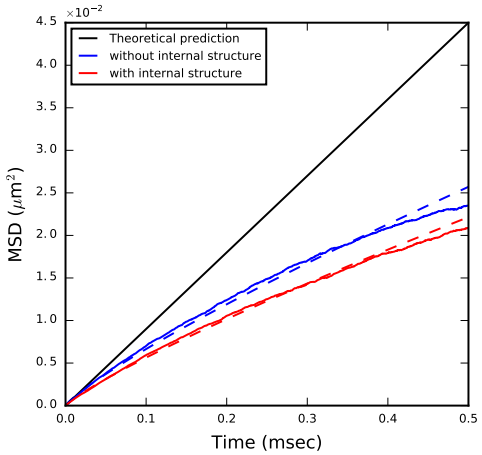

Figure 6.10: Time courses of the mean square displacement (MSD) for particles diffusing in the matrix, in blue without considering the internal structure and in red with the internal structure. Initially, 2500 particles were distributed homogeneously in the matrix, and their position was tracked to afterwards compute the MSD for both configurations. The dash lines represent a power law fitting of the data. The black line is the theoretical prediction of the MSD for normal or Fickian diffusion.

Chapter 7

Conclusions and perspectives

Mitochondrial morphology is thought to be context dependent and a mechanism to adapt to specific energetic requirements (Scalettar et al., 1991; Mannella, 2006). Mitochondria in the brain and specifically at synapses exhibit rather unique and complex morphologies (Perkins et al., 2001, 2010) that may reflect the high energy demand for neuronal information transmission (Attwell and Laughlin, 2001). Since the internal structure of mitochondria can be only resolved by EM tomography, a mechanistic understanding of how morphology is affecting mitochondrial dynamics relies on mathematical modeling to simulate dynamic consequences from the static images.

While modeling approaches have estimated the morphological effect on the mitochondrial membrane potential (Song et al., 2013) and diffusion properties based on simplified geometries (Dieteren et al., 2011; Ölveczky and Verkman, 1998), the consequences for the main function of ATP production of a real physiological morphology is only vaguely understood. Here, I used an electron tomogram of a presynaptic terminal in mouse cerebellum to (i) comprehensively reconstruct and analyze in detail the morphology of an entire mitochondrion (Chapter6, Table 6.1) and to (ii) subsequently investigate the dynamic consequences of the interplay between the complex morphology the spatial molecular orchestration by my developed computational model based on the mitochondrial morphology and molecular properties of the main adenosine phosphate processing molecules.

Surprisingly, simulations of the isolated scenario without any ADP import from and ATP export into the cytosol do not exhibit a strong dependence on the spatial arrangement (Figure 6.2) indicating that the assumed diffusion properties do not lead to a diffusion limiting condition. In accordance with theoretical considerations, comparing the timescales of diffusion and reactions indicated only a slight overlap for this scenario (Appendix A, Section 8.8). A morphological effect on ATP production could only be found for diffusion coefficients decreased by two orders of magnitude. Although some studies (Scalettar et al., 1991; López-Beltrán et al., 1996; Dieteren et al., 2011) showed evidence of severe hindrance of diffusion in the matrix, more recent experiments

estimated that diffusion is only three to four fold smaller than in water (Partikian et al., 1998). I reduced the diffusion coefficient of ATP and ADP, in my model, by one order of magnitude to reflect their ionized form and related interactions with other charged particles. The potential interaction of the ions with the membrane potential leading to electro-diffusion are not included in the current model but could actually decrease diffusion further and induce a regime of diffusion limitation. Independent of the diffusion limitation, my simulations indicated anomalous diffusion in agreement with previous evidences (Ölveczky and Verkman, 1998).

Although diffusion had only a minor effect in the isolated system, spatial aspects became significant when bringing the mitochondrion in contact with the cytosol under unlimited access to ADP and ATP export through VDAC (Figure 6.3). Under these more physiological conditions, the spatial organization of ANTs had a significant effect on ATP gain within the cytosol. While the spatiotemporal simulations did not exhibit significantly strong deviations from the spatially independent ODE system when ANTs were exclusively located at the IBM, the co-localization of ANTs with ATP synthases at the apex of cristae led to an approximately halved ATP export into the cytosol. Careful analysis of the dynamics revealed that this effect is driven by smaller concentration gradients between the ICS and the OM for ANT localization in the cristae, which led to ATP buffering within the cristae. This scenario is in contrast with the greater concentration gradient formed between the IBM and the OM when ANTs are located in the IBM what is facilitating ATP transport into the cytosol. These findings quantitatively support the importance of sub-organelle gradients suggested in the literature (Mannella, 2000).

To test whether this buffering mechanism might have an effect on synaptic physiology and explain the distinct morphology of brain and specifically of synaptic mitochondria, I subsequently simulated the mitochondrion in its synaptic environment with a variable cytosolic ATP consumption reflecting changes during synaptic transmission. These simulations have shown that ATP buffering in cristae caused by the non-equilibrium induced gradients is a mechanism to buffer large energy demand peaks.

I finally used my detailed model to calculate the ATP production rate of the considered mitochondrion for the different scenarios. The resulting rates of $\sim 10^5$ molecules of ATP per second are in agreement with my theoretical estimation based on the ANT translocation rate and the ANT density in mitochondria (See Appendix A, Section 8.7). These values are further supported by independent approximations found in the literature (Babu et al., 2017; Attwell and Laughlin, 2001) as summarized in Table 7.1 where minor deviations to the calculations by Attwell and Laughlin (2001) would rematch for firing rates of 30 Hz. The main mechanism how mitochondria decode the firing rate is probably Ca^{2+} influx through the mitochondrial calcium uniporter (MCU) (Kirichok et al., 2004). Incorporating the MCU and the effect of Ca^{2+} on the membrane potential in a future version of the model will allow for more detailed predictions of ATP

production rates in dependence on neuronal activity.

#ATPs/sec	Reference
$0.56 \cdot 10^5$	MCell simulations (ANTs in the CM)
$0.72 \cdot 10^5$	MCell simulations (ANTs in the IBM)
$0.95 \cdot 10^5$	ODE simulations
$4.60 \cdot 10^5$	theoretical estimation
$7.00 \cdot 10^5$	Attwell and Laughlin (2001)
$6.02 \cdot 10^5$	Babu et al. (2017)

Table 7.1: Estimation of ATP production in synaptic mitochondria.

Overall, my systematic approach with the detailed mitochondrial model has shown that the concrete morphology of the presynaptic mitochondrion induces anomalous diffusion but has not per se an impact on ATP production when the system relaxes towards an equilibrium steady state (Figure 6.2). In contrast, the spatial arrangement of ANTs under non-equilibrium conditions induce sub-organelle gradients that led to a significant effect on the cytosolic ATP concentration (Figure 6.3F). Physiological simulations of the synaptic dynamics suggest that this buffering effect might be a mechanism to smear out the variable energy demands (Figure 6.6) and may therefore increase robustness and adaptability of synapses and explain the distinct morphology of brain mitochondria.

Part II

Mitochondrial genes and its temporal organization

Chapter 8

Mitochondrial gene expression

In the following explorative approach, I investigated the mitochondrial dynamics on the more global scale by analyzing the regulation of mitochondrial gene expression during the circadian cycle. Hence, on this slower time scale of hours, the resulting adaptation is on the network structure level. In particular, the question of metabolic adaptation was addressed by investigating these structural changes in dependence on feeding conditions and their relation to cellular functionality.

8.1 Introduction

After years of evolution, mammals and other organisms have adapted their behavior and physiology to the light and dark cycles (Gerhart-Hines and Lazar, 2015). This temporal adaptation of behavioral and physiological processes might provide advantages to better adjust to the foreseen daily changes of the environment (Gerhart-Hines and Lazar, 2015). Through a molecular mechanism based on a transcription/translation feedback loop present in all cells of our body, the pace is maintained and e.g. in rodents up to 10% of genes exhibit daily rhythms in expression (Panda et al., 2002a).

The master circadian clock in mammals is the suprachiasmatic nucleus (SCN) of the hypothalamus. It regulates behavioral and physiological circadian activity and also orchestrates the activity of peripheral tissue. Projections of melanopsin retinal ganglion cells to the SCN translate light information and can photo-entrain the master clock (Panda et al., 2002b). Large fractions of the hypothalamic SCN and liver transcriptome exhibit daily rhythms in a tissue specific manner (Panda et al., 2002a). While the SCN is rather insensitive to perturbations of the feeding pattern, the rhythms in the liver are determined by the interplay of the cell-autonomous molecular clock and the feeding pattern (Vollmers et al., 2009). Moreover, a compromised circadian phenotype can be rescued by a time-restricted diet (Vollmers et al., 2009). Thus, metabolism is believed to be temporally coordinated to maintain metabolic homeostasis (Zarrinpar

et al., 2016), its disregulation is associated with a number of metabolic diseases (Zarrinpar et al., 2016).

To understand in more detail how the temporal organization of metabolism is fulfilled, I analyzed gene expression dynamics of liver cells in mice under ad libitum and time-restricted feeding conditions with a particular focus on mitochondria related genes. For this purpose, I filtered the transcriptome data sets for genes listed in MitoCarta – a repository of genes encoding for mitochondria localized proteins (Calvo et al., 2015). For functional analysis, I generated co-expression networks and genes with similar co-expression pattern were grouped by a hierarchical clustering algorithms. Finally, I studied the temporal organization of these genes and mapped it to their associated role using the functional annotations provided in MitoCarta.

8.2 Material and Methods

In the past, patterns of hepatic gene expression of mice under different feeding conditions were analyzed as described previously (see (Vollmers et al., 2009) for more details). In brief, animals were first entrained under light-dark conditions for 14 days, and subsequently released in darkness for 15 days. Sample collection started at day 16 and was taken every hour for 24 hours. The animals were either fed ad libitum (with permanent food availability) or during a restricted time of 8 hours during the light phase. Total RNA was pooled form at least three livers and transcript levels were quantified by qPCR (Vollmers et al., 2009). From the whole transcriptome, I selected those genes encoding for mitochondrial proteins (Calvo et al., 2015) $\sim$ 1000 transcripts.

For further investigation, I normalized the transcripts by first taking the logarithm of base 2 of the expression and afterwards median-normalizing to 1. To identify similar gene expression profiles, I computed gene-gene correlation matrices using Pearson's correlation coefficient. These correlations were subsequently used as a distance matrix to cluster genes with similar expression profile by a hierarchical clustering algorithm implemented in the Python library Scipy. Similar tools known in the literature as co-expression matrices (Zhang and Horvath, 2005; Horvath et al., 2006) have been used in the past to analyze system-level functionality of genes.

From the gene-gene correlation matrix, I generated weighted networks where nodes are represent by genes and weighted connections are described by correlations between genes. A variable correlation threshold was used to analyze the main connected component of the network. All network analysis was done using Networkx, a Python package to create, adapt and study complex networks.

The phases of gene expression were determined by the cosine-wave fitting algorithm COSOPT which also calculate parameters characterizing the goodness of the fit to a circadian pattern of expression (Panda et al., 2002a; Straume, 2004).

Several functional labels can be associated with mitochondrial proteins such as proteins associated to membrane transport, to structure, to the electron transport chain, to apoptosis, to the TCA cycle, to ROS metabolism, to fatty acids and ketone metabolism, to mobility, to iron metabolism, to CoQ synthesis, to ribosomes or to tRNA synthetase. An attempt to label theses $\sim$ 1000 genes was made using the annotations found in MitoCarta, together with a number of different literature sources (Pfanner et al., 2014; Zick et al., 2009; Nilsson et al., 2009; Lill et al., 2012; MacAskill and Kittler, 2010; Hoppins et al., 2011; Arroyo et al., 2016; Scarpulla, 2011; Johnson et al., 2007; Scheffler, 2009) and the PDmap.

8.3 Explorative results

To investigate whether mitochondrial metabolism exhibits a coordinated order in relation to circadian control, the normalized expression data for the different feeding conditions were first visualized. The resulting heatmaps of the temporal hepatic gene expression are displayed in Figure 8.1 for ad libitum feeding (A) and time-restricted feeding (B). The white and black bars at the bottom represent the time of the day and red bars indicate food availability. The order of the genes is different for each representation due to the independent hierarchical clustering using the gene-gene correlation matrix as distance measure.

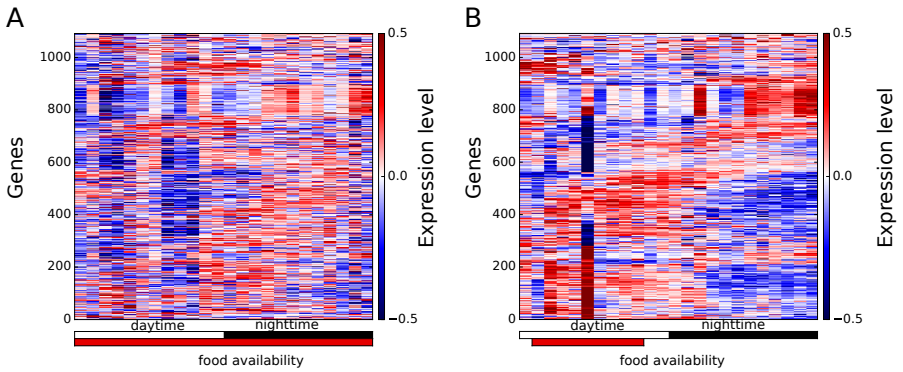

Figure 8.1: Dynamics of hepatic gene expression in mice under different feeding conditions. A) Ad libitum feeding (ad lib) and B) daytime-restricted feeding (trf). Expression is shown over time where white bars indicate daytime, black bars indicate nighttime and red bars indicate food availability. The order of the genes is different for each representation due to the independent hierarchical clustering.

By a first visual inspection, the temporal organization of the transcripts under time-restricted feeding conditions seems to exhibit a stronger co-regulation (Figure 8.1,B). To quantify this observation, thresholded gene-gene correlation matrices were plotted (Figure 8.2) with ordering accordingly to the indexes given by the hierarchical clustering (same order as Figure 8.1). Here, only the values of the co-expression matrices larger than 0.5 or smaller than -0.5 were plotted.

To continue with the analysis of the co-expression matrices, corresponding networks were generated with genes representing nodes and links connecting them if the corresponding correlation is higher than a threshold (Figure 8.3). There are several ways to characterize these networks. A very simple approach is to count the total number of connections present in the network. For instance, for a threshold of 0.8, the total number of connections is 10990 under time-restricted feeding and 7872 for ad

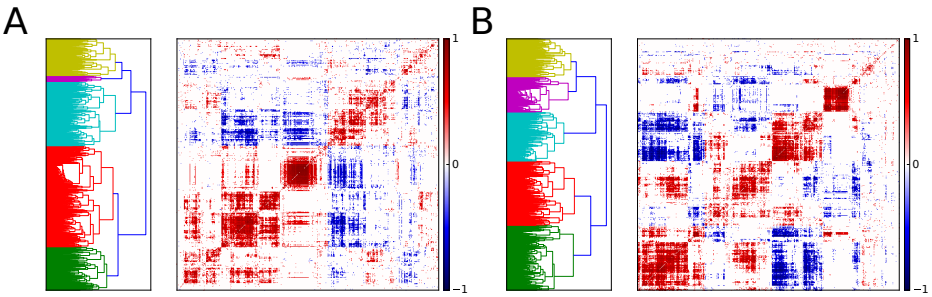

Figure 8.2: Thresholded gene-gene correlation matrices for animals under different feeding conditions. A) for ad libitum feeding (ad lib) and B) daytime-restricted feeding. As before the order is different for each network due to the independent hierarchical clustering of the corresponding matrices.

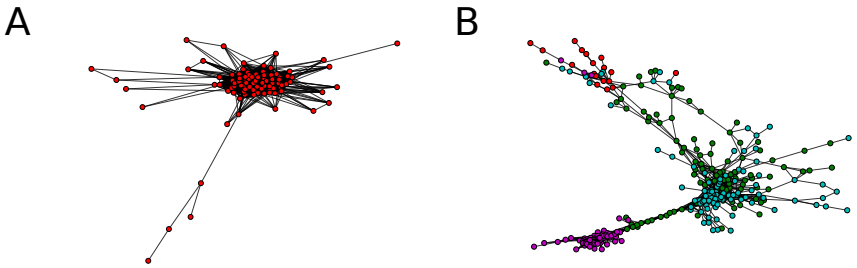

Figure 8.3: Network representation for the thresholded (higher than 0.9) co-expression matrices for ad libitum feeding (A) and for day-time restricted feeding (B).

libitum feeding ($\sim$ 30% less connections). Another approach is to quantify the size of the main connected component. In particular, I analyzed the size (number of nodes) of this network for different values of the threshold (Figure 8.4). As the threshold is increased the network starts to fall apart, groups of nodes get disconnected because links are removed. The main connected component is the larger cluster of nodes that remain linked. Since these are co-expression matrices the size of this main component speaks about the global organization of the expression. Under time-restricted feeding conditions, mitochondrial genes show consistently stronger temporal organization.

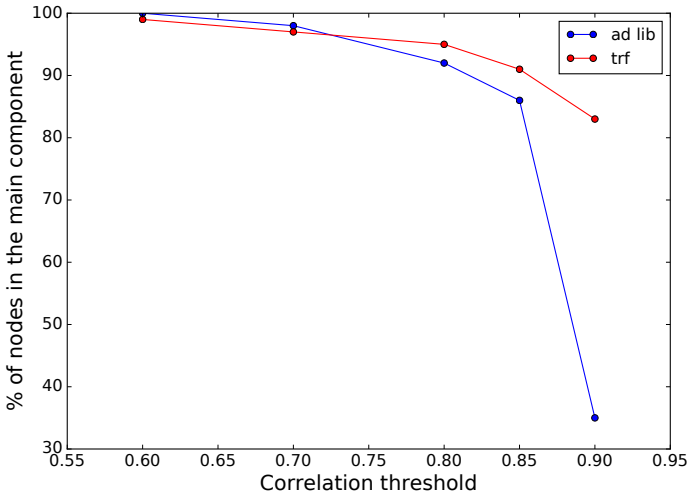

Figure 8.4: Relative number of nodes in the main component as a function of the correlation threshold for ad libitum feeding conditions (in blue) and for time-restricted feeding conditions (in red).

To investigate the crosstalk between circadian regulation and metabolic activity, the expression was classified with respect to its specific dynamics. From Figure 8.2B it becomes apparent that five gene clusters obey a similar expression dynamics. For these groups of genes, I analyzed the phase distribution for the different feeding conditions. This analysis exhibited that food can have a significant impact on the phase of some genes (Figure 8.5) and shift the phase of several transcripts (Figure 8.5, upper panels) while others were unaltered (Figure 8.5, lower panels).

A naturally following question was then to analyze the functional annotations of genes in each of these groups. In Figure 8.6 the different resulting functional groups are shown in rows and columns give the percentage of labeled genes in each dynamical group (obtained from the clustering). For instance, by looking at the first row, the red and green cluster together consists of 60% of the membrane transport proteins which were identified to be the most sensitive to food conditions. In the third row, the red

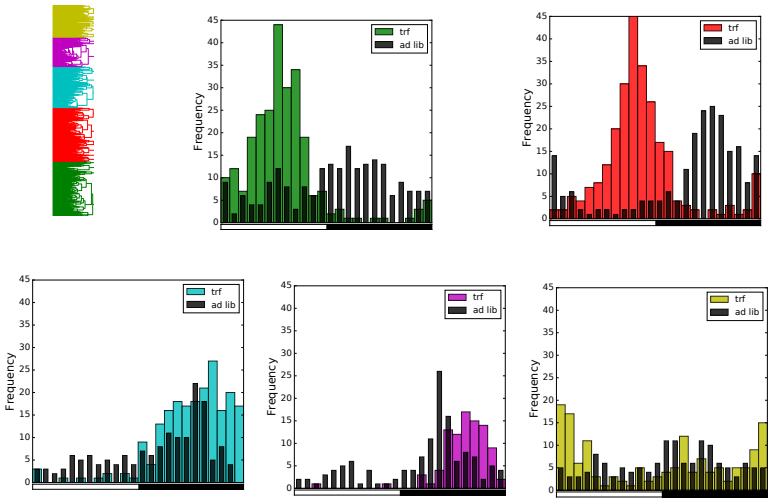

Figure 8.5: Phase distribution of genes separated accordingly to the clusters obtained in Figure 8.2B for both feeding conditions.

and green cluster have 80 % of genes in the ribosomal group.

8.4 Discussion and Conclusions

In this explorative analysis, I found distinct temporal patterns of expression for many genes under different feeding patterns. Mitochondrial genes exhibited the tendency of stronger coregulation under time-restricted feeding condition what is accompanied with a more robust global organization.

Furthermore, the explorative analysis indicates some functional relation in dependence to the temporal organization. Transcripts which were more responsive to feeding conditions seem to be related to membrane transport (60%), encoding for mitochondrial ribosomes (80%), related to mitochondrial structure and apoptosis (40%) or encoding for components of the ETC (50%).

In the future the robustness of these results will be tested against different distance measures and clustering algorithms.

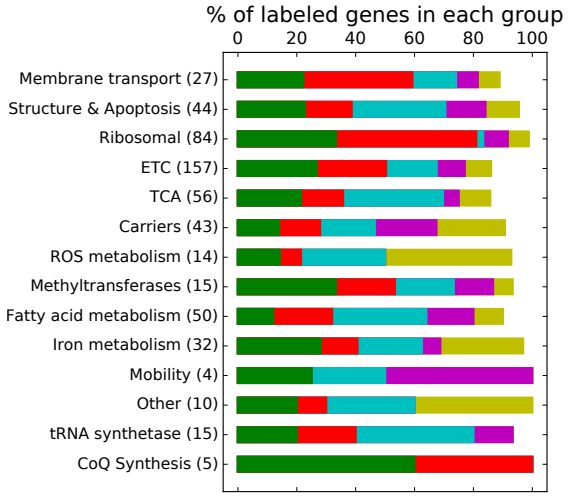

Figure 8.6: Functional annotations of genes organized in the five dynamical clusters obtained in Figure 8.2B.

General conclusions

General conclusions

Energy is ubiquitously required to maintain life. Cells extract energy from their environment and make it available for physiologically relevant processes in form of ATP by glycolysis and oxidative phosphorylation. As such, mitochondria play an essential role in metabolism and cell signaling in health and disease.

A compelling open question from the spatial systems biology perspective is how mitochondria related structures affect the function on different scales. On the slower time scale, the adaptation of protein content may influence the energetic machinery by changing the overall molecular interactions. On the faster time scale, the formed subcompartments are speculated to provide an advantage for ATP production but a mechanistic and quantitative framework is still lacking.

The complexity of the underlying regulatory processes leads to the need for mathematical analysis and modeling to obtain mechanistic insights. In general, mathematical models can serve as tools to test suspected mechanisms that might control cellular behavior. Moreover, mathematical models can fill gaps that current experimental technologies cannot investigate. These approaches are the essence of this work. Electron tomography can resolve the internal structure of mitochondria at high resolution and proteins can be tagged and localized with high precision (Shu et al., 2011; Perkins, 2014), but it only generates static images that cannot give dynamic information. To fill this gap, I built an *in silico* representation of a mitochondrion using three-dimensional morphologies from electron tomography combined with molecular dynamic models of the main ATP producing components and integrated these in the agent-based reaction diffussion simulator MCell. With this mechanistic approach, I found that under physiological conditions, the spatial organization of ANTs has a significant effect on ATP availability within the cytosol. Careful analysis of the dynamics revealed that this effect is mainly driven by small concentration gradients within the mitochondrion, which led to ATP buffering in the cristae structure and may contribute to cellular robustness. The details of these findings are found in Chapter 7.

The effect of the mitochondrial membrane potential has been neglected in this first version of the model. This simplification is not due to the disregard of its importance but based on general technical challenges of electro-diffusion which are just now addressed in the research field. To properly include the effect of electro-diffusion, the

Nernst-Planck equation has to be solved in the specified geometry. This would bring us to solve partial differential equations in the complex mitochondrial morphology with finite methods – a rather challenging scenario. Furthermore, this approach would imply the assumption of continuous concentrations of molecules in the finite geometry which is a very doubtful scenario due to low number of molecules. These issues point to the general challenges in the field of spatial systems biology on the subcellular level where in future such issues should be tackled for instance by hybrid models. But currently there is not yet an established theoretical foundation for these approaches available. As an intermediate step, ignoring the spatial resolution of mitochondria to calculate the membrane potential by employing an ODE formalism could give at least a first estimation for the movement of ions across the mitochondrial membrane.

Two major players of mitochondrial dynamics were left out in this version of model: the electron transport chain (ETC) and the mitochondrial calcium uniporter (MCU). In principle, the elements of the ETC could be included following the modeling approach of Magnus and Keizer (1997), and the dynamic of the MCU could be also captured as described in Section 4.5. However, without explicit consideration of the membrane potential these processes cannot be coupled meaningfully and mechanistically to the dynamics. Furthermore, the available model of the MCU does not capture the much faster ion channel mechanism of the recently characterized dynamics (Kirichok et al., 2004) and may therefore introduce artifacts. Therefore, a next step is to develop an appropriate MCU model and to include this together with an ODE based estimation of the mitochondrial membrane potential in a next version of the model.

In the second part of this dissertation, I explored changes of the underlying regulatory network of mitochondrial protein content on the slower time scale of hours. This data-driven approach revealed distinct temporal patterns of mitochondrial gene expression under different feeding conditions. The analysis indicated a link between these structural network modifications and physiological functionality in dependence of the temporal regulation of subgroup of genes. Interestingly, a more robust organization was found when animals were fed in a time-restricted manner. Further validation and testing of the robustneess of these preliminary results are required. In particular, the reproducibility of the results with other distance measures besides Pearson's correlation. In addition the effect of genetic interactions (epistasis) within and between these groups should be investigated, also in context of not mitochondrial related genes.

For a more complete understanding of mitochondrial dynamics, the embedding of these investigations into further integrative multiscale perspectives would be compelling to understand organism regulation. In particular, next steps should study if the temporal patterns are conserved for mitochondria in different tissues or if these patterns are tissue specific? Time restricted feeding has been shown to have a significant impact on health (Zarrinpar et al., 2016) but the underlying mechanisms are not well characterized. Answering the above questions could significantly contribute to

the identification of principles in metabolism on temporally at locally organized scales. This will be of further relevant since in recent years significant evidence has shown the importance of circadian rhythms for health (Panda, 2019).

Multiscale models are needed to integrate experimental results at different temporal and spatial scales and to dissect the mechanisms that control system behavior. Such models can produce *in silico* scenarios to test different hypothesized mechanisms, but most importantly they should fill the gap current experimental technology leaves, by zooming in and out of the dynamics, changing scales, coarse-graining the dynamics and giving distinct views of a dynamical phenomena. In the modeling field, no such an approach is currently available. We can model different scales with different computational strategies but there is no tool that combines these scales based on general principles and would allow us to have different representations in the same *in silico* experiment. Efforts are directed to this goal from the theoretical and computational perspective to bridge –for instance– molecular dynamics simulations to Markov state models. The development of these simulation tools and theory would allow us to merge the two parts of this dissertation by including the slower scale of a variable protein content into intra-mitochondrial dynamics. Therefore, the here investigated scales and developed tools will further trigger new scientific approaches towards this active research direction.

Appendix A

8.5 Additional figures for part I

Here, we include all variables of the model that are not shown in the main section, for both averaged traces of MCell simulations and the corresponding solution of the system of ODE. Figure 8.7 A-H exhibits all the variables of the ANT model for the isolated scenarion of equilibration and panels I-N show all the variables of the ATP synthase model.

Analogously, Figure 8.8 exhibits the variables for the non-equilibrium condition induced by a clamped ADP concentration at the surface of the OM where Figs. 8.8 A-H shows variables for the ANT model and panels I-N of the ATP synthase model.

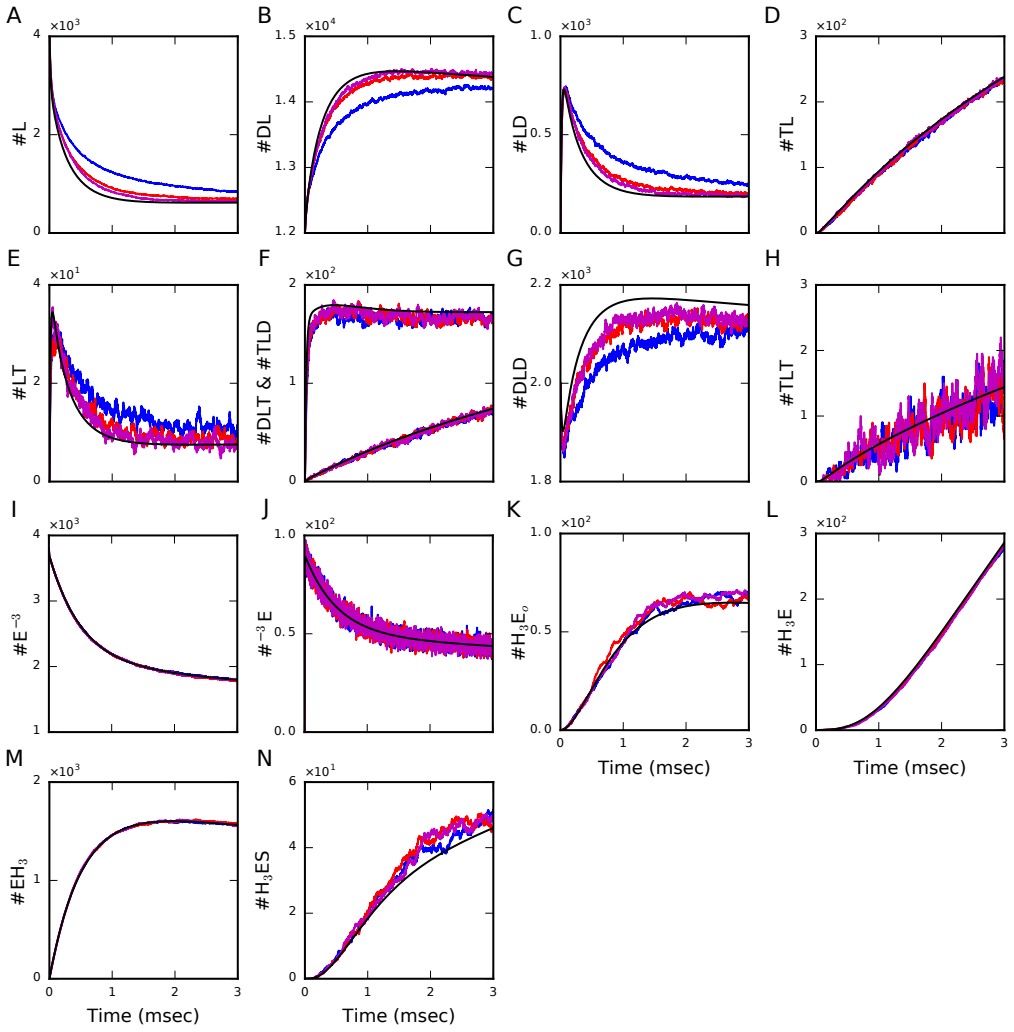

Figure 8.7: Isolated scenario of dynamic equilibration does not exhibit a strong dependence on the spatial arrangement. Comparison of molecule numbers between averaged trajectories of 10 different initial conditions in MCell and the results obtained with the ODE system. Simulations started with a a large number of ADP molecules outside (IMS and ICS) that were subsequently phosphorylated. ATP molecules accumulate outside due to the lack of VDACs. ANT molecules were placed in three different locations: ANTs homogeneously distributed in the IBM (in red), ANTs colocalized with ATP synthase at the most curved region of the CM (blue) and ANTs in both locations (magenta). The results of the ODE system is shown in black. Panel A-H show the variables of the ANT model and panels I-N the variables of the ATP synthase model. The different arrangements of ANTs do not exhibit significant differences with the corresponding ODE system.

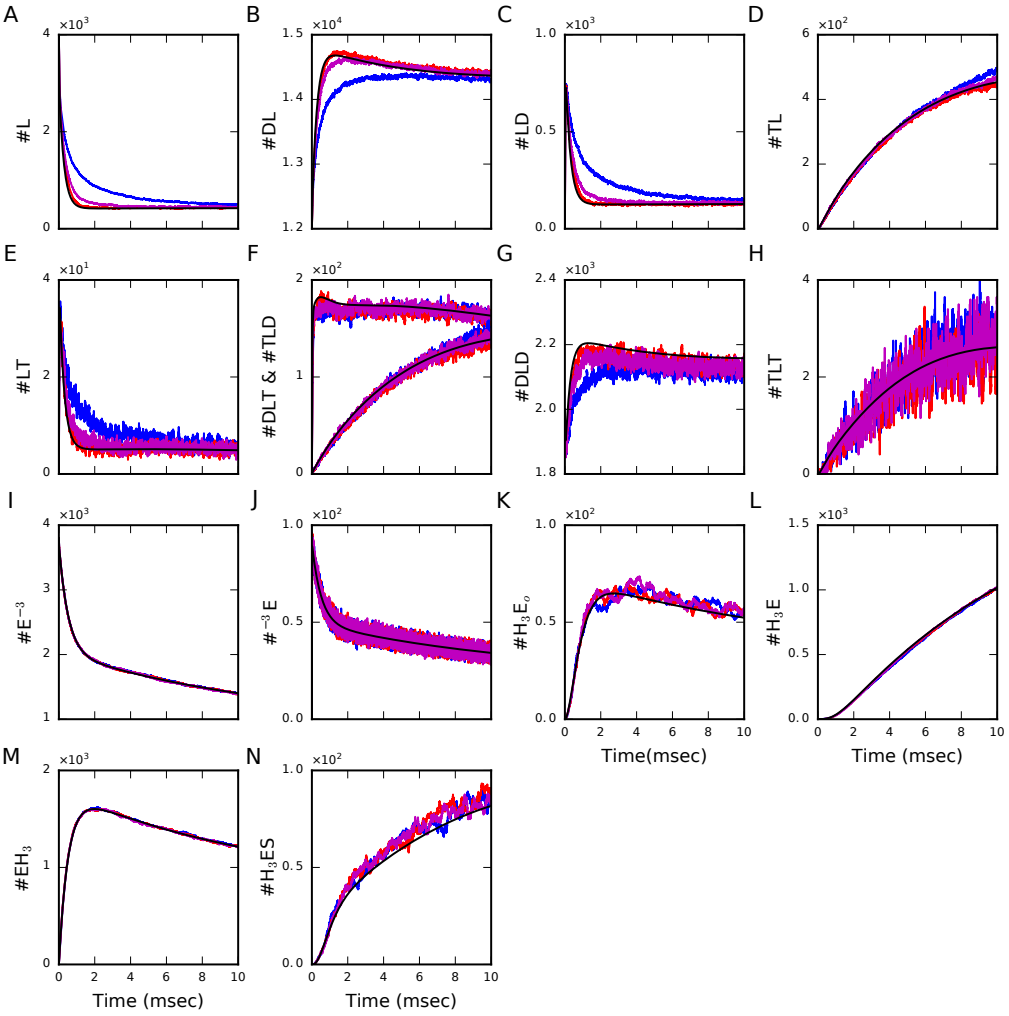

Figure 8.8: Non-equilibrium dynamics of the synaptic mitochondrion driven by clamped ADP concentration and ATP export. Averaged molecule number trajectories for the distinct ANT localizations with ANTs homogeneously distributed in the IBM (red), colocalized with ATP synthase at the most curved region of the CM (blue) or in both locations (magenta) were compared with results of the ODE system. This comparison exhibits most significant spatial effects for colocalization (blue). In panel A-H, we show variables of the ANT model, and in panels I-N variables of the ATP synthase model.

8.6 Experimental data-Reproducing results

Metelkin et al. (2006) developed a model of the ANT based on the data from Kraemer and Klingenberg (1982). In this publication exchange of adenine nucleotides were measured on reconstituted carriers from heart mitochondria on liposomes. The data need to be modified to get turnover rate vs concentration, Figures 8.9,8.10,8.11A (in the original paper flux vs rate/concentration is plotted), and the units need also to be modified. A number of typos were suspected in Metelkin et al. (2006); therefore, a script was written to extract the experiemental data points systematically from Kraemer and Klingenberg (1982), Figure 8.9,8.10,8.11B. Afterwards, the data is plotted as turnover rate vs concentration, doing the inverse of the x coordinate and mutliplying by the rate, the y coordinate is modified by multiplying by 0.06 (dividing by 2 times the molecular weight of the ANT). After these modifications, the turnover rate vs concentration is obtained in units of min^{-1}, Figure 8.9,8.10,8.11C. A typo was found in the respective figures in Metelkin et al. (2006), reproduced here Figure 8.9,8.10,8.11D, the units of the turnover rate were written as sec^{-1} but are min^{-1}. Another typo was found in Figure 8.10C, line 1, corresponds to a membrane potential of 0 mV, and is labelled as 180 mV in Metelkin et al. (2006). Similarly with line 2, it corresponds to a membrane potential of 180 mV, but is labelled as 0 mV in Metelkin et al. (2006).

The next step was to reproduce the results using the model and parameter values from Metelkin et al. (2006)

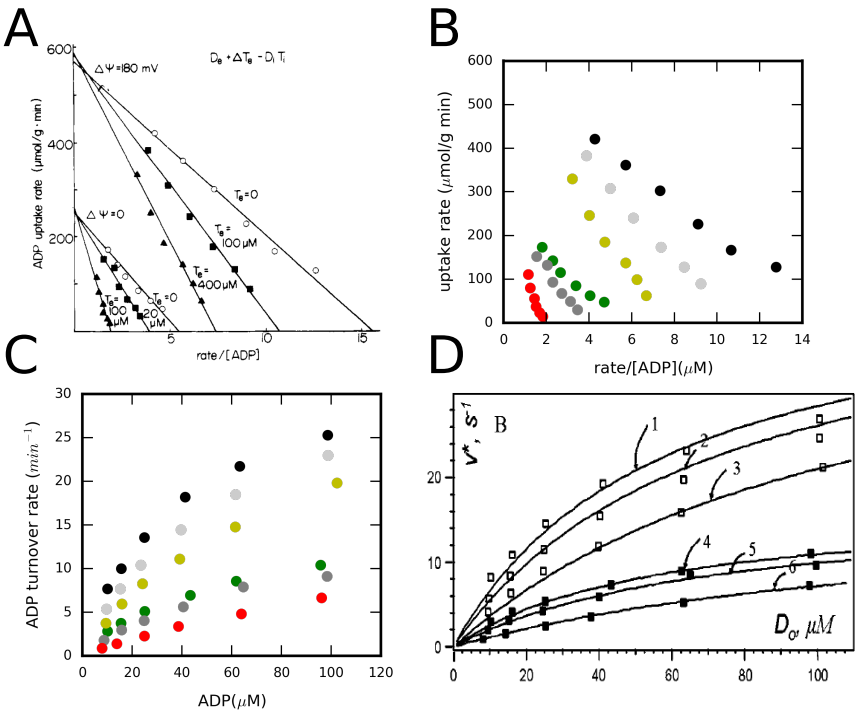

Figure 8.9: Experimental data. A) ADP uptake rate vs rate/[ADP], figure taken from Kraemer and Klingenberg (1982) (Figure1). ADP uptake rate was measured for different concentrations of ATP outside (T_o) and different values of the membrane potential $\Delta\psi$ = 180, 0 mV. B) Extracted data point from A), black, light grey and yellow points, ADP uptake rate for a membrane potential of $\Delta\psi$ 180 mV, and ATP concentrations outside the liposomes of 0, 100, 400 μM respectivelly. Green, grey and red points ADP uptake rate for membrane potential of $\Delta\psi$ 0 mV, and concentrations of T_o of 0, 20, 100 μM respectivelly. For a concentration of ADP and ATP inside the liposomes of 5 mM. C) The data is transformed to obtain turnover rate vs concentration, and the units modified, dividing by 2 times the molecular weight, the obtained turnover rate is in units of min^{-1}. D) Reproduction of Figure 5b from Metelkin et al. (2006). A typo was found in the units of the turnover rate in Metelkin et al. (2006).

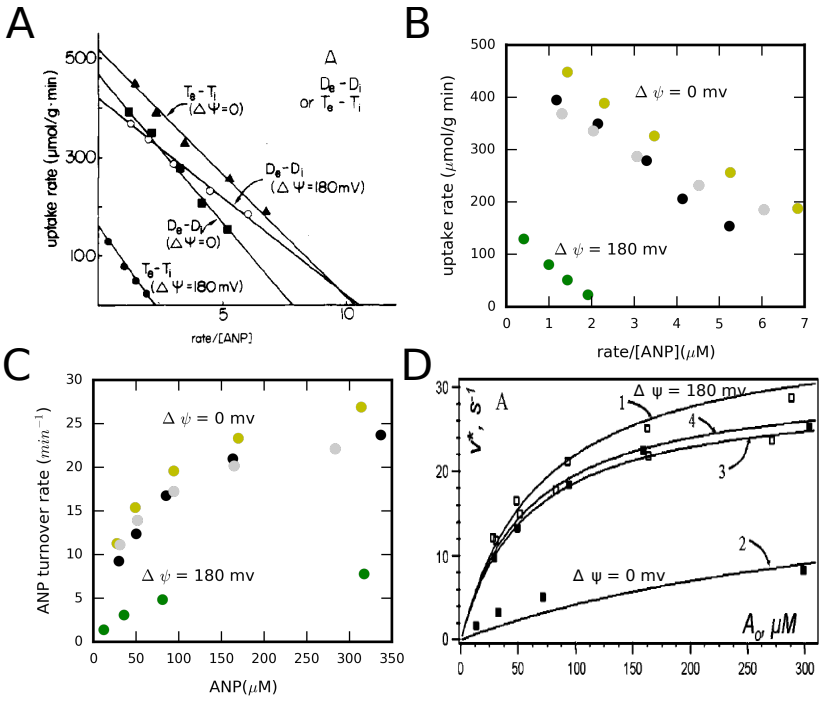

Figure 8.10: Experimental data. A) Adenine nucleotide (ANP) uptake rate vs rate/[ANP], figure taken from Kraemer and Klingenberg (1982) (Figure 2A). ADP uptake was measured for membrane potentials of $\Delta\psi = 180$ and 0 mV, and for no ATP inside and outside the liposomes. ATP uptake rate was also measured for the same membrane potential, with no ADP present. B) Extracted data points from A), yellow and green points, ATP uptake rate vs rate/[ATP] for a membrane potential of $\Delta\psi$ 0 and 180 mV, and no ADP concentration. Black and grey points, ADP uptake rate vs rate/[ADP], for a membrane potential of $\Delta\psi$ 0 and 180 mV, and no ATP concentration. C) The data is transformed to obtain turnover rate vs concentration, and the units modified, dividing by 2 times the molecular weight, the obtained turnover rate is in units of min^{-1}. D) Reproduction of Figure 5a from Metelkin et al. (2006). Two typos were found here, one is, as before, the units of the turnover rate that are in min^{-1} not sec^{-1}, and the other is related with the values of the membrane potential. Line 1, corresponds to a membrane potential of 0 mV, and is labelled as 180 mV in Metelkin et al. (2006). Similarly with line 2, it corresponds to a membrane potential of 180 mV, but is labelled as 0 mV in Metelkin et al. (2006).

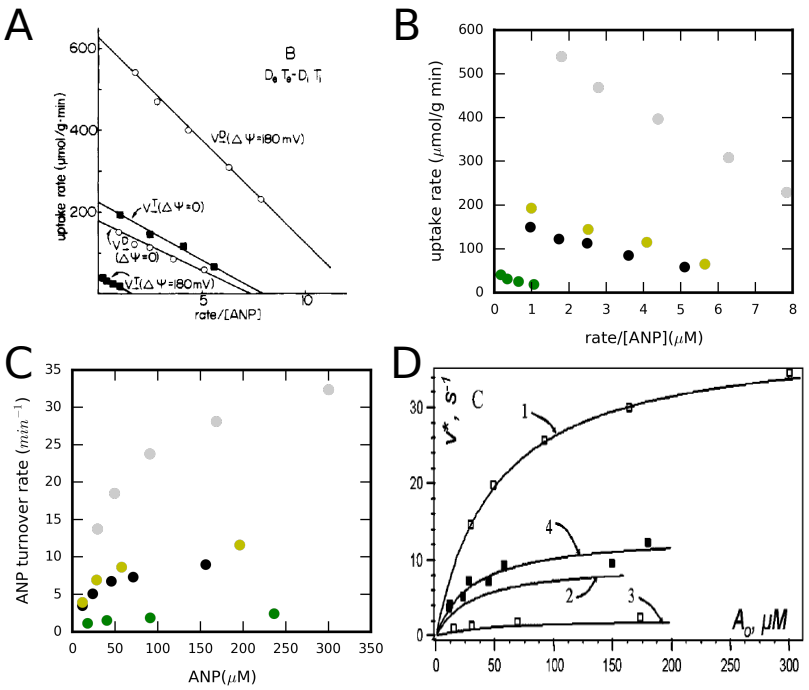

Figure 8.11: Experimental results. A) Adenine nucleotide (ANP) uptake rate vs rate/[ANP], figure taken from Kraemer and Klingenberg (1982) (Figure 2B). ADP uptake rate was measured for membrane potentials of $\Delta\psi = 180$ and 0 mV, and for a concentrations of ATP outside equal to the ADP concentration, and ADP and ATP concentrations inside the liposomes of 5 mM. ATP uptake rate was also measured for the same conditions. B) Extracted data points from A), yellow and green points, ATP uptake rate vs rate/[ATP] for a membrane potential of $\Delta\psi$ 0 and 180 mV respectivelly, and ADP concentration equal to the ATP concentration. Black and grey points, ADP uptake rate vs rate/[ADP], for a membrane potential of $\Delta\psi$ 0 and 180 mV, and ATP concentration equal to the ADP concentration. C) The data is transformed to obtain turnover rate vs concentration, and the units modified, dividing by 2 times the molecular weight, the obtained turnover rate is in units of min^{-1}. D) Reproduction of Figure 5c from Metelkin et al. (2006).

8.7 Estimation ATP production in synapses

Based on the turnover rate of ANTs and the number of translocators in the synaptic mitochondrion, we estimated the number of ATP molecules that can be exported to the cytosol per second (Table 8.1). The product of the turnover rate times the number of ANTs gives the maximum number of ATP molecules that can reach the cytosol per second if the ANTs are not the limiting step. The total amount of ANT proteins in synaptic mitochondria has been estimated to 1.37 nmol/mg protein (Chinopoulos et al., 2009) assuming 1 nmol/mg protein $\approx$ 1.25 mM (Magnus and Keizer, 1997) leading to a concentration of 1.71 mM. The inner membrane has a volume of 0.021 μm^3 what corresponds to $\sim 2{\cdot}10^4$ ANTs within the mitochondrion. This number of ANTs working at a turnover rate of 23 s^{-1} exports $4.6{\cdot}10^5$ ATPs/s. We further estimated the number of ATP produced by non-synaptic brain mitochondria (Table 8.1). This value critically depends on the volume of the mitochondria and, since no complete reconstructions are available in the literature, this is only a rough estimation based on an assumed cylindrical shaped mitochondria with a radius of 0.3 µm and length 1 µm (Perkins et al., 2001).

Tissue	**Rate**(s^{-1})	**Density**(nmol/mg prot)	**Concentration** (mM)	**Volume** (μm^3)	**Nr.ANTs**	**ATPs/sec**	**ATP moles/sec**
Synapse	23 *	1.37*	1.71 ‡	0.021 †	$2 \cdot 10^4$	$4.6 \cdot 10^5$	$0.75 \cdot 10^{-18}$
Non-synapse	22 *	1.44 *	1.79 ‡	0.28	$3 \cdot 10^5$	$6.6 \cdot 10^6$	$1.1 \cdot 10^{-17}$

Table 8.1: Estimation ATP production in brain tissue.

* Chinopoulos et al. (2009), ‡ 1 nmol/mg prot $\approx$ 1.25 mM (Magnus and Keizer, 1997), † our estimation.

The number of ATP molecules produced by a synaptic mitochondrion coincides with the estimations of Attwell and Laughlin (Attwell and Laughlin, 2001) explained above. Moreover, a similar value of $6.02 \cdot 10^5$ ATP molecules per second has been also estimated for hair cell mitochondria (Babu et al., 2017). In Table 7.1 we compare the different estimations with the results of our MCell and ODE simulations.

8.8 Time scales estimation

We calculate the spatial time scales for a diffusion coefficient of D $= 1.5 \cdot 10^{-7}\mathrm{cm}^2\mathrm{s}^{-1}$ by considering the characteristic length scales as the diameter of cristae junctions $\sim$ 25.5 nm [1] (L_1) and the distance from the center of the mitochondrion to the IBM $\sim$ 0.13 µm (L_2). The time required to transverse these distances is τ and is calculated as $\tau = \mathrm{L}^2/6\mathrm{D}$.

$$\tau_1 = \frac{L_1^2}{6D} \sim 7 \cdot 10^{-6} s$$
$$\tau_2 = \frac{L_2^2}{6D} \sim 2 \cdot 10^{-4} s$$

A number of reactions occur in the ANT model. We calculated the corresponding time scales of some of the reactions to compare with the temporal scales of diffusion. The time scales of the forward reactions are denoted by τ_f and for the backward reactions by τ_b accordingly to a previous report (Andrews and Arkin, 2006). For these calculations, we used the initial concentrations. As before L represents the free protein, $\mathrm{D_i}$ denotes ADP molecules from the matrix side and $\mathrm{D_o}$ ADP from the inner boundary membrane and cristae side, called outside.

$$D_i + L \rightleftharpoons LD \quad \tau_f \sim 2.4 \cdot 10^{-4} s,\ \tau_b \sim 2.5 \cdot 10^{-5} s$$
$$D_o + L \rightleftharpoons DL \quad \tau_f \sim 4 \cdot 10^{-4} s,\ \tau_b \sim 1 \cdot 10^{-2} s$$
$$T_i + L \rightleftharpoons LT \quad \tau_f \sim 1.6 \cdot 10^{-3} s,\ \tau_b \sim 2.5 \cdot 10^{-5} s$$
$$T_o + L \rightleftharpoons TL \quad \tau_f \sim 27 s,\ \tau_b \sim 5 \cdot 10^{-3} s$$

A similar analyzes has been done for the reactions of the ATP synthase model.

$$E_o \rightleftharpoons EH_3 \ \ \tau_f \sim 1 \cdot 10^{-3} s,\ \tau_b \sim 1 \cdot 10^{-3} s$$
$$D_i + H3E_O \rightleftharpoons H3ES \ \ \tau_f \sim 3.1 \cdot 10^{-1} s,\ \tau_b \sim 1 \cdot 10^{-2} s$$
$$H3ES \rightleftharpoons T_i + H3E \ \ \tau_f \sim 2 \cdot 10^{-4} s,\ \tau_b \sim 1.8 \cdot 10^{-2} s$$

Different time scales are found for the reactions of the ANT and ATP synthase models that spread over a large range but most of them are between $1 \cdot 10^{-5}$ s and $1 \cdot 10^{-2}$ s (Figure 8.12). We graphically represent the time scales of the reactions (blue dots) and the temporal scales of diffusion (black lines). They overlap for both

[1] The diameter of the cristae junctions is an average over 25 junctions measured in the reconstructed mesh.

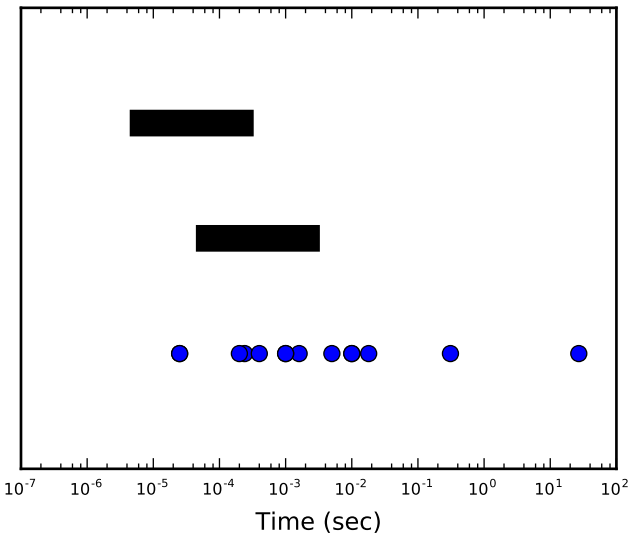

Figure 8.12: Graphical representation of the temporal scales. The black lines represent the temporal scales of diffusion, upper line for a diffusion coefficient of $1.5{\cdot}10^{-7}\mathrm{cm}^2/\mathrm{s}$, and the lower line for a diffusion coefficient of $1.5{\cdot}10^{-8}\mathrm{cm}^2/\mathrm{s}$. The blue dots are a representation of the temporal scales of the reactions. Decreasing the diffusion coefficient brings the temporal scales closer.

considered diffusion coefficients but for the smaller diffusion coefficient the scales get closer together and diffusion limitation becomes more predominant.

Appendix B

8.9 Details of MCell simulations

The MCell model is composed of 9 MDL modules: A main file with the global simulation specifications (Scene.main.mdl), the geometry file where the geometry is defined (Scene.geometry.mdl), a file where molecules are introduced (Scene.molecules.mdl), a file where the reactions are set (Scene.reactions.mdl), a file with all the parameter values used (Scene.parameters.mdl), the output file (`Scene.rxn_output.mdl`), the surface classes file (`Scene.surface_classes.mdl`) and the modify surface region file (`Scene.mod_surf_regions.mdl`). A useful reference guideline –giving details of each module– can be found here MCell Quick Reference Guide.

Main file

Below is included a part of the main file, where the global simulation parameters are specified, i.e. the total number of iterations, the time step (in seconds), if checkpointing the simulation this is also specified in this file (in this example the simulations will stop after 5 days running), the spatial partitioning is included, all the others MDL files that need to be read are called here (e.g. Scene.parameters.mdl, Scene.molecules.mdl, Scene.reactions.mdl, etc), afterwards the objects that are part of the simulations are determined. Finally the initial location of the molecules is specified, in this example `rel_d_mo` number of D molecules are released inside the object `inner_with_cristae_final`.

```
ITERATIONS = 1e8
TIME_STEP = 1e-9
VACANCY_SEARCH_DISTANCE = 10

CHECKPOINT_OUTFILE = "chkpt_10_1"
CHECKPOINT_REALTIME = 5:0:0:0

INCLUDE_FILE = "Scene.initialization.mdl"
```

```
PARTITION_X = [[-0.400000005960464 TO 0.400000005960464 STEP 0.00999999977648258]]
PARTITION_Y = [[-0.349999994039536 TO 0.349999994039536 STEP 0.00999999977648258]]
PARTITION_Z = [[-0.400000005960464 TO 0.400000005960464 STEP 0.00999999977648258]]

INCLUDE_FILE = "Scene.parameters.mdl"

INCLUDE_FILE = "Scene.molecules.mdl"

INCLUDE_FILE = "Scene.surface_classes.mdl"

INCLUDE_FILE = "Scene.reactions.mdl"

INCLUDE_FILE = "Scene.geometry_syn_resc.mdl"

INCLUDE_FILE = "Scene.mod_surf_regions.mdl"


INSTANTIATE Scene OBJECT
{
  inner_with_cristae_final OBJECT inner_with_cristae_final {}
  outer_membrane_final OBJECT outer_membrane_final {}
  syn OBJECT syn {}

  rel_d_m RELEASE_SITE
  {
   SHAPE = Scene.inner_with_cristae_final[ALL]
   MOLECULE = D
   NUMBER_TO_RELEASE = rel_d_mo
   RELEASE_PROBABILITY = 1

   ...
}
```

Geometry

In the geometry module all the objects and regions included in the simulations are defined, as a set of vertices, edges and surfaces.

```
 inner_with_cristae_final POLYGON_LIST
{
  VERTEX_LIST
  {
```

```
    [ -0.000546309340279549, -0.107638701796532, -0.378262519836426 ]
    [ -0.00388858979567885, -0.11393629014492, -0.380676567554474 ]
    [ -0.00802061147987843, -0.108226649463177, -0.38147896528244 ]
    [ -0.00697485264390707, -0.099134773015976, -0.377753883600235 ]
    [ 0.00244327099062502, -0.102245070040226, -0.370583981275558 ]
    [ -0.00312606617808342, -0.120454244315624, -0.37895792722702 ]
    [ -0.012694513425231, -0.118293903768063, -0.383267849683762 ]
    [ -0.00239189038984478, -0.0949208214879036, -0.369176000356674 ]
    [ -0.0165454987436533, -0.105396278202534, -0.379870444536209 ]
    ...

   DEFINE_SURFACE_REGIONS
  {
    curva
    {
      ELEMENT_LIST = [1735, 1944, 8212, 8777, 9140, 29757, 29783,
      29807, 29809, 29810, 29833, 29834, 29835, 29853, 29854,
      29855, 29856, 29873, 29874, 29875, 29876, 29877, ...]
     }
   }
```

Molecules

In the file Scene.molecules.mdl all the particles in my model are set. In this extraction of my model, ATP (T), ADP (D) and $E^{-3}(E_o)$ molecules are specified, and the diffusion coefficient set (in units of $cm^2 s^{-1}$).

```
DEFINE_MOLECULES
{
  T
  {
    DIFFUSION_CONSTANT_3D = 1.5e-7
  }
  D
  {
    DIFFUSION_CONSTANT_3D = 1.5e-7
  }
  Eo
  {
    DIFFUSION_CONSTANT_2D = 0
  }
 ...
```

```
}
```

Reactions

All the reactions taking part in the model are set in its own module (an extraction is shown below). As before, L represents the free ANT protein, TL, LT, DLT, etc. are bimolecular or trimolecular states of the protein. On brackets the rate of the reaction is specified (in units of $M^{-1}s^{-1}$ and s^{-1} for bimolecular and unimolecular reactions respectively).

```
 DEFINE_REACTIONS
{
  L' + T, <-> LT' [>k2_on, <k2_off]
  LT' + D' <-> DLT' [>k1_on, <k1_off]
  L' + T' <-> TL' [>k5_on, <k5_off]
  TL' + D, <-> TLD' [>k6_on, <k6_off]
  TLD' -> DLT' [kcp] : counter_prod
  ...
}
```

Parameters

In the optional file Scene.parameters.mdl all the values of the variables set can be specified.

```
/* DEFINE PARAMETERS */
a12 = 24    /*    units=s-1 */
a43 = 8e5    /*    units=M-1s-1 */
a56 = 1e3    /*    units=s-1 */
a45 = 1e2    /*    units=s-1 */
a54 = 1e2    /*    units=s-1 */
a21 = 40    /*    units=s-1 */
a65 = 924    /*    units=s-1 */
a34 = 1e2    /*    units=s-1 */
a32 = 5e3    /*    units=s-1 */
a23 = 4e6    /*    units=M-1s-1 */
a16 = 452457    /*    units=s-1 */
a61 = 11006    /*    units=s-1 */
a25 = 1.17e-12    /*    units=s-1 */
a52 = 2.0    /*    units=s-1 */
rel_eo_mo = 7100    /*    units=number_of_proteins */
...
```

Output

In the file `Scene.rxn_output.mdl`, the output from the simulations is established, in this example -in the seventh line- the number of ATP molecules inside the object `inner_with_cristae_final` is tracked. The number of reaction happening can also be tracked, the number of time a species hits a surface can also be tracked, etc.

```
INCLUDE_FILE = "./my_seed.mdl"
sprintf(param1,"%05g",my_se)

REACTION_DATA_OUTPUT
{
  STEP=1e-7
  {COUNT[T,Scene.inner_with_cristae_final]}=> "./react_data/param1_" & param1 & "/T.inner_with_cristae_final.dat"
  {COUNT[T,Scene.outer_membrane_final]}=> "./react_data/param1_" & param1 & "/T.outer_membrane_final.dat"
  {COUNT[D,Scene.inner_with_cristae_final]}=> "./react_data/param1_" & param1 & "/D.inner_with_cristae_final.dat"
  {COUNT[D,Scene.outer_membrane_final]}=> "./react_data/param1_" & param1 & "/D.outer_membrane_final.dat"
```

Surface classes

In the file `Scene.surface_classes.mdl`, properties of a surface can be defined transparent, absorptive, reflective or a concentration can be clamped. In this example, I campled the concentration of ADP molecules to 0.9 mM.

```
DEFINE_SURFACE_CLASSES
{
  Surface_Clamp
  {
    CLAMP_CONCENTRATION D, = 0.9e-3
  }
}
```

Modified surface regions

If a surface class has been generated, this property can be assing to an object in the file `Scene.mod_surf_regions.mdl`. In my simulations, the concentration of ADP molecules was clamped to the outer membrane.

```
MODIFY_SURFACE_REGIONS
{
  outer_membrane_final[ALL]
  {
    SURFACE_CLASS = Surface_Clamp
```

```
    }
  }
```

Bibliography

Alberts, B., Roberts, K., Lewis, J., Bray, D., Hopkin, K., Johnson, A. D., Walter, P., and Raff, M. (2015). *Essential cell biology*. Garland Science.

Andrews, S. S. and Arkin, A. P. (2006). Simulating cell biology. *Current Biology*, 16(14):R523–R527.

Arroyo, J. D., Jourdain, A. A., Calvo, S. E., Ballarano, C. A., Doench, J. G., Root, D. E., and Mootha, V. K. (2016). A genome-wide crispr death screen identifies genes essential for oxidative phosphorylation. *Cell metabolism*, 24(6):875–885.

Attwell, D. and Laughlin, S. B. (2001). An energy budget for signaling in the grey matter of the brain. *Journal of Cerebral Blood Flow & Metabolism*, 21(10):1133–1145.

Babu, V., Vazirian, S., Perkins, G., and Lysakowski, A. (2017). Energy output of mitochondria located near synaptic ribbons in inner ear hair cells. *The FASEB Journal*, 31(1_supplement):740.21–740.21.

Barbour, L. R. and P, C. H. (1981). Characterization of the kinetics and mechanism of the mitochondrial ADP-ATP carrier. *Journal of Biological Chemistry*, 256(4):1940–1981.

Beard, D. A. (2005). A biophysical model of the mitochondrial respiratory system and oxidative phosphorylation. *PLoS Computational Biology*, 1(4):e36.

Calvo, S. E., Clauser, K. R., and Mootha, V. K. (2015). Mitocarta2. 0: an updated inventory of mammalian mitochondrial proteins. *Nucleic Acids Research*, 44(D1):D1251–D1257.

Chinopoulos, C., Vajda, S., Csanády, L., Mándi, M., Mathe, K., and Adam-Vizi, V. (2009). A novel kinetic assay of mitochondrial ATP-ADP exchange rate mediated by the ant. *Biophysical journal*, 96(6):2490–2504.

Cleland, W. W. (1963). The kinetics of enzyme-catalyzed reactions with two or more substrates or products: I. nomenclature and rate equations. *Biochimica et Biophysica Acta (BBA)-Specialized Section on Enzymological Subjects*, 67:104–137.

Clewley, R. (2012). Hybrid models and biological model reduction with PyDSTool. *PLoS Comput. Biol.*, 8(8):e1002628.

Clewley, R. H., Sherwood, W. E., LaMar, M. D., and Guckenheimer, J. M. (2007). PyDSTool, a software environment for dynamical systems modeling.

Colombini, M. (1989). Voltage gating in the mitochondrial channel, vdac. *Journal of Membrane Biology*, 111(2):103–111.

Cortassa, S nad Aon, M. A., Marban, E., Winslow, R., and ORourke, B. (2003). An integrated model of cardiac mitochondrial energy metabolism and calcium dynamics. *Biophysical Journal*, 84:2734 – 2755.

Dash, R. K., Qi, F., and Beard, D. A. (2009). A biophysically based mathematical model for the kinetics of mitochondrial calcium uniporter. *Biophysical Journal*, 96(4):1318–1332.

De Pinto, V., Ludwig, O., Krause, J., Benz, R., and Palmieri, F. (1987). Porin pores of mitochondrial outer membranes from high and low eukaryotic cells: biochemical and biophysical characterization. *Biochimica et Biophysica Acta (BBA) - Bioenergetics*, 894(2):109–119.

Devine, M. J. and Kittler, J. T. (2018). Mitochondria at the neuronal presynapse in health and disease. *Nature Reviews Neuroscience*, 19(2):63.

Dieteren, C. E. J., Gielen, S. C. A. M., Nijtmans, L. G. J., Smeitink, J. A. M., Swarts, H. G., Brock, R., Willems, P. H. G. M., and Koopman, W. J. H. (2011). Solute diffusion is hindered in the mitochondrial matrix. *Proceedings of the National Academy of Sciences*, 108(21):8657–8662.

Duchen, M. R. (1999). Contributions of mitochondria to animal physiology: from homeostatic sensor to calcium signalling and cell death. *The Journal of physiology*, 516(1):1–17.

Duyckaerts, C., Sluse-Goffart, C. M., Fux, J. P., Sluse, F. E., and Lièbecq, C. (1980). Kinetic mechanism of the exchanges catalysed by the adenine-nucleotide carrier. *European Journal of Biochemistry*, 106(1):1–6.

Frey, T. G., Perkins, G. A., and Ellisman, M. H. (2006). Electron tomography of membrane-bound cellular organelles. *Annu. Rev. Biophys. Biomol. Struct.*, 35:199–224.

Gerhart-Hines, Z. and Lazar, M. A. (2015). Circadian metabolism in the light of evolution. *Endocrine Reviews*, 36(3):289–304.

Goodsell, D. S., Dutta, S., Zardecki, C., Voigt, M., Berman, H. M., and Burley, S. K. (2015). The rcsb pdb molecule of the month: inspiring a molecular view of biology. *PLoS biology*, 13(5):e1002140.

Gropp, T., Brustovetsky, N., Klingenberg, M., Müller, V., Fendler, K., and Bamberg, E. (1999). Kinetics of electrogenic transport by the ADP/ATP carrier. *Biophysical journal*, 77(2):714–726.

Gunawardena, J. (2014). Models in biology:accurate descriptions of our pathetic thinking. *BMC biology*, 12(1):29.

Gupta, S., Czech, J., Kuczewski, R., Bartol, T. M., Sejnowski, T. J., Lee, R. E., and Faeder, J. R. (2018). Spatial stochastic modeling with mcell and cellblender. *arXiv preprint arXiv:1810.00499*.

Hackenbrock, C. R. (1966). Ultrastructural bases for metabolically linked mechanical activity in mitochondria. I. reversible ultrastructural changes with change in metabolic steady state in isolated liver mitochondria. *The Journal of Cell Biology*, 30(2):269–297.

Hackenbrock, C. R. (1968). Ultrastructural bases for metabolically linked mechanical activity in mitochondria: II. electron transport-linked ultrastructural transformations in mitochondria. *The Journal of cell biology*, 37(2):345.

Heller, E. and Fuchs, E. (2015). Tissue patterning and cellular mechanics. *J Cell Biol*, 211(2):219–231.

Hill, T. L. (1989). *Free energy transduction and biochemical cycle kinetics*. Springer-Verlag New York Inc.

Hoppins, S., Collins, S. R., Cassidy-Stone, A., Hummel, E., DeVay, R. M., Lackner, L. L., Westermann, B., Schuldiner, M., Weissman, J. S., and Nunnari, J. (2011). A mitochondrial-focused genetic interaction map reveals a scaffold-like complex required for inner membrane organization in mitochondria. *J Cell Biol*, 195(2):323–340.

Horvath, S., Zhang, B., Carlson, M., Lu, K., Zhu, S., Felciano, R., Laurance, M., Zhao, W., Qi, S., Chen, Z., et al. (2006). Analysis of oncogenic signaling networks in glioblastoma identifies aspm as a molecular target. *Proceedings of the National Academy of Sciences*, 103(46):17402–17407.

Johnson, D. T., Harris, R. A., Blair, P. V., and Balaban, R. S. (2007). Functional consequences of mitochondrial proteome heterogeneity. *American Journal of Physiology-Cell Physiology*, 292(2):C698–C707.

Keener, J. P. and Sneyd, J. (1998). *Mathematical physiology*, volume 1. Springer.

Kerr, R. A., Bartol, T. M., Kaminsky, B., Dittrich, M., Chang, J.-C. J., Baden, S. B., Sejnowski, T. J., and Stiles, J. R. (2008). Fast monte carlo simulation methods for biological reaction-diffusion systems in solution and on surface. *SIAM Journal on Scientific Computing*, 30(6):3126–3149.

Kirichok, Y., Krapivinsky, G., and Clapham, D. E. (2004). The mitochondrial calcium uniporter is a highly selective ion channel. *Nature*, 427(6972):360.

Kitano, H. (2002). Systems biology: a brief overview. *science*, 295(5560):1662–1664.

Klingenberg, M. (2008). The ADP and ATP transport in mitochondria and its carrier. *Biochimica et Biophysica Acta (BBA)-Biomembranes*, 1778(10):1978–2021.

Knott, A. B., Perkins, G., Schwarzenbacher, R., and Bossy-Wetzel, E. (2008). Mitochondrial fragmentation in neurodegeneration. *Nature Reviews Neuroscience*, 9(7):505–518.

Ko, Y. H., Delannoy, M., Hullihen, J., Chiu, W., and Pedersen, P. L. (2003). Mitochondrial atp synthasome cristae-enriched membranes and a multiwell detergent screening assay yield dispersed single complexes containing the ATP synthase and carriers for Pi and ADP/ATP. *Journal of Biological Chemistry*, 278(14):12305–12309.

Kraemer, R. and Klingenberg, M. (1982). Electrophoretic control of reconstituted adenine nucleotide translocation. *Biochemistry*, 21(5):1082–1089.

Lawrence, A., Bouwer, J. C., Perkins, G., and Ellisman, M. H. (2006). Transform-based backprojection for volume reconstruction of large format electron microscope tilt series. *Journal of Structural Biology*, 154(2):144–167.

Lill, R., Hoffmann, B., Molik, S., Pierik, A. J., Rietzschel, N., Stehling, O., Uzarska, M. A., Webert, H., Wilbrecht, C., and Mühlenhoff, U. (2012). The role of mitochondria in cellular iron–sulfur protein biogenesis and iron metabolism. *Biochimica et Biophysica Acta (BBA)-Molecular Cell Research*, 1823(9):1491–1508.

López-Beltrán, E. A., Maté, M. J., and Cerdán, S. (1996). Dynamics and environment of mitochondrial water as detected by ^{1}HNMR. *Journal of Biological Chemistry*, 271(18):10648–10653.

Lowell, B. B. and Shulman, G. I. (2005). Mitochondrial dysfunction and type 2 diabetes. *Science*, 307(5708):384–387.

MacAskill, A. F. and Kittler, J. T. (2010). Control of mitochondrial transport and localization in neurons. *Trends in cell biology*, 20(2):102–112.

Magnus, G. and Keizer, J. (1997). Minimal model of beta cell mitochondrial Ca^{2+} handling modeling of mitochondrial adenine nucleotide translocase. *American Journal of Physiology-Cell*, 273:C717–C733.

Mannella, C. A. (1998). Conformational changes in the mitochondrial channel protein, VDAC, and their functional implications. *Journal of structural biology*, 121(2):207–218.

Mannella, C. A. (2000). Introduction: our changing views of mitochondria.

Mannella, C. A. (2006). The relevance of mitochondrial membrane topology to mitochondrial function. *Biochimica et Biophysica Acta (BBA)-Molecular Basis of Disease*, 1762(2):140–147.

Mannella, C. A., Lederer, W. J., and Jafri, M. S. (2013). The connection between inner membrane topology and mitochondrial function. *Journal of molecular and cellular cardiology*, 62:51–57.

Metelkin, E., Demin, O., Kovcs, Z., and Chinopoulos, C. (2009). Modeling of ATPADP steady-state exchange rate mediated by the adenine nucleotide translocase in isolated mitochondria. *FEBS Journal*, 276(23):6942–6955.

Metelkin, E., Goryanin, I., and Demin, O. (2006). Mathematical modeling of mitochondrial adenine nucleotide translocase. *Biophysical Journal*, 90(2):423 – 432.

Milo, R., Jorgensen, P., Moran, U., Weber, G., and Springer, M. (2009). Bionumbersthe database of key numbers in molecular and cell biology. *Nucleic acids research*, 38(suppl_1):D750–D753.

Milo, R. and Phillips, R. (2015). *Cell biology by the numbers*. Garland Science.

Nilsson, R., Schultz, I. J., Pierce, E. L., Soltis, K. A., Naranuntarat, A., Ward, D. M., Baughman, J. M., Paradkar, P. N., Kingsley, P. D., Culotta, V. C., et al. (2009). Discovery of genes essential for heme biosynthesis through large-scale gene expression analysis. *Cell metabolism*, 10(2):119–130.

Noskov, S., Hermida, O. T., Rostovtseva, T., and Sergei, B. (2014). Mapping conformational states in VDAC1 channel: Complexity of gating landscape. *Biophysical Journal*, 106(2):234a.

Noskov, S. Y., Rostovtseva, T. K., Chamberlin, A. C., Teijido, O., Jiang, W., and Bezrukov, S. M. (2016). Current state of theoretical and experimental studies of the voltage-dependent anion channel (VDAC). *Biochimica et Biophysica Acta (BBA)-Biomembranes*, 1858(7):1778–1790.

Nury, H., Dahout-Gonzalez, C., Trezeguet, V., Lauquin, G. J. M., Brandolin, G., , and Pebay-Peyroula, E. (2006). Relations between structure and function of the mitochondrial ADP/ATP carrier. *Annu. Rev. Biochem.*, 75:713–741.

Ölveczky, B. P. and Verkman, A. (1998). Monte carlo analysis of obstructed diffusion in three dimensions: Application to molecular diffusion in organelles. *Biophysical Journal*, 74(5):2722 – 2730.

Panda, S. (2019). The arrival of circadian medicine. *Nature Reviews Endocrinology*, 15(2):67.

Panda, S., Antoch, M. P., Miller, B. H., Su, A. I., Schook, A. B., Straume, M., Schultz, P. G., Kay, S. A., Takahashi, J. S., and Hogenesch, J. B. (2002a). Coordinated transcription of key pathways in the mouse by the circadian clock. *Cell*, 109(3):307–320.

Panda, S., Sato, T. K., Castrucci, A. M., Rollag, M. D., DeGrip, W. J., Hogenesch, J. B., Provencio, I., and Kay, S. A. (2002b). Melanopsin (opn4) requirement for normal light-induced circadian phase shifting. *Science*, 298(5601):2213–2216.

Partikian, A., Ölveczky, B., Swaminathan, R., Li, Y., and Verkman, A. (1998). Rapid diffusion of green fluorescent protein in the mitochondrial matrix. *The Journal of cell biology*, 140(4):821–829.

Perkins, G., Jackson, D. R., and Spirou, G. A. (2015). Resolving presynaptic structure by electron tomography. *Synapse*, 69:268–282.

Perkins, G., Renken, C., Martone, M. E., Young, S. J., Ellisman, M., and Frey, T. (1997). Electron tomography of neuronal mitochondria: three-dimensional structure and organization of cristae and membrane contacts. *Journal of structural biology*, 119(3):260–272.

Perkins, G. A. (2014). The use of minisog in the localization of mitochondrial proteins. In *Methods in enzymology*, volume 547, pages 165–179. Elsevier.

Perkins, G. A. and Ellisman, M. H. (2011). Mitochondrial configurations in peripheral nerve suggest differential ATP production. *Journal of structural biology*, 173(1):117–127.

Perkins, G. A., Renken, C. W., Frey, T. G., and Ellisman, M. H. (2001). Membrane architecture of mitochondria in neurons of the central nervous system. *Journal of Neuroscience Research*, 66(5):857–865.

Perkins, G. A., Tjong, J., Brown, J. M., Poquiz, P. H., Scott, R. T., Kolson, D. R., Ellisman, M. H., and Spirou, G. A. (2010). The micro-architecture of mitochondria at active zones: electron tomography reveals novel anchoring scaffolds and cristae structured for high-rate metabolism. *Journal of Neuroscience*, 30(3):1015–1026.

Pfanner, N., van der Laan, M., Amati, P., Capaldi, R., Caudy, A., Chacinska, A., Darshi, M., Deckers, M., Hoppins, S., Icho, T., et al. (2014). Uniform nomenclature for the mitochondrial contact site and cristae organizing system. *The Journal of cell biology*, 204(7):1083–1086.

Phan, S., Boassa, D., Nguyen, P., Wan, X., Lanman, J., Lawrence, A., and Ellisman, M. H. (2016). 3D reconstruction of biological structures: automated procedures for alignment and reconstruction of multiple tilt series in electron tomography. *Advanced Structural and Chemical Imaging*, 2(1):8.

Phillips, R. (2015). Theory in biology: Figure 1 or figure 7? *Trends in Cell Biology*, 25(12):723–729.

Phillips, R., Theriot, J., Kondev, J., and Garcia, H. (2012). *Physical biology of the cell*. Garland Science.

Pietrobon, D. and Caplan, S. R. (1985). Flow-force relationships for a six-state proton pump model: Intrinsic uncoupling, kinetic equivalence of input and output forces, and domain of approximate linearity. *Biochemistry*, 24(21):5764–5776.

Pradhan, R. K., Qi, F., Beard, D. A., and Dash, R. K. (2010). Characterization of membrane potential dependency of mitochondrial Ca$2+$ uptake by an improved biophysical model of mitochondrial Ca$2+$ uniporter. *PLoS One*, 5(10):e13278.

Reed, K. C. and Bygrave, F. L. (1974). The inhibition of mitochondrial calcium transport by lanthanides and ruthenium red. *Biochemical Journal*, 140(2):143–155.

Scalettar, B. A., Abney, J. R., and Hackenbrock, C. R. (1991). Dynamics, structure, and function are coupled in the mitochondrial matrix. *Proceedings of the National Academy of Sciences*, 88(18):8057–8061.

Scarpulla, R. C. (2011). Metabolic control of mitochondrial biogenesis through the pgc-1 family regulatory network. *Biochimica et Biophysica Acta (BBA)-Molecular Cell Research*, 1813(7):1269–1278.

Scheffler, I. E. (2009). *Mitochondria*. Wiley, second edition.

Schwerzmann, K., Cruz-Orive, L. M., Eggman, R., Sänger, A., and Weibel, E. R. (1986). Molecular architecture of the inner membrane of mitochondria from rat liver: a combined biochemical and stereological study. *The Journal of Cell Biology*, 102(1):97–103.

Shu, X., Lev-Ram, V., Deerinck, T. J., Qi, Y., Ramko, E. B., Davidson, M. W., Jin, Y., Ellisman, M. H., and Tsien, R. Y. (2011). A genetically encoded tag for correlated light and electron microscopy of intact cells, tissues, and organisms. *PLoS biology*, 9(4):e1001041.

Song, D. H., Park, J., Maurer, L. L., Lu, W., Philbert, M. A., and Sastry, A. M. (2013). Biophysical significance of the inner mitochondrial membrane structure on the electrochemical potential of mitochondria. *Physical Review E*, 88(6):062723.

Sosinsky, G. E., Crum, J., Jones, Y. Z., Lanman, J., Smarr, B., Terada, M., Martone, M. E., Deerinck, T. J., Johnson, J. E., and Ellisman, M. H. (2008). The combination of chemical fixation procedures with high pressure freezing and freeze substitution preserves highly labile tissue ultrastructure for electron tomography applications. *Journal of Structural Biology*, 161(3):359 – 371. The 4th International Conference on Electron Tomography.

Stiles, J. R. and Bartol, T. M. (2001). *Monte Carlo Methods for Simulating Realistic Synaptic Microphysiology Using MCell*, chapter 4. CRC Press.

Stiles, J. R., Van Helden, D., Bartol, T. M., and Salpeter, M. M. (1996). Miniature endplate current rise times < 100 μs from improved dual recordings can be modeled with passive acetylcholine diffusion from a synaptic vesicle. *Proceedings of the National Academy of Sciences of the United States of America*, 93(12):5747–5752.

Straume, M. (2004). Dna microarray time series analysis: automated statistical assessment of circadian rhythms in gene expression patterning. *Methods in enzymology*, 383:149–166.

Strauss, M., Hofhaus, G., Schröder, R. R., and Kühlbrandt, W. (2008). Dimer ribbons of ATP synthase shape the inner mitochondrial membrane. *The EMBO Journal*, 27(7):1154–1160.

Szabo, I. and Zoratti, M. (2014). Mitochondrial channels: ion fluxes and more. *Physiological reviews*, 94(2):519–608.

Vinogradov, A. and Scarpa, A. (1973). The initial velocities of calcium uptake by rat liver mitochondria. *Journal of Biological Chemistry*, 248(15):5527–5531.

Voet, D. and Voet, J. G. (2011). *Biochemistry*. John Wiley and Sons, Inc., fourth edition.

Vogel, F., Bornhövd, C., Neupert, W., and Reichert, A. S. (2006). Dynamic subcompartmentalization of the mitochondrial inner membrane. *J Cell Biol*, 175(2):237–247.

Vollmers, C., Gill, S., DiTacchio, L., Pulivarthy, S. R., Le, H. D., and Panda, S. (2009). Time of feeding and the intrinsic circadian clock drive rhythms in hepatic gene expression. *Proceedings of the National Academy of Sciences*, 106(50):21453–21458.

Vyssokikh, M. Y., Katz, A., Rueck, A., Wuensch, C., Dörner, A., Zorov, D. B., and Brdiczka, D. (2001). Adenine nucleotide translocator isoforms 1 and 2 are differently distributed in the mitochondrial inner membrane and have distinct affinities to cyclophilin D. *Biochemical Journal*, 358(2):349–358.

Wallace, D. C. (2012). Mitochondria and cancer. *Nature Reviews Cancer*, 12(10):685.

Williams, G. S. B., Boyman, L., Chikando, A. C., Khairallah, R. J., and Lederer, W. J. (2013). Mitochondrial calcium uptake. *Proceedings of the National Academy of Sciences*, 110(26):10479–10486.

Wittig, I. and Schägger, H. (2009). Supramolecular organization of ATP synthase and respiratory chain in mitochondrial membranes. *Biochimica et Biophysica Acta (BBA)-Bioenergetics*, 1787(6):672–680.

Yoshida, M., Muneyuki, E., and Hisabori, T. (2001). Atp synthase-a marvellous rotary engine of the cell. *Nature reviews Molecular cell biology*, 2(9):669.

Zarrinpar, A., Chaix, A., and Panda, S. (2016). Daily eating patterns and their impact on health and disease. *Trends in Endocrinology & Metabolism*, 27(2):69–83.

Zhang, B. and Horvath, S. (2005). A general framework for weighted gene co-expression network analysis. *Statistical applications in genetics and molecular biology*, 4(1).

Zick, M., Rabl, R., and Reichert, A. S. (2009). Cristae formationlinking ultrastructure and function of mitochondria. *Biochimica et Biophysica Acta (BBA)-Molecular Cell Research*, 1793(1):5–19.